Synthesis, Characterisation and Application of Carbonised Metal Organic Frameworks

Naghmeh Saeidi Bidokhti

Department of Chemical Engineering

Submitted to the University College London for the Degree of

Doctor of Philosophy

December 2017

Declaration

I, Naghmeh Saeidi Bidokhti, confirm that the work presented in this thesis is my own. Where information has been derived from other sources, I confirm that this has been indicated in the thesis.

Naghmeh Saeidi Bidokhti

Abstract

The main purpose of this project was to synthesise, characterise and evaluate metal organic frameworks (MOFs) and MOF-derived carbons for different applications. Carbon is widely used in the structure of electrodes of electrochemical energy conversion/storage devices. In order to control the pore size distribution of such carbons, the pyrolysis of MFOs under inert atmosphere was considered. MOFs are highly porous crystalline materials constructed from metal ions linked together by different organic ligands. When MOFs are pyrolysed, the resulting carbon material inherits the pore structure of the precursor MOF. By combining different metal ions and organic linkers, it is possible to create MOFs with different pore sizes. In this research, we aimed to take advantage of this property and derive carbons from MOFs to produce porous carbons with controlled pore size distributions and evaluate their behaviour in electrochemical energy conversion/storage devices to improve the performance of the latter. Three different MOFs were selected in terms of their pore sizes (ZIF-8, MOF-5 and MIL-100(Fe)) and were hydrothermally synthesised and characterised with Brunauer–Emmet–Teller (BET) and powder X-ray diffraction. These MOFs were then carbonised under an argon atmosphere and characterised with BET and energy dispersive spectroscopy analysis. The electrocatalyst was made by loading platinum on the carbonised ZIF-8 and characterised with EDS to measure the amount of platinum loaded and assess the homogeneity of the platinisation process for fuel cell application. The Pt/C_{ZIF-8} was electrochemically characterised by cyclic voltammetry, oxygen reduction reaction and durability tests to evaluate its electrochemical behaviour. For the supercapacitor applications, all MOF-derived carbons were characterised by cyclic voltammetry and the cyclic charge–discharge curve.

The separation ability of the MOFs was also assessed by immersion calorimetry, and when any unexpected behaviour was observed, the assessment was applied to the replica MOF (carbonised MOFs), and their behaviour was observed. After evaluating the results, the best MOF/carbonised MOF for each application was introduced. Four different MOFs, ZIF-8, HKUST, UiO-66 and UiO-67, were synthesised and characterised with BET and X-ray diffraction, and their separation ability was investigated using immersion calorimetry in xylene isomers. Since HKUST and UiO-66 had unexpected adsorption behaviour, the replicas of these MOFs were also produced under argon, and their separation ability was evaluated in m-xylene.

Impact Statement

The main aim of this research was focused on the enhancement of the performance of electrochemical devices (supercapacitors and proton exchange membrane fuel cells) and separation industries. The high demand for energy currently results in a considerable amount of pollutant, which is of great concern. To overcome this problem, electrodes/electrocatalysts with better performance and longer lifecycles have been used. Highly porous materials and their derivatives are used as electrodes/electrocatalysts and adsorbents respectively. The porosity of the electrode materials has been controlled using the carbonisation of MOFs. MOFs are highly crystalline materials that have recently gained much attention owing to their high surface area, permanent porosity and varying applications. By controlling the pore sizes of the electrodes/electrocatalysts used in fuel cells/supercapacitors, it is possible to optimise the efficiency of these industry applications. Different MOF-derived carbons with controlled porosity were synthesised, and the evaluation of their applications in electrochemical industries has shown that it is possible to optimise the performance of supercapacitors by controlling the porosity of the carbon used for the electrode preparation.

Moreover, although xylene is one of the most commonly used solvents in different industries, the removal of this solvent has always been a matter of concern. Various MOFs with different pore sizes and structures were thus synthesised and used for adsorption of xylene isomers using the immersion calorimetry technique in order to identify the best performance adsorbents for the separation of xylene isomers.

Considering the easy and convenient methods of synthesising these materials, they have the potential for industrial scale production. In 2016, Young et al. evaluated the application.

Finally, MOFs are currently produced industrially by the BASF Company and sold by Sigma-Aldrich, which provides the opportunity for researchers and people in the supercapacitor industry or separation industries to use these materials to improve their production performance.

Table of Contents

List of Abbreviations

BDC: Benzenedicarboxylic acid

BET: Brunauer–Emmett–Teller

BPDC: Biphenyldicarboxylicacid

BTC: Benzenetricaboxylate

CCD: Cyclic charge0discharge

CNTs: Carbon nanotubes

DEF: N,N diethylformamide

DFT: Density functional theory

DMF: N,N dimethylformamide

EDLC: Electric double-layer capacitance

HER: Hydrogen evolution reaction

MOFs: Metal organic frameworks

NGPCs: Nitrogen doped graphitic porous carbons

NMP: N-methyl-2-pyrrolidone

NPCs: Nanoporous carbons

OER: Oxygen evolution reaction

ORR: Oxygen reduction reaction

PANI: Polyaniline

PEMFC: Proton exchange membrane fuel cell

PGM: Platinum group metals

PTFE: Polytetrafluoroethylene

PVDF: Polyvinylidene fluoride

PXRD: Powder X-ray diffraction

RDE: Rotating disk electrode

RHE: Reversible hydrogen electrode

RRDE: Rotating ring-disk electrode

SEM: Scanning electron microscopy

TEM: Transmission electron microscopy

UHP: Ultra high pressure

ZIF: Zeolitic imiodazolate framework

List of Nomenclature

p_0: Equilibrium pressure

p: Saturation pressure

C: BET constant

$\mathrm{n_m}$: Number of the gas molecules adsorbed

E_1: Heat of adsorption for the first layer

E_L: Liquefaction energy

L: Avogadro constant ($6.022140857 \times 10^{23}$)

σ: Average area each molecule of adsorbate occupies

d: Distance between atomic layers of the sample

λ: Wavelength of the incident X-ray beam

θ: Scattering angle

I_S: Specific activity

I_K (A): Kinetic current

I: Current in amperes

W: Mass of electrode material

V: Volts

A: Ampere

C: Coulomb

Δh_{vap}: Molar vaporisation energy

P_0: Saturation pressure of adsorbate

V: Dead volume of the bulb

R: Ideal gas constant

P: Vapour pressure

A, B and C: Antoine constants

T: Temperature (°C)

ρ: Density (g/cm^3)

Table of Figures

List of Tables

Acknowledgments

Firstly, I would like to thank my advisor, Dr Ozgur Yazaydin, for his support, motivation and patience during my PhD.

My sincere thanks go to Professor Haroun Mahgerefteh and Dr Joaquin Silvestre Albero for their insightful comments.

I would like also to thank Professor Dan Bret and his team at the Electrochemical Innovation Lab for their help and allowing me to use their facilities. Special thanks go to Dr Tobias Neville, Dr Julia Weaving, Dr Noramalina Mansor and Miss Dina Ibrahim Abouelamaiem for their help and guidance throughout my research.

I would like to thank my friends, especially Dr Anna Vartapetiance, who was exceptionally supportive during this journey.

Lastly, I would like to thank my family, my parents and my sister, for supporting me spiritually throughout my studies.

Chapter 1

1 Introduction

With an ever-increasing population, the demand for energy is also increasing. Owing to the limited source of fossil fuels and their considerable ability to pollute, using sustainable and eco-friendly sources of energy is of the highest concern. Most of the energy used for transportation and heating in life is currently provided by fossil fuels, which are the main producers of carbon emissions. It is estimated that by 2030, the required energy will be 50% more than the current production (Resch et al., 2008). Such increasing energy production will result in further carbon emissions. One way to overcome this problem is to use renewable energy systems such as Li-ion batteries, fuel cells and supercapacitors.

So far, batteries have provided the best performance in terms of energy storage among portable energy storage strategies (Goriparti et al., 2014). Chemical energy is converted directly into electrical energy in batteries through redox reactions in anodes and cathodes (Martin Winter, 2004). The oxidation reaction takes place in the anode and the reduction reaction takes place in the cathode, and the entire reaction is called a redox reaction (Zhang and Zhao, 2009). A wide range of materials have been used as anode materials in Li-ion batteries, such as graphitised carbon, metal oxides and oxysalts. However, graphitised carbon has a relatively low charge storage capability that consequently limits its application, and most metal oxides experience a severe deterioration in capacity during cycling as a result of large volume changes (Goriparti et al., 2014, Reddy et al., 2013). One of the challenges related to anode materials used in Li-ion batteries is to have high stability and a large surface area. These requirements can be met by using metal organic frameworks (MOFs) as alternatives to the current anode material used in Li-ion batteries (Goriparti et al., 2014). MOFs are crystalline porous materials consisting of metal clusters connected by organic linkers. They usually have high surface areas and large pore volumes, which enable them to have more available sites for electron transport.

Another source of clean and sustainable energy conversion is a proton exchange membrane fuel cell (PEMFC). The PEMFC converts chemical energy directly into electrical energy via the oxidation of H_2 to H_2O (Steele and Heinzel, 2001). The most common material used as electrocatalyst in PEMFCs are carbon materials loaded by platinum (Pt) nanoparticles. High porosity and a large surface area are two important properties that support materials are required to have in order to enhance the electron transfer and improve the dispersion of the Pt on the support (Candelaria et al., 2012). MOFs have recently been used as electrodes/electrocatalysts in electrochemical energy storage/conversion devices (Ferey et al., 2007) (Zhao et al., 2012). For instance, they have been considered as electrocatalysts in the fuel cells to reduce the high cost of platinum group metals (PGM) as well as increase the rate of mass transfer. However, the poor conductivity of the MOFs (Ferey et al., 2007) (Li et al., 2006) has not provided a good result for electrochemical devices, hence the carbonisation of MOFs was suggested to overcome this problem (Morozan and Jaouen, 2012).

Supercapacitors (also known as electrochemical capacitors) are another source of clean energy that has attracted much attention owing to their long lifecycle, high power supply, simple principals and high charge generation. The main electrode materials used thus far for supercapacitors are activated carbons, which have high surface areas and good electrical properties. Activated carbons usually are produced from carbonaceous materials such as nutshells, coal, wood, etc. They often are treated with different methods and with different agents (such as physical activation with heat treatment at temperatures around 700 to 1200 °C under an oxidising atmosphere such as steam or CO_2; or chemical activation, which includes heat treatment at lower temperatures, usually around 400 to 700 °C, followed by an activating agent such as phosphoric acid, potassium hydroxide, sodium hydroxide and zinc chloride). The different treatment methods result in carbons with different properties.

Activating carbons enables them to have a porous structure varying between micropores (0 to 2 nm), mesopores (2 to 5 nm) and macropores (larger than 5nm). Previous studies have shown that not only the specific surace area is important in the capacitance of the electric double-layer capacitance (EDLC), but also other properties, such as pore size and pore shape, can also affect the performance of the EDLCs (Zhang and Zhao, 2009).

MOF-derived porous carbons are a new class of porous materials, which usually inherit the highly porous nature of the precursor MOF structure. Hence, they are highly desirable for application in electrochemical devices. Using electrodes/electrocatalysts with different pore sizes can generate different performance behaviours in PEMFC and Li-ion batteries. One of the methods used to increase the performance of these devices is to control the microporosity of the support material (carbon) of the electrodes/electrocatalysts. Carbon with a micropore structures provides a larger surface area, which means there is higher capacity for storing electricity. Liu et al. (2010a) have investigated the behaviour of electrochemical properties of supercapacitors using electrodes with different pore size distributions (ranging from 2.9 to 3.9 nm) and surface areas (1141 to 3040 m^2/g). They stated that microporous systems are most useful in improving the energy density, and mesoporous systems are beneficial for improving the power density (Liu et al., 2010a).

Xylene is one of the most commonly used solvents in industries, such as in tissue processing, cover slipping and staining. The chemical formula for xylene is $(CH_3)_2C_6H_4$. It has three isomers; ortho-, meta- and para-xylene (O-, M- and P-xylene). The use of xylene is hazardous, thus the removal of this solvent is of great concern. One of the promising functionality of MOFs is their high adsorption ability. Immersion calorimetry is a useful technique for measuring the adsorption ability of the materials by calorimetry.

Immersion calorimetry is a technique for measuring the heat released when a solid is immersed in a liquid. The measurements can begin when the adsorbate and adsorbant are in contact. When the surface of the solid is in full contact with the liquid, the highest value of immersion enthalpy can be measured. Samples need to be degassed before the measurements are taken, hence the measure enthalpy mainly corresponds to the accessible surface of the solid and the physical-chemical interaction between the solid surface and liquid molecules of the liquid immersion solvent. When the sample has a polar or heterogeneous surface, the enthalpy corresponds to the accessibility of the surface of the solid sample, or the specific interaction between the adsorbate and adsorbent surface.

Measuring the heat exchanged between the reactants and the products for different materials gives different measurements of heat of immersion in various liquids. These differences are owing to both the available surface area of the materials and the specific interaction between the solid surface and the liquid.

This research is composed of eight chapters, starting with an introduction, followed by a background history of the application of MOFs and MOF-derived carbons. The experimental methodology is then described, and followed a discussion of the results, a conclusion, and recommended future works.

Chapter 2

2 Literature Review

2.1 Metal Organic Frameworks

Also known as porous coordination polymers (Horiuchi et al., 2016), MOFs are a class of (organic–inorganic) crystalline microporous materials. These materials have an organic–inorganic structure consisting of metal clusters (inorganic) joined together by organic bridging linkers. It is possible to have a versatile structure just by changing the metal cluster or organic linker (Spanopoulos et al., 2015). This feature makes MFOs unique in terms of their structural properties, and offers the potential for use in different functionalities. The relatively facile synthesis method of MOFs is one the reasons that they are a good choice for a variety of applications. Their chemical functionality, tailored pore structure/size and thermal stability make them suitable for different applications such as drug delivery, gas storage (Li et al., 2014a), separation (Car et al., 2006), catalysis (Llabrés i Xamena et al., 2007) and proton conduction (Park et al., 2006).

Figure 1 illustrates a schematic view of the structure of three different MOFs: HKUST-1 (formed from $Cu(NO_3)_2$: 2.5 H_2O as the metal cluster and 1,3,5-benzenetricarboxylic acid as the linker), ZIF-8 (made from zinc nitrate coordinated by 2-methylimidazole in the same way, as Si and Al atoms are covalently joined by bridging oxygen in zeolites), and UiO-66 (consisting of $Zr_6O_4(OH)_4$ linked by 1,4-benzodicarboxylic acid linkers).

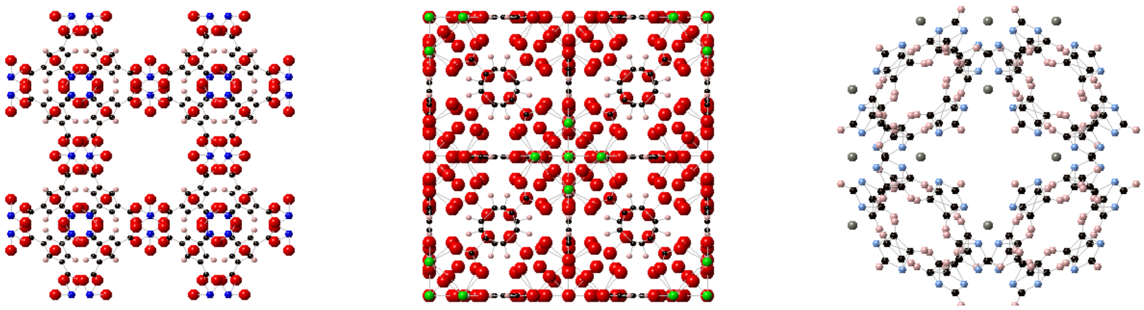

HKUST-1 UiO-66 ZIF-8

Figure 1: The schematic structure of some MOFs drawn by crystal maker software licenced by UCL

Yaghi et al. (1995) were the first researchers who defined the new family of porous materials denoted by MFO-5 (Morozan and Jaouen, 2012), following its introduction by Tomic et al. in 1965, and then primary investigations by Hoskins and Robson (Li et al., 1999).

There is a wide range of methods available to synthesise MOFs, including the solvothermal (hydrothermal), electrochemical, microwave-assisted, mechanochemical and sonochemical synthesis methods. Each of these methods are described below:

- Hydrothermal synthesis: the reactions usually take place in a hydrothermal or solvothermal medium at a temperature above the boiling point of the solvent (Rabenau, 1985). Most of the MOFs are synthesised using this method. For instance, Ferey et al. (2007) synthesised MIL-101 hydrothermally using chromium salt and benzendicarboxylic acid under autogenous pressure in an autoclave system.
- Electrochemical synthesis: in 2006, Mueller et al. (2006) for the first time synthesised Cu-BTC electrochemically. Here, bulk copper plates were used as anodes and the carboxylate linker (1,3,5-benzenetricarboxylic acid) was

dissolved in methanol and used as a cathode in an electrochemical cell (Mueller et al., 2006).

- Microwave-assisted synthesis: this method is based on the interaction of electromagnetic waves and mobile electric charges. These can be polar solvent molecules or ions in a solution or electron/ions in a solid. Jhung et al. (2005) used a microwave oven to synthesise MIL-100 with a similar procedure to the solvothermal method (Jhung, 2005).
- Mechanochemical synthesis: in this method, the intramolecular bonds of the materials are broken down by mechanical forces followed by a chemical transformation (Stock and Biswas, 2012). Yuan et al. (2010) synthesised H-KUST-1 by grinding $Cu(OAC)_2.H_2O$ and H_3BTC in a ball mill without adding any solvents (Yuan et al., 2010).
- Sonochemical synthesis: this method is related to the chemical reactions that take place with the help of applying ultrasound. Jung et al. (2010) synthesised MOF-117 (Zn4O(BTB)2) by using a sonication bar at 60% power for 40 min, and after several washings, the MOF was activated under vacuum for 24 h (Jung et al., 2010).

MOFs that are synthesised using solvothermal methods have shown higher thermal stability, hence in this study we used the solvothermal method rather than the other aforementioned methods.

The structure of the MOFs is usually determined by the coordination of the metal ions and donor atoms of the linker (also called secondary building units). The strong bond between the metal ions and the linker atoms results in MOFs with a robust structure with micropores and pore apertures within the framework (usually less than 20 Å).

2.1.1 Metal organic frameworks as electrocatalysts for fuel cells

Fuel cells, as sources of clean energy, still face some significant challenges such as increasing their efficiency and power density (Li and Xu, 2013)**.** One of the challenges in the oxygen reduction reaction (ORR) catalysis (Li and Xu, 2013) for fuel cells concerns the number of transferred electrons (n). Usually, having four electrons transferred is the ideal number, as H_2O can then be formed as the product. Ma et al. demonstrated the first application of MOF as a precursor for ORR catalysts in 2011. They investigated the mechanism of electron transfer by using the rotating ring-disk electrode (RRDE) technique (number of transferred electrons = n). The n value of the cobalt imidazole framework activated at 75 ^{o}C was in the range of 3.2 to 3.5. The range was improved to 3.3–3.6 by sonicating the cobalt imidazole in sulphuric acid before preparing the catalyst ink. The results suggest a dominative four electron transfer process with a certain peroxide formation (Ma et al., 2011).

Presently, the most common catalyst materials are PGMs. The Cu-based MOF was synthesised by Li et al. as a non-PGM to be used for an electrode catalyst (Cu-2,2$^{/}$-dipyridinbenzene-1,3,5-tricarboxylate). Two good peaks were obtained at ca.-0.15 V in a phosphate buffer (pH = 6). Li et al (2013) claimed that the positive shift of the potential for an oxygen reduction reaction (ORR) at the modified MOF compared with that of the bare graphene electrode showed the electro-catalytic activity of the Cu-bipy-BTC towards ORR through a four-electron reduction pathway. They believe that the presence of the iron porphyrin in the assembly of the MOF structure has a crucial role in the ORR and oxygen transport. Hence, they synthesised graphene metal porphyrin by the use of pyridine functionalised graphene (G-dye) as a building block with iron porphyrin. It is possible to increase the porosity of MOFs, and hence the performance of the electrochemical charge transfer rate of the iron porphyrin, by adding G-dye (Li and Xu, 2013).

2.1.2 Metal organic frameworks as precursors for non-precious metal electrocatalysts

Previous studies have examined efficient, economical and eco-friendly catalysts for ORR to replace the Pt-based catalysts. Transition metal nitrogen carbon materials (M-N-C), especially Fe-N-C or Co-N-C, have shown excellent electro-catalytic activity, and are thus the focus of much research. Some MOF-derived materials, such as carbon hydrides containing N-doped metal species with homogenous active sites and nanoporous structures, are gaining increased attention. Li et al. (2013) have shown the application of ZIF-67 as the precursor for making Co-N_x-C hybrid, and its application as ORR catalyst in alkaline and acidic electrolytes. They improved the ORR activity and stability by enhancing the leaching process and the temperature of the pyrolysis. It is claimed that, in order to have a high-performaning ORR catalyst, well-dispersed Co-N_x active sites in the nanoporous conductive system are required (Wang et al., 2014). Xia et al. have also mentioned that the particle size of the ZIF-67 precursor has an important role on the catalytic activity (Xia et al., 2014).

A comparison between the ORR activity of the ZIF-67-derived catalyst with different particle size precursors has shown that ORR activity and stability increase with the decrease of the particle size of the crystal (from several micrometers to 300nm). The highest ORR activity has been observed for the ZIF-67 precursor with the smallest particle size. This phenomenon can be explained by the smallest particles being able to provide more active sites and easier access to the catalytic centres, resulting in faster electron transfer.

Some functionalised Fe-based MOFs can also be used as precursors for producing non-precious metal catalysts for fuel cell application, as well as Co-based MOFs. Zhao et al. have reported the use of MIL-88B-NH_3 (Fe-based MOF) as a pyrolytic precursor with a controllable shape and size to improve the non-precious metal catalyst (Zhao et al., 2014a).

Pyrolysis of MIL-88B-NH_3 at 900°C can result in the production of Fe and N co-doped nanocarbons (Fe/FeN/C). The ORR catalyst Fe/FeN/C has shown a higher positive onset potential of 1.03V (vs. Reversible Hydrogen Electrode (RHE)) than Pt/C (1.01 V). Also, the diffusion-limited current density of the Fe/FeN/C catalyst is remarkably higher than that of Pt/C (1.2 times), showing the highest ORR activity among the non-precious metal catalysts previously reported.

The performance of the ORR has shown that nanocarbons characterised by porous structures with Fe/FeN active sites can be helpful for both mass transfer and catalytic conversions during the ORR process. Afsahi et al. (2013) have also used Fe-based MOFs as the only precursor to prepare a cathode electrocatalyst. After pyrolysis, acid leaching and heat treatment were applied under NH_3 at various temperatures, forming iron-nitrogen containing carbon active sites (Afsahi et al., 2013).

In order to gain more efficient ORR catalysts, the speed of the mass transfer needs to be increased, resulting in the expansion of the effective space for diffusion of O_2, H_2 and electrolytes into the catalysts (Xia et al., 2014) (Proietti et al., 2011). The MOF precursors have a porous structure, which makes them a good option for making porous catalysts with high surface areas. However, after carbonisation, the porous structure of the catalysts usually collapses and produces a non-interconnected, disordered pore structure, which is not desirable for mass transfer. Hence, the rational design and fabrication of MOF-derived hybrids as efficient catalysts characterised by highly porous structure with proper three-dimensional interconnected pores for better diffusion of O_2 and H_2 to the catalyst are important.

The successful synthesis of N-doped Fe/Fe_3C@graphitic layer/carbon nanotube hybrid having the MIL-100(Fe) as the precursor was first reported by Li et al. in 2015 (Li et al., 2015).

The large contents of active sites (Fe/N/C species), electron-conductive graphitic layers/carbon nanotubes, and unique designs resulted hybrids showing great activities for oxygen reduction reaction and oxygen evolution reaction.

Xia and co-workers have also reported a new method to prepare new Co@Co_3O_4@C core is situ capsulated into a highly ordered porous carbon matrix using Co-MOFs. (Xia et al., 2015). Converting the Co (the metal cores) to Co@Co_3O_4 particles and transforming organic ligands to porous graphitic carbon, resulted to both improving the electron transfer between Co@Co_3O_4 nanoparticles and porous carbon matrix, and making the removal of the active particles from the matrix support more difficult. Moreover, the three-dimensional interconnected pore structures of the carbon matrix provide improved pathway for the electrolyte and the oxygen compared to the catalyst prepared from pure MOFs crystals. Wei et al (2015), have also reported design of a new hybrid having graphene oxide-supported Co-MOFs particles (Wei et al., 2015)

‘’In addition, Co-MOFs were converted to functional carbon materials with a highly specific surface area, nanoporous structure and nitrogen-doping carbon framework. As a result, this kind of N/Co-doped porous carbon@GO composite with the remarkable features of the porous carbon structure, N/Co doping effect and the introduction of graphene support led to triple electrocatalytic activities for ORR, hydrogen evolution reaction (HER), and OER. Additionally, the good interaction between the N/Co-doped carbon and graphene support make a catalyst composite with superior durability and excellent methanol tolerance’’ (Zhao et al., 2016).

2.1.3 Metal organic frameworks for lithium-ion batteries

Ferey et al. (2007) used MOFs as rechargeable intercalation electrodes by applying MIL-53(Fe) with higher oxidation state metals. They used an MOF mixed with 15 wt.% carbon as the positive electrode and Li-foil as the negative electrode (Ferey et al., 2007).

Recently, Shin et al. (2015) tested the applicability of two Fe-based MOFs: MIL-53(Fe) and MIL-68(Fe). In the Li-ion battery systems, they found that both MIL-53 and MIL-68 have good electrochemical reversibility, with MIL-53 showing better reversibility compared to MIL-68. Before that, they tested the applicability of MOF-177, but the poor performance of MOF-177 prevented them from further investigation. They also evaluated the performance of MIL-101(Fe), but the redox chemistry (Fe^{2+}/Fe^{3+}) was found not to be completely reversible, similar to the MOF-177 (Shin et al., 2015).

2.1.4 Metal organic frameworks as electrodes for supercapacitors

Supercapacitors, are one of the promising energy storage devices, having high-power energy and life cycle. There are two different kinds of supercapacitors; Electrical Double Layer Capacitance (EDLC) and Pseudocapacitive. EDLC, usually uses carbon materials with high surface area and porosity. Which have low energy densities and the charges physically stored. Pseudocapacitive on the other hand, have higher energy density use transition metal oxide and sulphides as active materials.

Here, MOFs and MOF-derived nanomaterials offer great potential in the application of supercapacitors because of their high surface areas, and controllable pores and nanostructures. MOFs can also be good templates for the preparation of metal oxides and porous carbons.

Diaz et al (2012) reported the first use of Co_8-MOF-5 ($Zn_3.68Co$ $0.32O$ $(BDC)_3(DEF)_{0.75}$) as an electrode for EDLCs (Díaz et al., 2012). later, Lee et al (2012), developed another Co-MOF film with good pseudocapacitive behavior having a specific capacitance up to 206.76 F g^{-1} (Lee et al., 2012). Lee et al (2012), has presented more research by using Three organic ligands with different molecular lengths to modify the pore size of Co-based MOFs, in which the MOF with the longer organic linker ($[Co(bpdc)(H_2O)_2]H_2O$, bpdc¼4,4- biphenyldicarboxylic acid) had larger pores, larger surface area, and the highest capacitive properties. The improvement of the electrochemical performance can be due to the continuously interconnected leaflet-like microstructure with fewer structural interfaces (Lee et al., 2013).

In another research, Yang et al (2014) applied a layered structure Ni-based MOF as an electrode material for supercapacitors for the first time and obtained a large specific capacitance, high rate capability of 1127 and 668 F g^{-1} at rates of 0.5 and 10 A g^{-1}, and cycling stability (Yang et al., 2014). More recently, another Zr-based MOF (UiO-66) has been synthesised at different reaction temperatures, resulting in different particle sizes and degrees of crystallisation (Tan et al., 2015). The sample obtained at a low temperature (50 °C) had the smallest particle size and highest specific capacitance of 1144 F g^{-1} at a scan rate of 5 mV s^{-1}. Yaghi's group designed a series of 23 different MOFs with different structure types such as MOF-5, nNi-MOF-74, nHKUST-1, nMOF-177, nUiO-66 and nMOF-867. Among these, the zirconium MOF (nMOF-867) exhibited stack and areal capacitances of 0.64 and 5.09 mF cm^{-2} times that of commercial activated carbon (Choi et al., 2014).

‘’Due to the low conductivity of MOFs, an effective strategy was developed to interweave MOF crystals with conductive polyaniline (PANI) chains (Wang et al., 2015). Interestingly, they further developed flexible solid-state supercapacitors using PANI-ZIF-67-CC as electrode, with a gel electrolyte serving as a separator. They also used these devices to power small electronic devices, such as a light-emitting-diode. These MOF-based solid-state supercapacitors show great potential for flexible and wearable electronics’’ (Wang et al., 2015).

‘’As seen in the above discussion, MOFs can be used as electrode materials for supercapacitors. With the rational design of metal ions, organic linkers and reaction conditions, MOFs with controllable particle and pore size can achieve satisfactory electrochemical properties. However, studies of MOFs directly in supercapacitors are still at an initial stage and more exploration is needed’’ (Zhao et al., 2016)

2.2 Metal Organic Framework-Derived Porous Carbons

The organic part of MOFs predominantly consists of carbon-based materials, which enables them to be an ideal template for the carbonisation process. The other main part of MOFs is the metallic species. Hence, in order to obtain high surface area carbons, it is important to remove all the metallic parts in the carbonisation process. The first study of the direct carbonisation of porous coordination polymers with the extremely large surface area of 5000 m^2 g^{-1} and the pore volume of 4.3 cm^3 g^{-1} was reported by Yamuachi et al. in 2012 (Hu et al., 2012). They also reported that the carbonisation temperature plays an important role in the large surface area and pore volume. There are different methods of obtaining carbons from an MOFs precursor: 1) direct carbonisation of MOFs, which is pyrolisation of MOFs at a temperature higher than the boiling point of the metallic parts of the MOFs; 2) direct carbonisation followed by chemical washing in which, after pyrolisation, the pyrolised MOF is treated with an inorganic solvent, such as, KOH, HCL, furfuryl alcohol, glucose, phenolic resin or ethylenediamine to remove all the metallic species in the MOF structure; and 3) introducing a secondary source of carbon into the pores of the MOF precursor (Yuan et al., 2009) (Radhakrishnan et al., 2011) Hu, 2010). These carbon sources can be; furfuryl alcohol (Jiang et al., 2011), fufuryl or some other carbon-based organics such as glycerol, carbon tetrachloride, ethylenediamine and phenolic resin (Zhao et al., 2016).

Nanoporous carbons (NPCs) are gaining more attention nowadays due to their unique properties such as high specific surface area, tuneable pore size distribution, good chemical resistance, and so forth (Torad et al., 2014). There have been various methods to synthesise porous carbons using versatile templates such as olive seeds, almond shell, date seeds, MOFs, etc.

MOFs can be used as templates for making NPC or other porous materials, and also as electrodes in electrochemical energy conversion devices (Amali et al., 2014b). The functionality of MOFs as a template NPC was first studied by Liu et al. (Bo Liu, 2008). In their experiments, furfuryl alcohol was introduced into the pores of MOF-5 as a carbon precursor and then carbonised at 1000 ^{o}C for 8 h under argon flow. The resulting porous carbon was called NPC, with the Brunauer–Emmett–Teller (BET) surface area and pore volume of 2872 $m^2 g^{-1}$ and 2.06 $cm^3 g^{-1}$ respectively (Liu et al., 2010a).

Different pore structures can be obtained by choosing a specific template for carbonisation; they are usually treated later by KOH to wash out the metal source and gain tuned pore structures and textures.

Zhang et al. (2014) used ZIF-7 (zeolitic imidazolate framework-7) to derive porous carbon. Glucose was used as a carbon source and calcined at 950 °C for 5 h under argon atmosphere. The obtained BET surface area and micropore volume were 783 $m^2 g^{-1}$ and 0.37 $cm^3 g^{-1}$, respectively (Zhang et al., 2014b).

Amali et al. (2014) synthesised ZIF-8 by applying sonication to yield pores with a wider range of porosity (micro- and mesopores) and carbonised ZIF-8 at 800 ^oC (Figure 2). The obtained carbon was called AS-ZC-800 (activated and sonicated-ZIF-8-derived carbon at 800 ^oC), with a BET specific surface area of 2972 $m^2 g^{-1}$ and a pore volume of 2.56 $cm^3 g^{-1}$ (Amali et al., 2014b).

Torad et al. (2014) heated ZIF-67 under argon atmosphere at 600 ^oC and 800 ^oC for 5 h to obtain Co/NPC-600 and Co/NPC-800. The BET surface area and total pore volume of Co/NPC-800 were 345 $m^2 g^{-1}$ and 0.25 $cm^3 g^{-1}$, and for Co/NPC-600 they were 352 $m^2 g^{-1}$ and 0.24 $cm^3 g^{-1}$, respectively (Torad et al., 2014).

Table 1 shows the specific capacitance at different sweep rates for supercapacitors based on various MOF-derived carbons with 1.0 M H_2SO_4 solution as the electrolyte.

Table 1: Specific capacitance at different sweep rates for supercapacitors based on various AS-ZC-(Amali et al., 2014b)

Sweep rate (mVS^{-1})	Specific capacitance(F/g)			
	ZC-800	S-ZC-800	A-ZC-800	AS-ZC-800
10	104	158	170	211
20	96	148	165	210
50	63	136	155	208
100	-	116	141	206

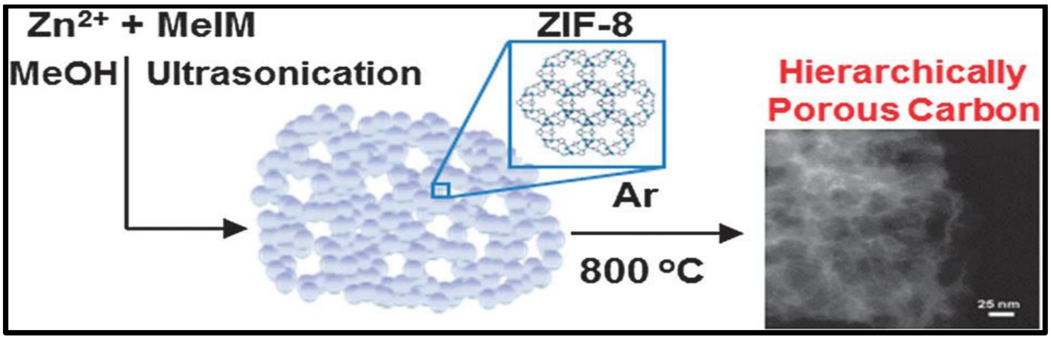

Figure 2: Preparation of hierarchically porous carbons (Amali et al., 2014b)

Shi et al. (2014) also used ZIF-8 to derive porous carbon. They carbonised ZIF-8 by direct carbonisation at 950 ^{o}C in nitrogen atmosphere. The calculated BET surface area and total pore volume for the obtained porous carbon were 1913 m^{2} g^{-1} and 0.84 cm^{3} g^{-1}, respectively. The XRD pattern, nitrogen-sorption isotherm and the corresponding NL-DFT pore size distribution of the ZIF-8-derived carbon are illustrated in Figure 3 (Shi et al., 2014).

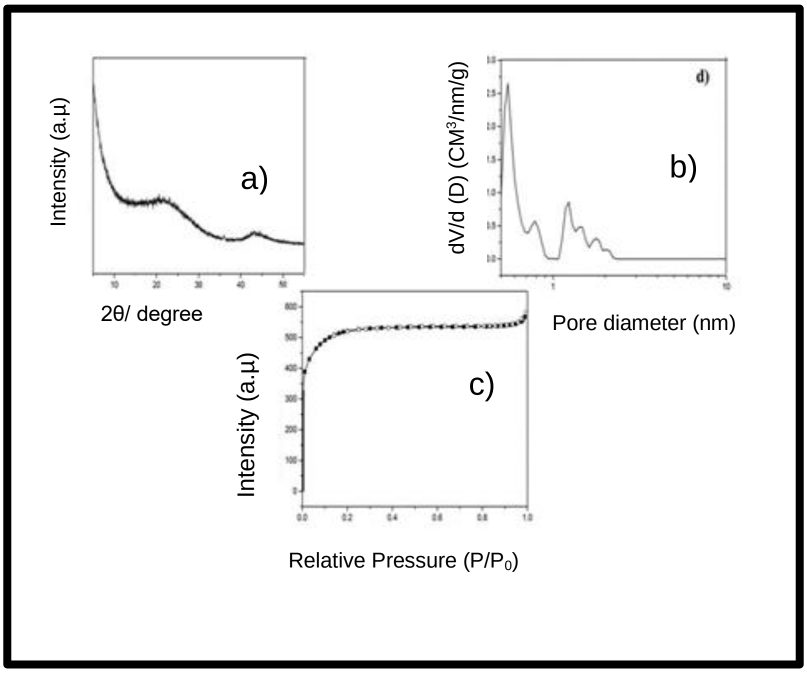

Figure 3: XRD pattern (a), the corresponding NL-DFT pore size distribution (b), and nitrogen-sorption isotherm (c) of ZIF-8 derived carbon (Shi et al., 2014)

Hu et al. (2010) made use of different approaches to obtain porous carbon using MOFs, specifically MOF-5, as a template. In the first approach, they used direct carbonisation of MOF-5 at 873 K (599.85 °C) for 6 h and then increased the temperature to 1173 K (899.85 °C) for another 6 h, and denoted the obtained carbon as MC. In the second approach, they used phenolic resin as an extra carbon precursor, heated the mixture of MOF-5 and phenolic solution at 473 K (199.85 °C) for 2 h, at 873 °C for 4 h, and at 1173 °C for 2 h. They denoted the obtained carbon as PMC. In the third approach, they used carbon tetrachloride and ethylenediamine as the additional carbon sources as well as MOF-5 as both template and precursor. First, they stirred the mixture of MOF-5 in a solution of carbon tetrachloride and ethylenediamine at 363 K (89.850 °C) overnight, and then they heated it at 373 K for 6 h, at 873 K for 6 h, and at 1173 K for another 6 h. They denoted the obtained carbon MAC. All the samples were activated with KOH at 973 K for 3 h under argon flow, denoted MC-A, MPC-A and MAC-a, respectively. A summary of the BET surface area and pore volume of the these samples is illustrated in Table 2, and the nitrogen-sorption isotherm and NL-DFT pore size distribution is illustrated in Figure 4 (Hu et al., 2010).

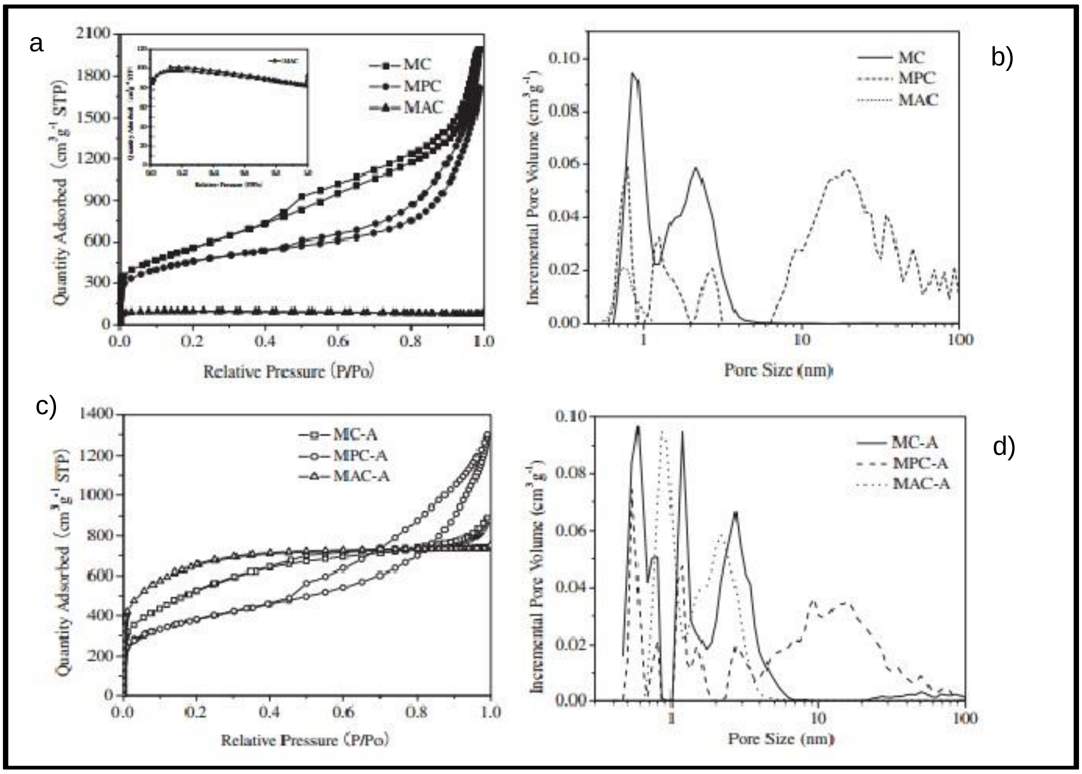

Figure 4: Nitrogen adsorption-desorption isotherms (a, c) and DFT pore size distributions (b, d) of the porous carbons (Hu et al., 2010)

Table 2: Texture parameters of samples of MC, MPC, MAC, MC-A, MPC-A and MAC-A (Hu et al., 2010)

Samples	[a] S_{BET} (m^2/g)	[b] V_t (Cm^3/g)	[c] V_{micro} (Cm^3/g)
MC	1812	2.87	0.92
MPC	1543	2.49	0.89
MAC	384	0.13	0.15
MC-A	1673	1.33	0.68
MPC-A	1271	1.92	0.59
MAC-A	2222	1.14	1.01

a: the specific surface area (S_{BET}) was calculated by the Brunauer-Emmet-Teller method

b: V_t represented the total pore volume

c: V_{micro} represented the volume of micropore

According to Hu et al. (2010), the electrochemical performance of the resultant carbon materials was investigated both in aqueous and organic electrolytes. Carbons with developed mesoporous networks showed high-rate performances, with high capacitance retention ratios. The largest capacitances of 271 and 156 F g^{-1}, as well as the highest energy densities on a gravimetric basis of 9.4 and 31.2 Wh kg^{-1}, were obtained over MAC-A in aqueous and organic electrolytes. When the energy and power densities were calculated on a volumetric basis, the highest volumetric power density in an aqueous electrolyte was 2.4 kW L^{-1} for MAC-A at a discharging time of 10 s, and the highest volumetric power density in organic electrolyte was 5.0 kW L^{-1} for MPC at a discharging time of 10 s (Hu et al., 2010).

A brief summary of the research studies on carbonisation is given in Table 3.

Table 3: Summary of carbonisation studies

Researcher/date	Method	MOF precursor	Final carbonisation temperature/Time (h)	BET surface area (m^2/g) and/ pore volume (cm^3/g)
Xu et al. (2015)	Acid wash with HCl	ZIF-8	800	1302 *[1]
Liu et al. (2010)	Chemical activation-washed with furfuryl alcohol	MOF-5	1000/8	2872/2.06
Zhang et al. (2014)	Chemical activation-washed with glucose	ZIF-7	950/5	783/0.37
Amali et al. (2014)	Direct carbonization	ZIF-8	800	2972/2.56
Torad et al. (2014)	Direct carbonization	ZIF-67	800/5	352/0.24
Shi et al. (2014)	Direct carbonization	ZIF-8	950	1913/0.84
Hu et al. (2010)	Direct carbonization	MOF-5	599.85/6	1812/2.87
	Chemical activation washed with phenolic resin		1173/2	1543/2.49
	Chemical activation washed with carbon tetrachloride and ethylenediamine		1173/2	384/0.13
Hao et al. (2014)	Chemical activation-washed with KOH	ZIF-11	1000/4	-

---

[1] No pore volume has been reported.

Kai Xi et al. (2013) investigated the carbonisation of four different MOFs (room temperature synthesised MOF (RT-MOF-5), solvothermally synthesised MOF-5 (solvo-MOF-5), ZIF-8, and [Zn_3(fumarate)$_3$(DMF)$_2$] (Zn fumarate)) all based on zinc metal, and used them as a conducting host for encapsulating sulphur in a Li-S battery. Figure 5 illustrates the carbonisation process of MOFs (Xi et al., 2013).

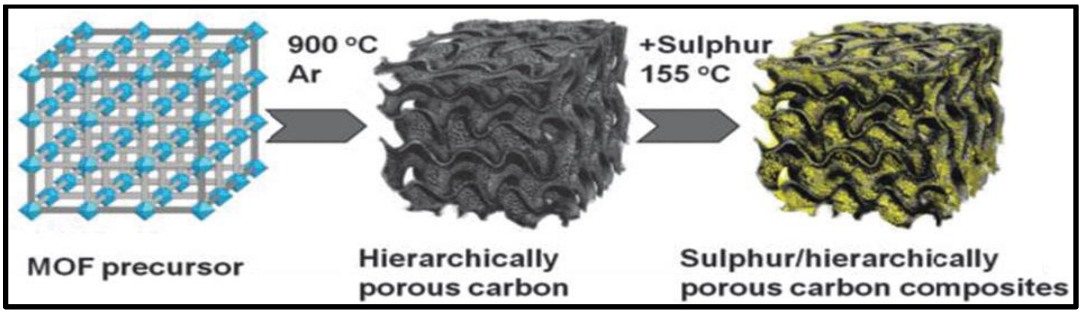

Figure 5: Scheme of sulphur-hierarchical porous carbon composite preparation (Xi et al., 2013)

Xu et al. (2015) used ZIF-8 to reach porous carbon via a similar process; they first preheated ZIF-8 crystals under nitrogen flow for 3 h and then increased the temperature from 150 °C to 300 °C for a further 2 h, and then increased and maintained at 800 °C for 4 h to reach ZIF-8 carbon black powder (ZIF-8C). After the carbonisation, the residual zinc was washed out by using HCl (35 wt.%). They showed the increase in the specific surface area carbon-derived ZIF-8 compared to the ZIF-8 precursor by measuring the surface area via BET; it increased from 949 m^2g^{-1} to 1302 m^2g^{-1} (Xu et al., 2015). Figure 6 illustrates the nitrogen-sorption isotherm for ZIF-8 and ZIF-8C.

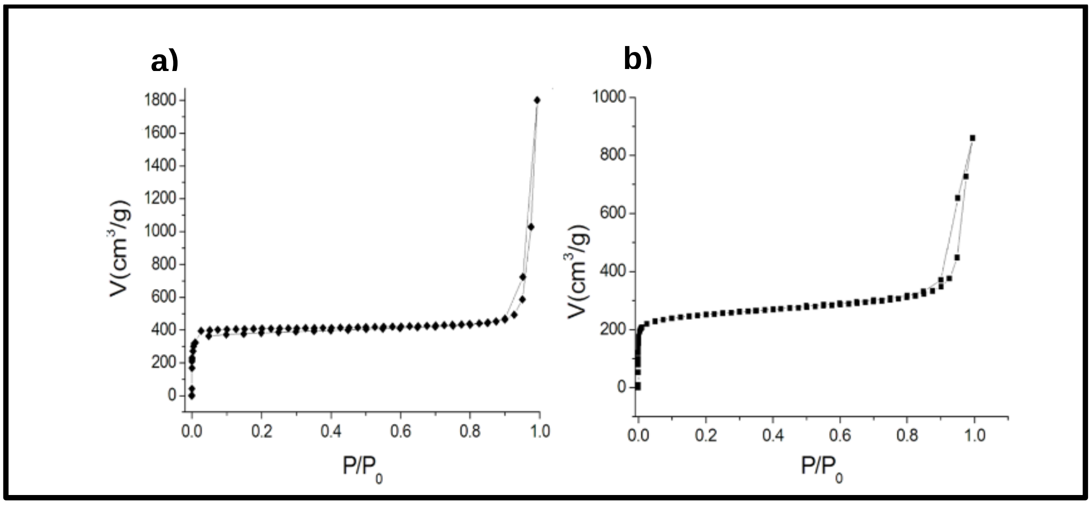

Figure 6: Nitrogen adsorption–desorption isotherms of (a) ZIF-8 and (b) ZIF-8C (Xu, 2015)

Hao et al. (2014) used another family of ZIFs to obtain MOF-derived carbons. N-PCMPs were synthesised by the direct carbonisation of ZIF-11 in a vacuum furnace at 1000 °C for 2 h with a heating rate of 5 °C/min, under a flow of nitrogen gas. Figure 7 illustrates the morphology structure of ZIF-11 and N-PCMPs. In the next step, they treated the N-PCMPs with solid KOH and then heated it at 750 °C for 1 h under nitrogen flow. They soaked the sample in HCl (1M) overnight and washed it thoroughly with DI water, and finally activated it at 60 °C under vacuum, and named it N-PCMP-A (Hao et al., 2014).

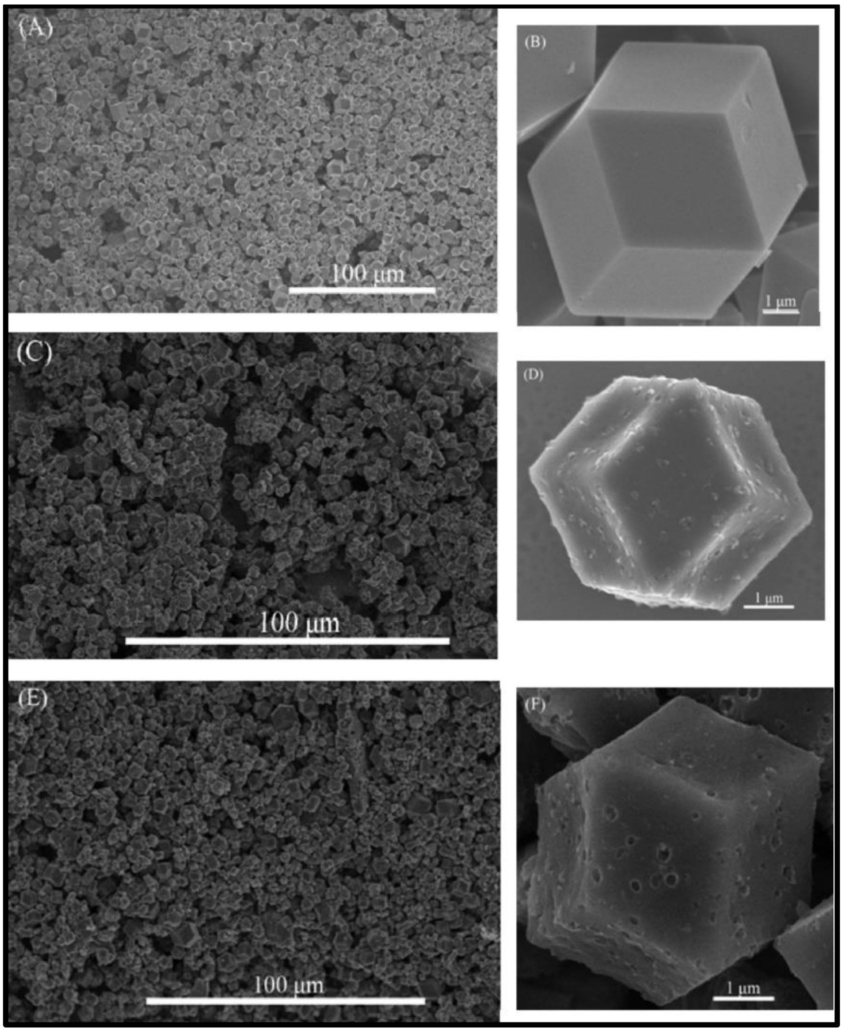

Figure 7: SEM images of ZIF-11 (A, B), N-PCMPs (C, D) and N-PCMPs-A (E, F) (Hao et al., 2014)

2.2.1 Metal organic framework-derived carbon as metal-free electrocatalysts

MOF-derived carbons have been widely investigated by many researchers (Zhao et al., 2014b) (Zhang et al., 2014a). Zhang et al (2014) reported the highly graphitic nitrogen-doped graphitic porous carbons (NGPCs) derived from ZIF-8. ‘’In a rapid carbonisation process, ZIF-8 worked as both the carbon and nitrogen sources and resulted in the NGPCs product not only retaining the morphology of the parent MOFs, but also possessing rich nitrogen, a large surface area and well-conducting network’’(Zhang et al., 2014a). Zhang et al (2014) believed that time and temperature of the carbonization plays crucial role in the electrochemical property of the NGPCs. The carbonized sample at 1000 °C and 10 h (NGPCs-1000-10), resulted high current density of 4.3 mA cm^{-2}, good ORR performance and oxygen reaction onset-potential of 0.02 V (vs. Ag/AgCl), which is just 40 mV negatively shifted compared to that of Pt/C. Zhang et claimed that ‘’The outstanding electrocatalytic activity of this metal-free catalyst is attributed to the synergetic contributions of abundant graphitic-N active sites, large surface area and high degree of graphitisation’’. (Zhang et al., 2014a)

A second source of carbon had to be introduced to the MOFs framework in order to achieve the in situ nitrogen-doped porous carbon with a large surface area and narrow pore size distribution(Yang et al., 2014) Glucose was used as the second source of the carbon by infiltration into the pores of the MOFs’ precursor zinc-benzimidazole (ZIF-7) after carbonisation at 950 °C for 5 h, the proposed nitrogen-doped porous carbon was synthesised. Adding the glucose not only improved the graphitisation degree, but also helps the removal of Zn metal and Zn compound impurities from ZIF-7, which produces a metal-free electrocatalyst for fuel cells. The bets ORR activity with the onset-potential of 0.86 V (vs. RHE) and almost four-electron selectivity (the electron transfer number is 3.68 at 0.3 V) in O_2-saturated 0.1 M KOH in comparison with ZIF-7 derived carbon was achieved by mixing ZIF-7 and glucose precursors in liquid phase which is the closest one to the commercial Pt/C. These nitrogen-doped carbons also have better methanol tolerance and stability in comparison with commercial Pt/C. Carbon source composites and MOFs with nitrogen in their structure can be used as template to make nitrogen-doped porous carbon as efficient electrocatalysts for ORR, due to their graphene-like morphology, high BET-specific surface area, and high porosity (Yang et al., 2014).‘’In order to develop more active sites on the MOF-derived nanostructured carbon, some heteroatoms (e.g. N, S,

P) can be designed doping on the MOF carbon materials, which will contribute to their electrocatalytic activity'' (Yang et al., 2014). After carbonisation of MOF-5 at 900 °C for 5 h, nitrogen and sulphur co-doped nanoporous carbon (N, S-MOFs-C) can be synthesised, where the MOF-5 is used as the template for the carbon source, nitrogen originates from urea and dimethyl sulfoxide (DMSO) is the source of the sulphur (Yoon and Moon, 2015) (Li et al., 2014b). It was revealed that the heteroatom-co-doped N, S-MOFs-C as an electrocatalyst could reduce oxygen at the relatively high onset-potential of 0.005 V (vs. Ag/AgCl) in O_2-saturated 0.1 M KOH solution and with a 3.8-electron transfer pathway, which is owing to the synergetic effect between active sites of heteroatoms N, S and C (C–Nx, C–Sx). In terms of long-term durability and methanol resistance ability, N, S-MOFs-C F exhibits good selectivity for ORR and outperforms the commercial Pt/C in the presence of methanol. By fabricating the MOFs precursors with nitrogen-containing ligands, the self-nitrogen doped nanocarbon can be arrived at after MOFs carbonisation. Generally, it should be noted that the incorporation of MOF-derived nanocarbon into the one-dimensional carbon nanotubes or two-dimensional graphene can significantly enhance the surface polarity, electrical conductivity and electron-donor tendency of the nanocarbon, resulting in an enhanced performance in the applications, especially in fuel cells electrocatalyst (Yang et al., 2014)

Yoo et al (2014) described a method to coat MOFs homogeneously, on the outer surface of carbon nanotubes(CNTs) (Yoo et al., 2014). They formed the MOF-based continuous layers on the CNTs, by just changing the concentrations of the MOFs in MOFs/CNTs composites. Also, in 2015 Ge et el, synthesised a new ORR electrocatalyst based on N-containing nano-carbon produced from an in situ grown ZIF-8/CNTs composite (Ge et al., 2015). ''This strategy delivered high-performance electrocatalysts by taking advantage of the merits of these interacting materials. The CNTs were applied as a high conductivity skeleton in the final electrocatalyst with N-nanocarbon decoration, leading to abundant catalytic sites on the CNTs' skeleton. The excellent affinity between the continuous thin N-nanocarbon layer and the CNTs' skeleton contributed to high ORR electrocatalytic activity and superior stability in the alkaline electrolyte''(Yang et al., 2014).

Wei et al (2014) has investigated the incorporation of an ultrathin layer of nanoporous carbon, in particular, nitrogen-doped nanoporous carbon, on graphene surfaces as ORR electrocatalyst (Wei et al., 2015) It was demonstrated that the combination of a nanoporous carbon thin layer on the graphene led to the formation of a N-nanocarbon/graphene/N-nanocarbon sandwich-like structure (as shown with functionalisation, high specific surface area and good electrical conductivity, all of which contribute to fast mass transport and electron transfer required by ORR. During an oxygen reduction process, graphene acts as a conductive layer to accelerate the electron transfer in the carbon matrix and allows it to readily reach the catalytic layer. The high specific surface area and nanoporous structure of N-nanocarbon/graphene nanosheets facilitate the fast transport of reactants to the active sites and the removal of corresponding products due to the short transport pathway (Zhao et al., 2016).

2.2.2 Metal organic framework-derived materials as anodes for lithium-ion batteries

Regarding the alloying-type anode materials of Li-ion batteries, one of the most serious problems is their large volume change during electrochemical cycling. An alternative strategy is to use porous materials as anodes, or introduce coating layers as a buffering matrix, including a porous carbon, carbon nanotube, graphene or polymer. MOFs are regarded as a new kind of ideal matrix for anodes. Wei's group used ZIF-8 as the coating layer on the surface of Zn_2SnO_4 (ZTO) nanoparticles to form a core/shell structure of ZTO/ZIF-8 nanocomposites(Wei et al., 2015). The electrochemical results indicate that the thin ZIF-8 coating layer can effectively enhance the performance of the composites by accommodating the drastic volume expansion of the electrode. Furthermore, MOFs are excellent precursors for the synthesis of mesoporous carbons after pyrolysis, as stated in a recent work by Han et al. (Han et al., 2015). To date, the commercial anodes for Li-ion batteries mainly focus on carbon-based materials due to their stable properties. Several novel carbon materials have been developed, including mesoporous carbon, graphene, and carbon nanotubes with higher reversible capacities than commercialised graphite (Zhao et al., 2015). As discussed above, MOFs are considered excellent reactive precursors for the synthesis of NPC materials. Regarding the organic components, heteroatoms such as sulfur, phosphorus, boron and nitrogen generally exist, which makes direct pyrolysis of MOFs an effective way of producing heteroatom-doped carbon materials.

Zhang et al (2014) reported nitrogen-doped graphene particle analogues with a high nitrogen content of 17.72 wt.%, which were directly derived from pyrolysis of a nitrogen-containing ZIF-8 (Zheng et al., 2014). Interestingly, this novel carbon anode achieved a capacity of 2132 mA h g^{-1} after 50 cycles, which can be attributed to the nitrogen-doped hexagonal lattice and edges. Thus, it can be useful to control the type and concentration of heteroatoms by choosing different organic components or additional surfactants with alternative heteroatoms. Furthermore, the ZIF-8-derived microporous carbons have also been tested as anode materials for sodium-ion batteries, and exhibit considerably higher capacity and better reversibility than mesoporous carbon (CMK-3) (Qu et al., 2014). It is believed that the small pore size of ZIF-C can significantly reduce decomposition of the electrolyte.

Aside from carbon materials, MOFs have also been widely studied as precursors for metal oxides, carbon/metal composites and mixed transition metal oxides. In 2000, Xu's group first reported an MOF-precursor route for the preparation of Co_3O_4 nanoparticles with an average diameter of around 250 nm, which is converted from cobalt-MOFs ($Co_3(NDC)_3(DMF)_4$) via a pyrolysis method in air (Liu et al., 2010b). The agglomerated Co_3O_4 nanoparticles favoured improved cycling and rate capability as Li-ion battery anodes. In another study, mesoporous nanostructured Co_3O_4 was prepared by the direct pyrolysis of MOF-71 ([Co(bdc)(DMF)]), in which the as-prepared mesoporous Co_3O_4 showed high specific surface area, reasonable pore volume and small crystallite size (Spanopoulos et al., 2015). The capacity of the porous Co_3O_4 was 913 mA h g^{-1} after 60 cycles at a current rate of 200 mA g^{-1}.

2.2.3 Metal organic framework-derived carbon for supercapacitors

In 2010, Liu’s group first employed zinc-based MOF-5 as the template NPC to be used as an electrode material for EDLCs (Liu et al., 2010a). The as-synthesised NPC exhibited a high surface area of 2872 m^2 g^{-1} and excellent electrochemical performance for an EDLC. The specific capacitance was maintained at 258 F g^{-1}, even at a current density of 250 mA g^{-1}. In addition, the influence of the carbonising temperature of MOF-5 from 530 to 1000 °C on the specific surface area, pore size distribution and electrical conductivity were studied (Liu et al., 2010a). The porous carbon derived from MOF-5 at high temperatures demonstrated ideal electrochemical performance owing to its high mesoporosity and good electrical conductivity. In their work, furfuryl alcohol was used as the carbon precursor introduced into the pores of

MOF-5 by means of furfuryl alcohol vapour. In another work, phenolic resin, carbon tetrachloride, and ethylenediamine were chosen as the carbon precursors to adjust the texture and structure of MOF-5, resulting in different pore structures (Hu, 2010).

All the porous carbons were investigated in both aqueous and organic electrolytes for electrochemical performance. The as-developed mesoporous network carbons showed excellent performance and high capacitance retention ratios, with capacitances of 271 and 156 F/g, as well as gravimetric energy densities of 9.4 and 31.2 Wh/kg in aqueous and organic electrolytes, respectively. Zeolite-type MOFs have also shown great potential for the synthesis of porous carbons (Salunkhe et al., 2014) (Hao et al., 2015); (Zhong et al., 2015) (Chen et al., 2013). NPC can be achieved through the direct carbonisation of ZIF-8 at different temperatures (Salunkhe et al., 2014). With increasing annealing temperatures, the surface area and micropore volume increases. When evaluating the electrochemical performance of the obtained samples in 0.5 M H_2SO_4 aqueous solutions, their capacitances were obviously enhanced with better carbonisation at higher temperatures (Chaikittisilp et al., 2012). Another work selected furfuryl alcohol as the additional carbon source for ZIF-8, in which an unexpectedly high surface area of 3405 m^2 g^{-1} was achieved, along with good specific capacitances of 200 F g^{-1} at a current density of 250 mA g^{-1} when used as an electrode material for EDLCs (Jiang et al., 2011). Additionally, different carbon sources, such as glucose, ethylene glycol, glycerol and furfuryl alcohol have been introduced into ZIF-7, in which the glucose modified ZIF-7 delivered the best specific capacitance (228 F g^{-1} at 0.1 A g^{-1}), high rate capability (178 F g^{-1} maintained at 10 A g^{-1}) and good cycling stability (94% capacitance retention over 5000 cycles) (Zhang et al., 2014b). It was proposed that the glucose-derived carbon helped to remove residual

Zn impurities, prevent the formation of macropores and created graphene-like structures that further contributed to the electrochemical performance (Zhang et al., 2014b).

Based on the importance of the pore’s influence, some studies have focused on the design of the specific structure of porous carbon frameworks (Yu et al., 2014) (Amali et al., 2014a). Three-dimensional hierarchical porous carbon frameworks with micro-, meso-, and macropores have been prepared by carbonisation of ZIF-8 synthesized by ultrasonication (Amali et al., 2014a). In this case, the interconnected tiny pores within larger ones are beneficial to buffer ions in order to shorten the diffusion distances of the electrolyte to the interior surfaces, further enhancing ion mobility and charge storage (Amali et al., 2014a). Another similar result has been reported by Yu et al. (Yu et al., 2014). In this study, silica colloids were embedded in the precursor and incorporated inside or between aggregated crystals. After an annealing process and removal of silica, mesopores were produced, along with the formation of micropores from intrinsic ZIF-8. The hierarchical porous carbon exhibited high capacitance, low resistance and good capacitance retention (92–97%) after 2000 cycles.

In order to combine the properties of individual ZIF-8 and ZIF-67 MOFs, core-shell ZIF-8@ZIF-67 nanocomposites have been designed by applying a seed-mediated growth technique (Tang et al., 2015). After thermal treatment of ZIF-8@ZIF-67 crystals, the authors obtained functionalised nanoporous hybrid carbon materials consisting of nitrogen-doped carbon as the cores from ZIF-8, and highly graphitic carbon as the shells from ZIF-67. As a result, the hybrid carbon material combines the advantageous properties of the individual nitrogen-doped carbon and graphitic carbon, exhibiting a specific capacitance of 270 F g^{-1}.

2.3 Immersion Calorimetry

Xylene isomers are commonly used in industry, especially in the petrochemical industry. P-xylene is one of the main elements of the manufacturing of polyethylene terephthalate, or polyester. However, the close boiling point of these isomers makes the separation process very challenging. One method to overcome this problem is to separate them through the adsorption process. Calorimetry is a technique for measuring the heat of a chemical reaction or heat capacity as well as physical changes (Moreno-Piraján et al., 2012). The word calorimetry consists of two words: calore, which means heat, and meter, which means measuring. The adsorption calorimetry usually occurs during immersion or physical adsorption. Below, different types of calorimetry instruments are discussed.

2.3.1 Reaction calorimeters

This is the standard instrument for measuring the heat of industrial processes. This instrument measures the adsorbed or released heat from the reaction inside the calorimeter.

2.3.2 Bomb calorimetry

This instrument is usually used for measuring the heat of combustion of a specific reaction. This instrument has to cope with strong pressure while the reaction is being measured. The first step is to burn the fuel, which requires electrical energy. This energy is used to heat the air around the fuel. Consequently, the air expands and while going out of the calorimeter flows through the water. This process results in the change in the temperature of the water. From this change of heat, the energy inside the fuel can be calculated. In the modern design of this equipment, fuel is pressurised by the excess of pure oxygen. Before the electrical charge begins, the fuel is immersed in the known amount of water and the temperature is measured. After the electrical charge is set up, the temperature is again measured and the change of temperature is calculated. Depending on the heat capacity of the metal bomb parts, the bomb factor can be variable. This factor is then used to determine the energy released from the burning fuel.

2.3.3 Differential scanning calorimeter

The differential scanning calorimeter uses a different method to measure the heat flow. This instrument compares the heat flow going to the sample (which is usually inside an aluminium capsule or pan) with the heat flow into the empty reference pan. In a heat flux differential scanning calorimeter, both pans are settled on a piece of material with a specific heat resistance. This part needs to have a solid design in order to provide a steady heating rate to increase the temperature of the calorimeter

The heat flow into the sample is provided by conduction during the measurements and, since the pan with the sample has a larger heat capacity, the heat flow of the sample will be greater as well. The difference of the heat flow between the two pans provides a small heat difference across the slab, which can be determined using a thermocouple. From this measurement, the heat capacity can be calculated.

2.3.4 Isothermal titration calorimeter

This instrument is mainly used in the field of biochemistry. The isothermal titration calorimeter determines the energy of biochemical reactions at a constant temperature (Freire et al., 1990). When the chemical composition of a sample changes (by the titration of the appropriate reactant), the reaction begins. In an isothermal titration calorimeter, the heat of the reaction is determined by measuring the adsorbed or released heat during a biomolecular binding event. In isothermal titration calorimeter experiments, the concentration of the anonymous reactant can be measured by applying a standard concentration of a different reactant that can react chemically with the unknown reactant. This technique is especially useful for drug discovery studies (Rajarathnam and Rösgen, 2014).

2.3.5 X-ray micro calorimeter

Mitsuda et al (2007). have reported the application of micro calorimetry in x-ray spectroscopy. When the x-ray photons are adsorbed on the material, heat pulses are generated, based on the amount of the photon energy created and the temperature increase, and the detector of the x-ray micro calorimetry senses this heat. There is a thermometer inside the micro calorimeter, which can determine the temperature change of the heat capacity of the adsorbed incident photons in x-ray range and ultraviolet visible, or even near-infrared, ranges. The first application of this technique was in the spacecraft orbiting x-ray observatory Suzaku/Astro-E2 launched in July 2005 (Mitsuda et al., 2007).

2.3.6 High-energy particle calorimeter

In particle physics, a calorimeter is a component of a detector that measures the energy of entering particles.

In the immersion calorimetry technique, the amount of heat exchanged when a solid is immersed in the liquid is measured. The heat of immersion is related to the adsorption of a layer of the liquid on the surface of the solid. The maximum value can be obtained when the interface of solid–liquid is formed during measurements when the surface of the solid is completely free.

Prior to the experiments, a solid surface needs to be outgassed under a vacuum. When the solid surface is outgassed under a vacuum before the measurement, the enthalpy of immersion mainly depends on the surface area available for the adsorbate, but also on the physical–chemical interactions between the solid surface and the vapour molecules of the liquid immersion compound. In the case of polar or heterogeneous surfaces, the heat of immersion has two contributions: the accessibility of the immersed liquid to the solid surface and the specific interactions between the solid surface and the adsorbate molecules.

We hypothesise that optimised microporosity of the electrocatalyst support as well as electrode material can lead to improved performance of the electrochemical devices and can also improve the separation ability of the MOFs.

Aim and Objectives

In this project, we aim to understand the effect of the microporosity on the performance of the PEMFC and supercapacitors, and develop knowledge to improve their performance by optimising the microporosity, as well as evaluating the adsorption ability of the MOFs for the separation of xylene isomers. Overall, this project involves the synthesis of MOFs and nanostructured carbons with controlled microporosity using MOFs as the sacrificial template, and evaluating their applications in xylene separation and electrochemical devices respectively.

The specific objectives of this project are:

- To synthesis and characterise different MOFs with different pore size distributions;
- To prepare samples for the immersion calorimetry measurements;
- To evaluate the separation ability of the MOFs with respect to the pore size and pore shape of the MOFs;

- To carbonise the synthesised MOFs under inert atmosphere and characterise the carbonised MOFS;
- To prepare Pt loaded electrocatalysts from MOF-derived carbons and use them in PEMFC;
- To prepare electrodes for supercapacitors from the carbonised MOFs; and
- To evaluate the performance behaviour of the fuel cell and supercapacitors with respect to the varying microporosity of the electrocatalyst/working electrode.

Chapter 3

3 Methodology

The main purpose of this study is to synthesise and characterise MOFs and MOF-derived carbons, evaluate their adsorption ability and assess performance of the PEMFC and Li-ion batteries affected by the microporosity of the electrocatalysts and electrodes. The first step in evaluating the electrochemical behaviour of the MOF-derived carbons is to control the porosity of the carbons used in the electrode. In order to control the pore size distribution of MOF-derived carbons, three different MOFs (with pore sizes ranging from 11 to 25 (Å)) were selected and synthesised under solvothermal conditions. Thereafter, these synthesised MOFs were characterised by BET and PXRD, then they were carbonised and characterised with BET and energy dispersive X-ray spectroscopy. Finally, their electrochemical behaviour was evaluated in PEMFC and supercapacitors by measuring their specific capacitance.

This chapter consists of eight main sections. Sections 3.1 and 3.2 describe the selected MOFs and MOF-derived carbons. Section 3.3 describes the synthesis of different MOFs (MOF-74, ZIF-8, MIL-53, MIL-100 (Al), MIL-100(Fe),MOF-5, UiO-66 and UiO-67), and the carbonisation of the synthesised MOFs is discussed in section 3.4. The application of the MOFs and their adsorption ability is addressed in section 3.5, and the characterisation of the synthesised MOFs and MOF-derived carbons are described in sections 3.6 and 3.7 respectively. Finally, section 3.8 presents their application in fuel cells and supercapacitors.

A step-by-step flowchart of this project is provided in Figure 8 below.

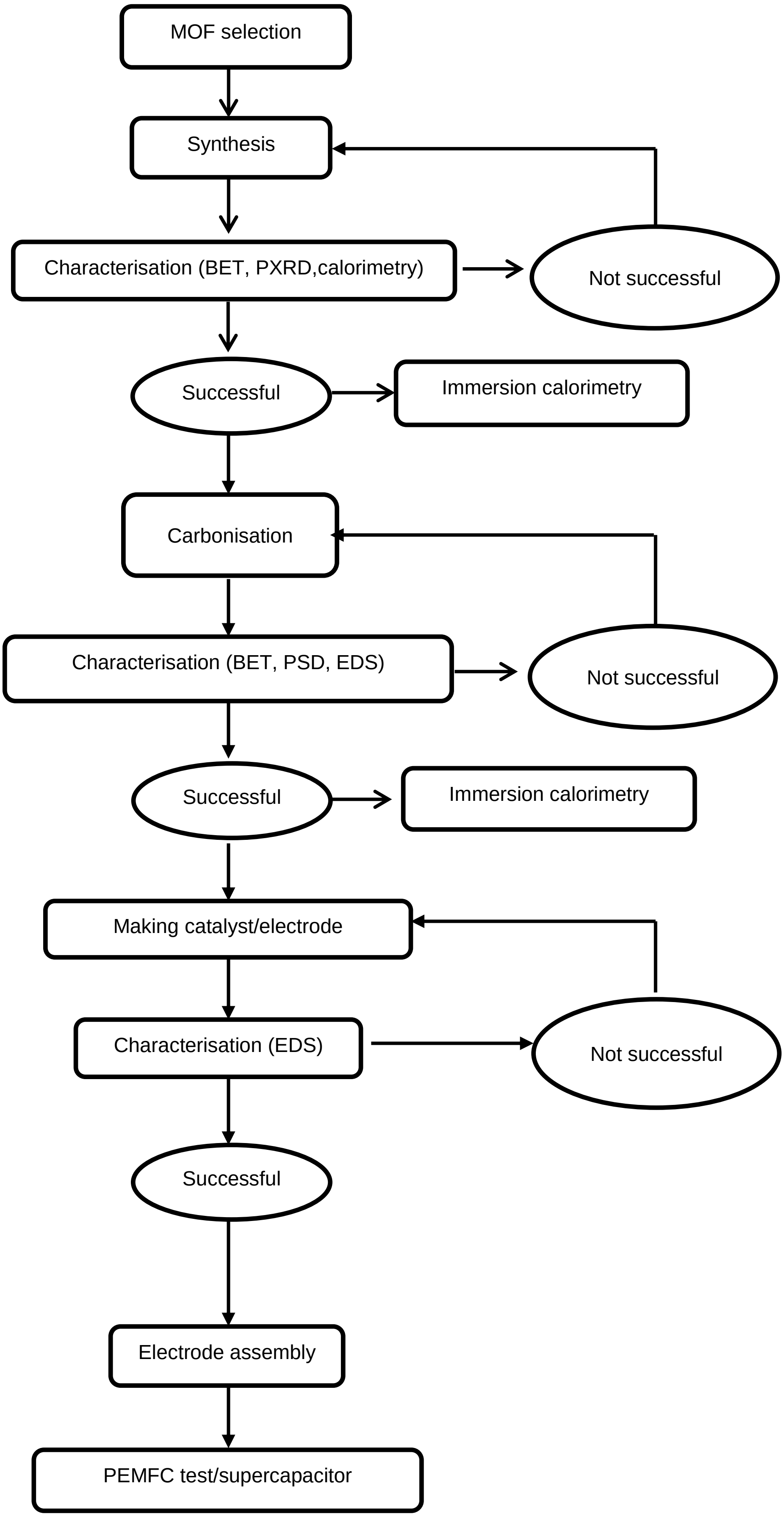

Figure 8: Flowchart of the proposed research

3.1 Metal Organic Frameworks

Details of the chosen MOFs structure with their pore diameters are given in Table 4.

Table 4: The structure and pore sizes of some MFOs

Metal-Organic Frameworks	**Pore Diameter (Å)**	**Metal cluster**	**Organic Linker**
MOF-74	11	Nickle	2,5-dihydroxyterephtalic acid
ZIF-8	11.6	Zinc	2-methylimidazole
MIL-53	8.5	Aluminium	Terephtalic acid
MIL-100	20 and 25	Iron	Trimethyl-1,3,5-benzene carboxylate
MOF-5	15	Zinc	Terephtalic acid
UiO-66	11	Zirconium	1,4-benzenedicarboxylate linkers (BDC)
UiO-67	11,22	Zirconium	BPDC4,4’-biphenyldicarboxylic acid
HKUST (purchased from Sigma-Aldrich)	3,5,8	Cupper	Benzene-1,3,5-tricarboxylic acid

3.2 Metal Organic Framework-Derived Carbon

As mentioned before, MOF-derived carbons (carbonised MOFs) are usually prepared by pyrolysis (heating selected MOFs at temperature around 600 to 800 ^{o}C under vacuum or inert atmosphere) and then activated by chemical activation. Section 3.4 focuses on the carbonisation of selected MOFs. Figure 9 schematically illustrates the carbonisation process.

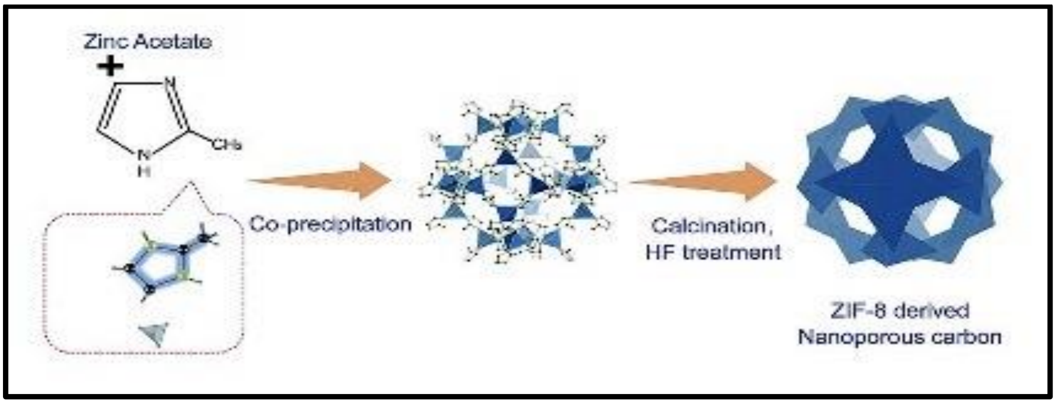

Figure 9: Schematic illustration of the carbonisation process (Salunkhe et al., 2014)

The following equipment was used in this study:

1) 7'' Square (Hotplate) Magnetic Stirrer, from Dragon Lab
2) SciQuip Oven 80-HT, from SciQuip
3) Vacuum Drying Oven Heraeus Instruments Vacutherm VT 6025
4) Vacuum Pump PC 3001 Variopro, Vario
5) Thermo Scientific Sorvall-Legend XIR Centrifuge
6) 45 ml Parr Steel Autoclave Bomb, purchased from Parr Instrument Company
7) Filter paper (125 mmØ) used as purchased from Whatman plc (Germany)
8) Tubular furnace (Alicante)
9) Balance
10) Immersion calorimetry (Setaram)

3.3 Metal Organic Framework Synthesis

All reagents were used as purchased without further purification. The DI water used in all experiments was supplied by University College London's Electrochemical Innovation Laboratory.

3.3.1 Ni-MOF-74 synthesis method

Ni-MOF-74 was hydrothermally synthesised following the method from Glover et al. (Grant Glover et al., 2011): 0.149g 2,5-dihydroxyterephtalic acid was added to 10 ml THF and 0.373 g nickel acetate tetra hydrate was added to 10 ml DI water. The two solutions were mixed together for 10 min resulting in a bright green solution. The resulting solution was transferred into the Teflon-lined Autoclave Bomb and placed in a preheated conventional oven at 110 ^{o}C for 72 h. After cooling to room temperature, the solution was filtered and washed with DI water several times. Finally, the sample was activated in a vacuum oven at 100 °C for 8 h, and stored in nitrogen atmosphere. The resulted sample weigh was 0.097 g.

Since Ni-MOF-74 and ZIF-8 have similar pore sizes, due to the low synthesis yield of MOF-74, only ZIF-8 was used for the carbonisation.

3.3.2 ZIF-8 synthesis method

ZIF-8 was synthesised solvothermally, using the method from Fu et al. (2013) with some modification: 3 g zinc nitrate hexahydrate was dissolved in 180 ml methanol. 8.3 g 2-methylimidazole was dissolved in 180 mL methanol and stirred for approximately 15 min. After all the imidazole was dissolved in the water, the solution of zinc nitrate was added to the imidazole solution, producing a milky solution, which was then stirred for 10 min at 600 rpm with the magnetic stirrer at room temperature. After mixing the two aqueous solutions of metal and linker to obtain ZIF-8 crystals, the solution was centrifuged at 12,000 rpm for 30 min. After centrifugation, the residuals were collected and washed with fresh methanol to remove unreacted methylimidazole. This process was repeated twice more. After the final washing with the centrifuge, the residue was collected and dried in a vacuum oven at 120 °C overnight. The resulted sample weight was 0.808 g. To avoid air exposure, ZIF-8 crystals were stored in a screw cap with septa thread vial under nitrogen (research grade nitrogen, purchased from BOC) (when the sample was transferred to the vial, a nitrogen-filled syringe was used to inject the nitrogen into the vial. One more needle was injected to remove the air from the vial).

3.3.3 MIL-53(Al) synthesis method

MIL-53(Al) was synthesised hydrothermally under autogenous pressure following the Khan et al. (2011) method: 2.244 g of aluminium chloride hexahydrate ($AlCl_3.6H_2O$) was added to 0.830 g of terephtalic acid, 14.41 mL DI water was added to the mixture and stirred for 5 min using a magnetic stirrer at 600 rpm. The aqueous solution was then transferred into a 45 mL Teflon-lined autoclave, sealed and placed in the centre of a conventional oven at 200 °C for 180 min. After cooling to room temperature, the precipitated white powder was collected by filtration using Grade 1 filter paper (Whatman, 125 mm), followed by washing with DI water several times to remove the residue of terephtalic acid. Finally, after activation at 150 °C for 5 h, the sample was collected and stored in thread vial under nitrogen atmosphere. The obtained sample weight was 0.851 g.

Since the synthesis of this MOF was not successful, we did not use this MOF for further experiments.

3.3.4 MIL-100(Al) synthesis method

MIL-100(Al) was synthesised solvothermally under autogenous pressure following the method of Volklinger et al. (Volkringer et al., 2009) with some modification. The chemical reagents that we used were aluminium nitrate nonahydrate Al $(NO_3)_3$.9H2O, ≥ 98%, and trimethyl-1, 3, 5-trimesate $(CH_3O)_3\,C_6H_3$, (Me_3BTC), 98%, both purchased from Sigma-Aldrich.

0.69 g of aluminium nitrate nonahydrate was added to 0.312 g trimethyl 1,3,5-benzenetricarboxylate. 2.31 mL of 1M nitric acid (HNO_3 (1M)) was added drop wise to 8.4 mL DI water and the mixture of aluminium nitrate nonahydrate and 3-methylbenzene tricarboxylic was dispersed in diluted nitric acid solution. The solution was then loaded into the 45 mL Teflon-lined Autoclave Bomb and put in the centre of the oven for 240 min at 210 °C. After cooling to room temperature, the pale-yellow powder was collected by filtration followed by washing with DI water to remove excess reagent. After drying overnight in room temperature, MIL-100 was activated following the method from Jeremias et al. (Jeremias et al., 2012). As-synthesised MIL-100(Al) was dispersed in 30 mL N, N Dimethylformamide (DMF) and stirred for 1 h followed by centrifugation for 10 min at 10,000 rpm, and was again dispersed in fresh 30 mL DMF and stirred overnight. Then the sample was centrifuged off, the same procedure was repeated with ethanol (sample first dispersed in 30 mL ethanol for 1h and then after centrifugation, the sample was immersed in 30 mL ethanol overnight and collected by centrifugation), and finally the sample was activated under vacuum at 120 °C overnight. The collected sample was stored under nitrogen atmosphere in thread vials. The obtained sample weight was 0.284 g.

3.3.5 MIL-100(Fe) synthesis method

MIL-100(Fe) was synthesised following the method of Shi et al. (2013), with some modifications(Shi et al., 2013). In a 25 mL round bottom flask, 4 g of $Fe(NO_3)_3$ was added to 6 mL UHP water and then 1.9 g of BTC was added to the solution. The flask was then connected to the reflux and was kept under stirring for 12 h at 95 °C. Once the reaction was complete, the remaining liquid was separated using filtration and the sample was washed thrice with DI water and thrice with ethanol. Finally, the sample was dried in air at room temperature. The sample weigh was 0.639 g.

3.3.6 MOF-5 synthesis method

MOF-5, also called IR-MOF-1, was hydrothermally synthesised following the method provided by Srinivas et al. (2014), with some modifications (Srinivas et al., 2014). 6.3 g of zinc nitrate hexahydret and 1.35 g terephtalic acid was added to 300 mL N,N dimethylformamide using a magnetic stirrer. The solution was stirred at 600 rpm for about 15 min. The solution was then transferred to a 500 mL Duran glass jar and loaded to the oven at 100 °C for 2 days. After the solvent cooled down to the room temperature, the sample was filtered off and washed with fresh DMF several times (950 mL). Finally, to extract the trapped DMF from the pores of the sample, it was soaked in chloroform for 5 days, where the chloroform was changed every day. Lastly, the sample was dried at 200 °C under vacuum and stored under nitrogen before N_2 sorption isotherms. The sample weight after the activation was 1.35 g.

3.3.7 UiO-66 synthesis method

UiO-66 was hydrothermally synthesised following the Katz et al. (2013) method with some modifications (Katz et al., 2013). Following the typical synthesis method, 125 mg of zirconium chloride ($ZrCl_4$) was loaded into a glass vial. 1 mL concentrated HCL and 5 mL DMF was added to the solution and sonicated for 20 min at room temperature. Then, 123 mg of 1,4-benzenedicarboxylate and 10 mL DMF was added to the solution, sonicated for another 20 min and loaded into the conventional oven at 80 °C overnight. Thereafter, the sample was filtered and washed thrice with DMF and thrice with ethanol. Finally, the sample was dried under vacuum at 90 °C and activated at 150 °C. The weight of the obtained sample was 0.113 g.

3.3.8 UiO-67 synthesis method

UiO-67 was hydrothermally synthesised following the Katz et al. (2013) method with some modifications (Katz et al., 2013). Using the typical synthesis method, 67 mg of zirconium chloride ($ZrCl_4$) was loaded into a glass vial. 0.5 mL concentrated HCL and 5 mL DMF was added to the solution and sonicated for 20 min at room temperature. Then, 90 mg of 4,4'-biphenyldicarboxylic acid (BPDC) and 10 mL DMF was added to the solution, sonicated for another 20 min and loaded into the conventional oven at 80 °C overnight. Thereafter, the sample was filtered and washed thrice with DMF and thrice with ethanol. Finally, the sample was dried under vacuum at 90 °C and activated at 150 °C. The weight of the obtained sample was 0.101 g.

3.4 Carbonisation

There are different methods to derive MOF template carbons, but the two most popular methods are direct carbonisation and carbonisation followed by chemical washing. The critical parameters in the carbonisation process are to conduct the experiment under an inert atmosphere and have a stable flow of inert gas (usually Ar or N_2). In order to evaluate the performance of the MOF-derived carbons as electrodes/electrocatalysts in supercapacitors and fuel cell industries and their adsorption ability in the separation industries, it was crucial to remove all the metal parts in the MOFs' structure during the carbonisation process. Any metal parts left in the MOF-derived carbons structure can interact with the adsorbate and decrease the surface area of the carbon, hence decrease the available sites of the adsorption. In addition, the interaction of the metals with the adsorbate might result in fake high enthalpy of adsorption.

In the first method, is sample was only heated under an inert atmosphere to the temperature above the boiling point of the metal salt, to evaporate the metal into a sample. In the second method, the sample is usually heated to up to 800 °C and then the metal is washed out with a chemical solvent such as KOH or HF. In this research, we used both methods for different materials. During the carbonisation, the precursor MOF kept its structure while all the metal parts of the MOF evaporated and the organic linkers turned to carbon.

3.4.1 ZIF-8 carbonisation

3 g of synthesised and activated ZIF-8 was transferred to an alumina boat and placed in the centre of the horizontal tubular furnace (Carbolite: STF16/75/450) under Ar flow at 100 ml/min for 2 h. The furnace was then increased to 1100 °C with a 5 °C/min ramping rate. It remained at that temperature for 6 h. After cooling to room temperature, the sample was collected and weighed. The obtained mass was 0.64 g. The carbonized ZIF-8 was then characterised using N_2 adsorption isotherm in fully automated manometric equipment.

The experimental set up for the carbonisation is given in Figure 10.

Figure 10: Experimental set up for carbonisation

3.4.2 MOF-5 carbonisation

MOF-5 was directly carbonised following Segakweng et al. (2016), with some modifications (Segakweng et al., 2016). 3.0187 g was transferred to the alumina boat and placed in the centre of the furnace under Ar flow for 2 h with the flow rate of 100 ml/ min. The furnace was ramped to 1100 °C at 3 °C/min and remained at that temperature for 6 h. After cooling to room temperature, the sample was collected and weighed. The weight of the sample was 0.48 g.

3.4.3 MIL-100(Fe) carbonisation

MIL-100(Fe) was carbonised following the Mao et al. (2015) method with some modifications (Mao et al., 2015). 2.15 g of MIL-100(Fe) was transferred to an alumina boat and placed in the centre of the horizontal tubular furnace. Argon was purged with 65 ml/min flow rate for 2 h before starting the heating process. After 2 h, the furnace was programmed to increase to 1000 °C with 5 °C/min and remain there for 4 h. After cooling to room temperature, the sample was collected. To remove the Fe from the carbon, the carbonised sample was soaked in 25 mL of 5 M HCl and stirred for 24 h at 400 rpm. Finally, the sample was filtered and washed with DI water and ethanol and dried overnight in air. The obtained weight of the sample was 0.422 g.

3.4.4 UiO-66 carbonisation

In order to evaluate the adsorption ability of the UiO-66 derived carbon, 2.52 g of UiO-66 was placed in the alumina boat in the centre of the furnace. The carbonisation was conducted under Ar starting at room temperature for 2 h and then heated to 1100 °C with a 5 °C/min ramping rate. The sample remained at that temperature for 6 h and was kept under Ar flow until it cooled down to room temperature. Then sample was collected and dissolved in 5 M HCl and stirred overnight at room temperature. Then, the sample was collected by filtration and washed thrice with DI water and ethanol. The weight of the sample after washing was 0.314 g.

Since the result from the carbonised UiO-66 was not promising, we decided not to repeat the experiments for carbonised UiO-67.

3.4.5 HKUST carbonisation

3.09 g of commercial HKUST was transferred to the alumina boat and placed in the centre of the furnace. Argon was purged with 100 ml/min flow rate for 2 h before starting the heating process. The furnace was heated up to 100 °C with a 5 °C/min ramp rate and remained at that temperature for 6 h. After cooling to room temperature, the sample was collected. The weight of the sample after the carbonisation was 0.945 g.

Since the synthesis of the MIL-53 and MIL-110(Al) was not successful, these MOFs were not used in this study, hence they were not carbonised.

3.5 Immersion Calorimetry

Four different MOFs (commercial ZIF-8, commercial HKUST, UiO-66 and UiO-67) were selected to evaluate their separation ability of xylene isomers (M-xylene, P-xylene, O-xylene).

3.5.1 Heat of adsorption measurements

The exothermic peak from the equipment corresponds to the contact of the immersion liquid with the sample. Thus, the enthalpy value obtained after the experiment (Q_{exp}) has been corrected to obtain the value of the real enthalpy (ΔH_{imm}), using the value of the vaporisation energy of the immersion liquid, ΔH_{vap}.

Equation 1

$$Q_{exp} = \Delta H_{imm} + \Delta H_{vap}$$

Equation 2

$$\Delta H_{vap} = \Delta h_{vap}(P_0/RT)$$

where Δh_{vap} is the molar vaporisation energy, P_0 is the saturation pressure of adsorbate, V is the dead volume of the bulb, T is the temperature of the experiment and R is the ideal gas constant (Silvestre-Albero et al., 2001).

3.5.2 Sample preparation

First, an empty sample tube was weighed and the weight (m_1) was noted. Then, 80 to 100 mg of the sample was transferred to the tube and the weight of the sample and the tube (m_2) was noted. Some glass wool was put in the middle of the stem to prevent the sample flying to the degasification system during degassing, and its weight (m_3) was noted. The special key was then connected to the sample tube, which keeps the sample under vacuum after removal from the degassing equipment. The next step was to degas the samples at 110 °C overnight with a 5 °C/min ramp rate.

Figure 11 shows a sample tube loaded by the commercial HKUST-1. The tube consists of three main parts; the stem, bulb and the tip at the bottom of the bulb. After samples were degassed in order to vacuum seal the samples, the bulb of the tube needed to be separated. A flame torch was used to separate the stem from the bulb so that the whole system was kept under vacuum. Then, the weight of the stem and the bulb together was measured, as well as the bulb alone (m_4 and m_5 respectively).

The bulb was attached to the sample holder of the calorimeter and immersed in the stainless-steel cell containing the solvent (xylene isomers). The cell was then transferred to the calorimeter. The equipment was set to run the test at 30 °C for 6 to 12 h. This timing varied, based on the required time for the equipment to reach equilibrium. Once equilibrium in the calorimeter chamber was reached, the tip at the end of the bulb was broken, allowing the sample to immerse in the liquid and get wet. The released heat was recorded as a function of time. The results were plotted and, from the integration of the area under the curve, the heat of adsorption was measured. Then, using Equation 3, the corrected heat of adsorption was calculated.

The detailed results are given in Chapter 6.

Equation 3

$$\log_{10} P = A - \left(\frac{B}{C + T}\right)$$

where P corresponds to vapour pressure, A, B and C are Antoine constants and T is temperature (°C) (Thomson, 1946).

Table 5 describes the details of the experiments and the calculation of the heat of adsorption.

Table 5: Description of the experimental details

Description	
m_1	empty bulb
m_2	bulb + sample
m_3	bulb + sample + wool before degassing
m_4	bulb + sample + wool after degassing
m_5	bulb + sample after cutting the bulb
m_6	bulb weight after the experiment
Density (g/cm^3)	ρ
Degassed weight (g)	$W_{clean} = (m_2 - m_1) - (m_3 - m_4)$
Solvent mass (g)	$M_{sol} = (m_6 - m_5)$
Solvent volume (l)	$V_L = ((\text{Solvent mass}/\text{Density})/1000)$
A	7.14914
B	1566.59
C	222.671
$\Delta H_{vap.}$ (kJ/mol)	45
T experiment (°C)	30
P_o (atm)	$10^{(A-(b/C+T))}/760$
Dissolved moles evaporated	$\text{moles}_{dissolved} = (P_o x V_L)/(0.082xT+273.15)$
Heat of evaporation (mJ)	$H_{evap} = \text{moles}_{dissolved} \times \Delta H_{vap.}$
Released heat (J/g)	Integration of the area under curve
Released heat (mJ)	Area under curve x W_{clean}x1000
Heat of adsorption (mJ)	$H_{ads} = H_{evap} + H_{imm}$
Corrected heat of adsorption (J/g)	$(H_{ads}/W_{clean})/1000$

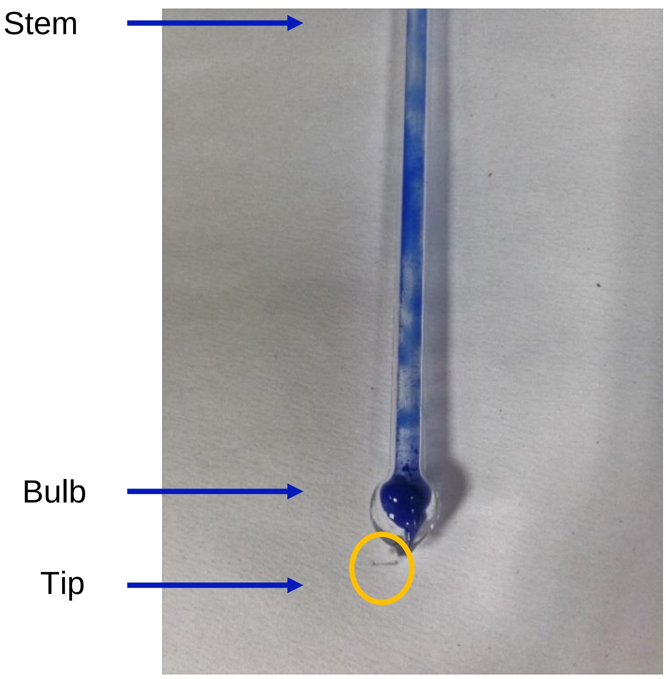

Figure 11: Calorimetry tube

Table *6* shows the amount of each MOF used in different xylene isomers. The results are provided in Chapter 6.

Table 6: Experimental details of the tested MOFs in xylene isomers

MOF/CMOF (mg)	Solvent (9mL)		
	O-Xylene	M-Xylene	P-Xylene
HKUST-1	91.6	100	109
ZIF-8	98.4	98.3	91.5
UiO-66	163	85.1	97.5
UiO-67	80.5	70.6	79.8
C-UiO-66	-	156	-
C-HKUST	-	86.4	-

3.6 Characterisation of Metal Organic Frameworks

The synthesised MOFs were characterised using a powder X-ray diffractometer to identify the crystallinity of the synthesised MOFs. The BET theory was used to measure the pore size distribution using t-plot method and surface area using nitrogen adsorption–desorption isotherm.

3.6.1 Bruanauer-Emmett-Teller surface area analyser

The specific surface areas of the MOFs were calculated using the BET equation. In 1938 Stephen Brunauer, Paul Hugh Emmett and Edward Teller first published the theory of BET, which analyses the physical adsorption of a gas adsorbate on a solid adsorbent. This method is the improved model of the Langmuir[2] theory for multilayer adsorption, which means each molecule adsorbed on the surface of the sample can be considered an adsorption site for the new layer adsorption of the molecule. The gas used in the experiments need to be nonreactive, hence N_2 is the most common gas used in this technique. The BET equation is:

---

[2] Langmuir is the theory of adsorption on the monolayer samples.

Equation 4

$$\frac{p}{n(p_0 - p)} = \frac{1}{n_m C} + \frac{C - 1}{n_m C} \times \frac{p}{p_0}$$

where p_0 is the equilibrium pressure, p is the saturation pressure, C is the BET constant and $\mathrm{n_m}$ is the number of the gas molecules adsorbed.

Equation 5

$$C = \exp(\frac{E_1 - E_L}{RT})$$

where E_1 is the heat of adsorption for the first layer, and E_L is the liquefaction energy.

To calculate the surface area, first we needed to plot the BET plot using the $(P/P_0)/[n\ (1-P/P_0)]$ as the y-axis and P/P_0 as the x-axis, resulting in a straight line from which the slope ($s = (C - 1/n_m)$) and intercept ($i = 1/n_m\ C$) were calculated and used in the Equation 8 to calculate the BET surface area (S_{BET}).

Equation 6

$$C = (^{s}/_{i}) + 1$$

Equation 7

$$n_m = 1/(^{s}/_{i})$$

Equation 8

$$S_{BET} = n_m\ L\sigma$$

where L is Avogadro constant (6.022140857 × 10^{23}), and **σ** is the average area of each molecule of adsorbate occupies. This value for N_2 at 77(K) is 0.162 nm^2 (Rouquerol et al., 1999).

The BET surface area and pore volume of the synthesised MOFs were measured by a BET surface area analyser (Micromeritics' Tri-Star surface area and porosity analyser). First, 0.1-0.2g of each MOF were loaded into the glass loop and into the out-gas port of the BET surface area analyser to be evacuated at a specific temperature overnight. After degassing, the samples were quickly transferred to the analysis port, the Dewar was filled with the liquid nitrogen and the analysis began.

3.6.2 Powder X-ray diffraction

PXRD is a useful structural characterisation technique for phase identification of crystalline materials such as MOFs. There are three main parts in the XRD system; the X-ray tube, sample holder and X-ray diffractometer. The principle of the XRD is based on the generation of X-rays by a cathode ray tube (a filament inside the cathode tube is heated and produces electrons, which are accelerated to the sample by applying voltage, bombarding the sample). When the electrons have gained enough energy, they are ejected from the inner shell and travel to the next shell. The diffractometer produces waves using X-rays with a known frequency. From the interaction of the waves with the sample, atoms of the sample generate light at a specific angle (the diffraction angle). This happens when the conditions satisfy Bragg's law.

Equation 9

$$n\lambda = 2d\ sin$$

where d is the distance between atomic layers of the sample, λ is the wavelength of the incident X-ray beam, θ is the scattering angle and n is a positive integer.

Then, the sample was scanned at the range of 2 θ to determine all the diffraction directions of the lattice; the diffracted waves were detected, processed and counted. Since each mineral had unique d-spacing, by converting the diffraction peaks to d-spacing the minerals could be determined (Feidenhans'l, 1989).

In order to determine the crystallinity of the synthesized MOFs, samples were characterised by PXRD (Bruker-AXS machine using Cu Kα radiation (λ = 1.5418 Å)). The transition mode for all samples was in the range of $5^o \leq 2\ \Theta \leq 50^o$. The scan rate and step size/width for all samples were: 2s/step and 0.05^o respectively.

3.7 Characterisation of Carbonised Metal Organic Frameworks

The morphology and structure of the MOF-derived carbons were characterised with XRD, BET surface area analysis and energy dispersive spectroscopy (EDS) analysis.

3.7.1 BET measurements

MOF-derived carbons were characterised with nitrogen at 77 K to measure the surface area, pore volume and pore size distribution. The detailed results of the samples are provided in Chapter 4.

3.7.2 Scanning Electron Microscopy and Energy Dispersive Spectroscopy

Scanning electron microscopy (SEM) is a useful and common tool for measuring different properties of MOFs, including elemental composition and crystal size. However, since MOFs have an insulating nature, in order to be used in SEM it is required for them to be coated with a conducting material such as gold (Howarth et al., 2017). The principles of SEM are based on beaming accelerating electrons onto the sample. Diffracted backscattered electrons are used for determination of the crystal structure of the sample as well as the orientation of the minerals. In SEM, secondary electrons are detected when the atoms are excited by the electron beam. The image of the sample is produced by collecting the emitted secondary electrons with the help of a special detector (McMullan, 1995).

EDS is an elemental analysis method that can be paired with SEM to evaluate elemental analysis. However, it is important to consider the coating material used for SEM analysis, as this may result in overlap with the peaks from the metal within the samples, resulting in inaccuracy in the results (Pearce, 2004).

In this study, to assess the carbonisation process, MOF-derived carbons and Pt/C-ZIF-8 were characterised with SEM and EDS elemental analysers. To prevent any error in the quantitative results, in the case of the EDS analysis, samples were not coated, whereas coating was applied in SEM analysis (JEOL, JSM-6480 LV, SEM). The detailed results are given in the next chapter.

3.7.3 Transmission electron microscopy

Transmission electron microscopy (TEM) is a light microscopy technique that consists of three main parts; electron gun to produce electron beam; image producing system, which consists of movable sample holder and objective lens; and the image recorder, which is responsible for converting the image of the electron into an observable format. This technique is based on the interaction of the transmitted electrons and the sample. When the electron beams are transmitted to the sample, under vacuum, based on the wavelength of the electrons, the speed of the electrons varies: the shorter wavelengths are faster and consequently result in a higher quality of the image. When a great number of electrons transmit through the sample, they produce a light area in the image, and where the sample is denser, the image is darker (Williams and Carter, 1996).

In order to study the morphology of the sample in this study, they were characterised by TEM analyser (JEOL, JEM-1010). The results are provided in Chapter 4.

3.8 Electrochemical Measurements

3.8.1 Fuel cell tests

In order to apply C_{ZIF-8} in fuel cells, they need to be loaded by a catalyst such as Pt. Two different methods were used for the catalyst preparation. In the first attempt, the microwave-assisted synthesis method given by Chen et al. (2012) was followed. In this method, 2 mL of 0.05 M aqueous solution of H_2PtCl_6 was added to 50 mL ethylene glycol, and the pH of the sample was adjusted to 9.5 by adding 0.5 mL of 0.8 M aqueous KOH. Then, 0.080 mg of the carbonised ZIF-8 was added to the solution, which was ultra-sonicated for 1 h. Thereafter, the solution was placed in the centre of the microwave oven and heated for 60 s at 800 W (CEM, MARS). The solution was filtered off and the residue was washed several times with acetone and DI water. The sample was then dried under vacuum at 100 ºC overnight. The sample was characterised by EDS to measure the amount of Pt loaded. The detailed results are given in Chapter 5. The nominal value for the Pt loading is 20% Pt and 80% carbon. Since the result obtained from the first attempt was not successful, a different method was followed.

In the second method, the Pt/C was synthesised using the method provided by Yang et al. (2003): 0.132 g of H_2PtCl_6 was mixed with 30 mL ethanol using a shaker for 30 min, and then 0.2 g of the carbon was added to the solution and ultra-sonicated for 1 h. Thereafter, the solution was stirred at 60 °C on the magnetic stirrer for 45 min (until the solvents evaporated). Then, the sample was transferred into a conventional oven for 20-30 min. Thereafter, the sample was left exposed to air under a fume cupboard for 3 days to completely dry. After three days, the sample was transferred to a ceramic crucible and put in the furnace (the furnace was set to 120 °C with the ramp rate of 5 °C/min) under N_2 atmosphere with the flow rate of 1 L/min starting at room temperature. After the temperature reached 120 °C, the H_2 was blown into the furnace with the flow rate of 70 mL/min, and kept at that temperature for 2 h. The sample was finally collected, and the yield was 0.217 g $Pt_{20\%}/C_{ZIF\text{-}8}$.

The same procedure was repeated for loading Pt on Vulcan XC-72 to be used as the reference. 0.131 g of H_2PtCl_6 was added to 30 mL ethanol and mixed in the shaker for 30 min, 0.2 g of support (Vulcan) was added to the sample and the solution was ultra-sonicated for 1 h. The solution was then placed on the magnetic stirrer for 45 min at 60 °C (at this stage, the ethanol had almost evaporated, so we put the sample in a conventional oven for only 5 min). Thereafter, the sample was left to dry in the air for 3 days. After 3 days, the sample was transferred to the ceramic crucible and placed in the centre of the tubular furnace to be purged with N_2 (flow rate of 1 L/min) and heated to 120 °C with a 5 °C /min ramping rate. After reaching the targeted temperature, the H_2 was purged to the sample with 70 mL/min flow rate, remaining at that temperature for 2 h.

Figure 12 illustrates the Pt/C after stirring on the magnetic stirrer (a) and the collected sample from the furnace (b).

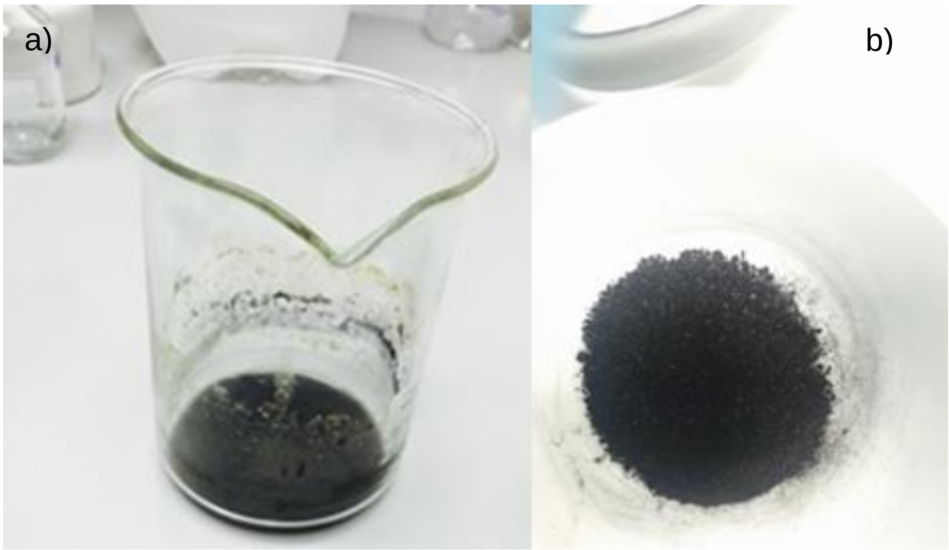

Figure 12: a) Pt/C after stirring, b) Pt/C collected from furnace

3.8.1.1 Catalyst ink solution and electrode preparation

The electrochemical activity of the Pt-loaded carbonised MOF (Pt/C_{ZIF-8}) was evaluated by the rotating disk electrode (RDE) method in a standard three-electrode electrochemical cell. The first step for this experiment was to clean the electrode and make an ink from the catalyst and load it onto the surface of the electrode. The procedure of making the catalyst ink and loading it on the electrode is described below.

3.8.1.2 Electrode cleaning

A 0.05 µm particle suspension of Al_2O_3 was poured onto a polishing cloth, and the electrode was polished on the cloth in 8 patterns several times (around 5 min), then rinsed with plenty of DI water and dried in air for at least 30 min. Finally, the electrode was mounted on top of the spinner to be loaded by the catalyst ink. Figure 13 shows the working electrode mounted on the spinner.

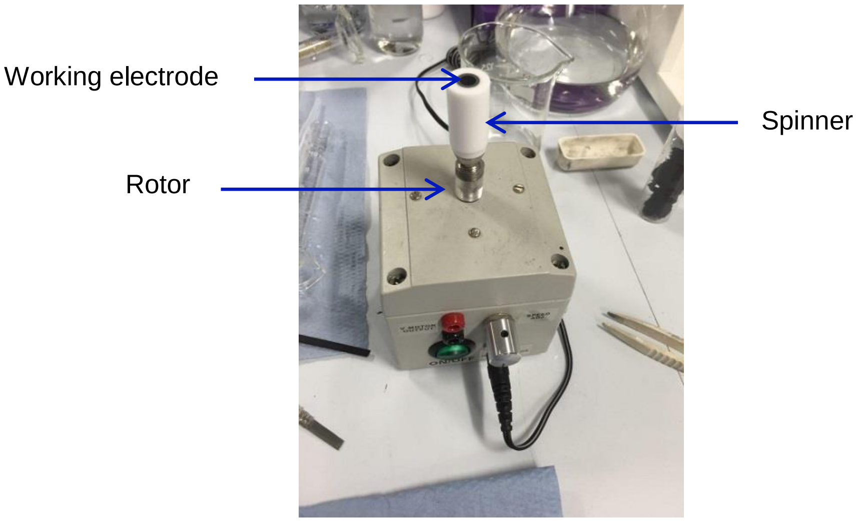

Figure 13: Working electrode mounted on the spinner

3.8.1.3 Catalyst ink preparation

5 mg of the Pt/C_{ZIF-8} and 5 ml of a solution containing 25% isopropyl alcohol (Goriparti et al.), and 0.02% Nafion were sonicated for 30 to 60 min in a small vial to obtain a well-dispersed solution before being loaded onto the electrode. 25 µL of the ink was then poured drop-wise onto the surface of the electrode. For this step, 5 µL of the ink was dropped on the surface of the electrode and the electrode was spun for about 5 min so that the ink could dry. This process was repeated 5 times until a total amount of 25 µL was loaded. After the final dropping, the electrode was left spinning for about 1 h so that the surface of the electrode was completely dry and ready to be loaded onto the electrochemical cell.

3.8.1.4 Cyclic voltammetry

Prior to using the electrochemical cell, it needed to be cleaned; for this reason, the cell was filled with H_2SO_4 (99.9%) and left overnight at room temperature. It was then rinsed several times with DI water to remove any acid from the cell. Thereafter, it was filled with the electrolyte (the electrolyte used here was $HClO_4$) and the reference and counter electrode was assembled in the cell, as well as the working electrode.

The working electrode was assembled to the shaft of the rotator system and inserted into the electrolyte. It is important to keep the working electrode at the same height in all the experiments to have the same resistance in the working electrode, along with the reversible H_2 electrodes (RHE) lugging capillary. Ultra-pure N_2 was purged to the electrolyte for more than 20 min with a 200 mL/min flow rate to deoxygenate the electrolyte.

The RDE was conditioned for 0.05–1.2V, 500 mV/s and 50 cycles at room temperature under N_2 atmosphere. The scan range was set to 0.025–1.2V and the scan rate was 20 mV/s. The number of scans was set to 3, of which the third was used for analysis. Before beginning the cyclic voltammetry (CV) test, the working electrode needed to be electrochemically cleaned via potential cycling, which was done between 0.05–1.2 V for 50 cycles with a scan rate of 500 mV/s.

This test was done both for the synthesised Pt/$C_{ZIF\text{-}8}$ and the commercial Pt/Vulcan (purchased from Sigma-Aldrich) and the electrochemical surface area (ECSA) was calculated using Equation 10 (Garsany et al., 2010). The results are provided in Chapter 5.

Equation 10

$$\mathrm{ECSA}_{\mathrm{Pt,cat}} = \left[\frac{Q_{\mathrm{H\text{-}adsorption}}\ (\mathrm{C})}{210\ \mu\mathrm{C\ cm_{Pt}}^{-2}\ L_{\mathrm{Pt}}\ \mathrm{mg_{Pt}cm^{-2}}\ A_g\ (\mathrm{cm}^2)}\right] \times 10^5$$

where $Q_{H\text{-adsorption}}$ (C) is the hydrogen adsorption charge in the negative going potential, L_{Pt} $mg_{Pt}cm^{-2}$ is the working electrode Pt loading ($mg_{Pt}cm^{-2}$), the charge of full coverage for clean polycrystalline Pt is 210 µC cm^{-2}, which is used as the conversion factor, and A_g is the geometric surface area of the glassy carbon electrode (Garsany et al., 2010).

3.8.1.5 Oxygen reduction reaction

In order to measure the specific activity of the sample, the ORR test was run. The first step was to replace the N_2 with O_2. O_2 was purged to the electrolyte for about 30 min prior to start the analysis. The rotation speed was set on 400, 800, 1200, 1600 and 2000 rpm. The scan range was set to -0.01–1.00V and the scan rate was 20 mV/s. The number of scans was set to 2, of which the second was used for analysis.

The specific activities of the Pt area were measured by calculating the kinetic current ($I_{k,}$ A), and normalising it to the electrochemical surface area of the Pt using Equation 11 (Garsany et al., 2010).

Equation 11

$$I_s(\mu A\ cm_{Pt}^{-2}) = \frac{I_k(A)}{Q_H(C)/210\ \mu C\ cm_{Pt}^{-2}}$$

where I_S is the specific activity and I_K (A) is the kinetic current.

3.8.1.6 Durability test

In order to measure the electrochemical stability of the $Pt/C_{ZIF\text{-}8}$, an ink solution of the catalyst was prepared, as mentioned in section 3.8.1.3. 35 µl of the solution was dropped onto the working electrode. The electrode was then assembled onto the shaft of the rotator system and inserted into the electrolyte. Before starting the test, N_2 was purged to the electrolyte for at least 30 min with 500 ml/min flow rate. The scan rate was set to 100 mV/s, and the scan range was set to1.0–1.6 V and the measurements were done in 10, 100, 200, 500, 1000, 2000, 4000 and 6000 cycles.

The electrolyte used was 0.1 M $HClO_4$ and the rotating ring-disk electrode (RRDE) used was polished glassy carbon with the geometric surface area of 0.2475 cm^2. The reference electrode used in this test was RHE. The analysis of the results is given in Chapter 5. Figure 14 shows the electrochemical cell set up.

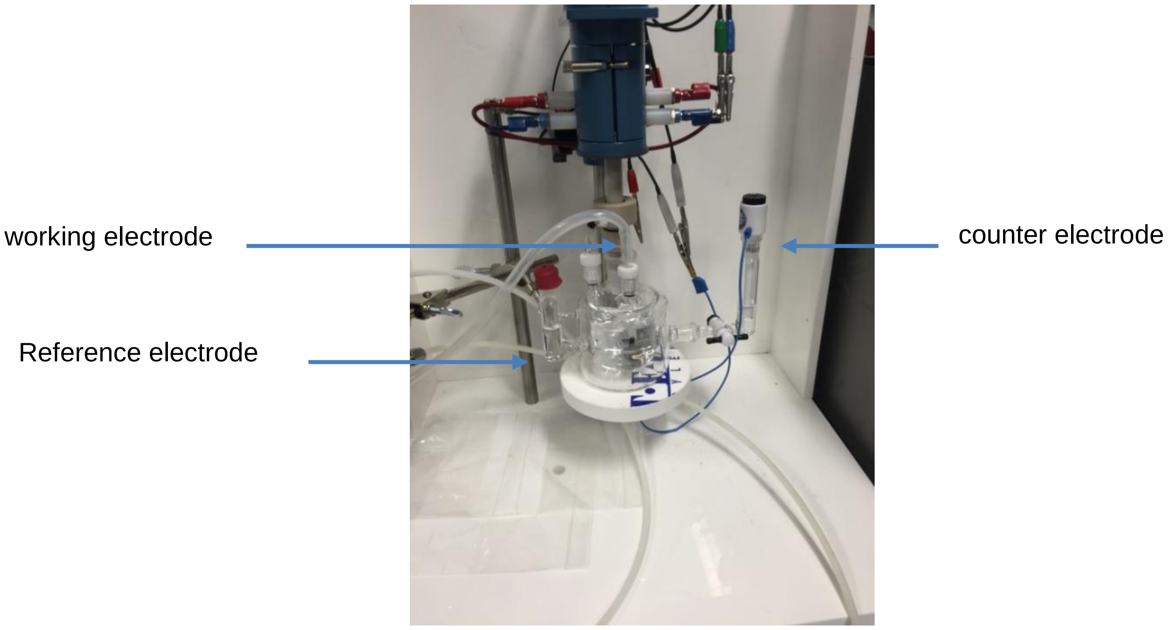

Figure 14: The electrochemical cell set up

3.8.2 Supercapacitors tests

The electrode capacitance in a chosen electrolyte can be measured by using CV, which records the cyclic voltammograms of the material. If the total charge Q accumulated in the electrode layer, expressed in Equation 12 (Wang et al., 2012), is measured using the area integrated under the CV diagram in either direction of a potential window from $E1$ to $E2$, the capacitance C can be obtained by the following equation:

Equation 12

$$C = \left| \frac{Q}{E2 - E1} \right|$$

Another method of obtaining the capacitance is by cyclic charge–discharge curves in two- and three-electrode systems. Setting the current density and potential window for the cycle, and knowing the mass of the electrode materials coated on the current collector, the capacitance can be calculated by

Equation 13 (Wang et al., 2012)

$$C = \frac{I}{W} \times \frac{\Delta t}{V}$$

where I is the current in amperes, W is the mass of electrode material (g), $\frac{I}{W}$ is the current density set by the user of the potentiostat, Δt is the time needed for the discharge cycle and V is the working potential window.

The electrochemical behaviour of the MOF-derived carbons was characterised by measuring the specific capacity using VC and a galvanostatic charge–discharge curve, at different sweep rates and current densities respectively, in a three-electrode system. The reference electrode used in this study was Ag/AgCl, and the counter electrode was a Pt-wired electrode in all tests. Before coating the electrodes, they needed to be cleaned. Hence, the Ni foam electrodes were first soaked in EtOH and sonicated for 15 min, then soaked in DI water and sonicated for another 15 min. Thereafter, they were dried overnight in the oven at 60 °C. After the electrodes had dried, they were labelled with a marker and weighed. Then, they were coated with the ink solution (1 cm^2 of the electrode area) and dried overnight under vacuum at 80 °C.

3.8.2.1 Carbonised ZIF-8

H_2SO_4 was used as the electrolyte. In order to make the slurry, 0.085 g of C_{ZIF-8} was mixed with 0.005 g C-65 as the booster carbon and 0.001 g polyvinylidene fluoride (PVDF) as the binder. A small amount of the N-Methyl-2-pyrrolidone (NMP) was added to make the ink.

1 cm^2 of the Ni-foam paper and carbon paper was coated with the slurry and dried overnight under full vacuum at 85 °C. Thereafter, the Ni-foams were pressed under 12 MPa to make the ink adhere completely to the electrode. The weight of the loaded carbon was calculated using the difference of the dried carbon coated electrodes and clean electrodes multiplied by 85%.

3.8.2.1.1 Cyclic voltammetry

The CV test at different sweep rates was performed at the potential window of 0–0.8 V. The mass loading for this test on the carbon paper was 0.00035 g and 0.01126 g on the Ni-foam. Since the mass loading on the Ni-foam was higher than required, only the carbon paper was used to evaluate the specific capacitance of the carbonised ZIF-8. The specific capacitance of the carbonised ZIF-8 at different potential windows was calculated based on Equation 12.

3.8.2.1.2 Charge–discharge curve for CZIF-8

Electrochemical measurements in the three-electrode systems were done in 6 M KOH electrolyte solution using a Pt mesh and silver/silver chloride (Ag/AgCl) as the counter and reference electrodes, respectively. The pH of the reference electrode was buffered by an Orion Electrode Filling Solution. The working electrodes were prepared as follows: 80% activated carbon (CC-Fe, CC-KOH, KB or graphite) was mixed with 10% Super C65 and 10% PVDF wherein NMP solution was added drop by drop to reach a good consistency. The mixture was then manually ground and mixed using a mortar and pestle, and then poured in the ball miller jars with the zirconia balls and mixed for 3 h at 300 rpm in both directions in the ball mill (pulverisette, FRITSCH, Markt Einersheim, Germany). The mixture was then drop-cased on the nickel foam using a spatula, reaching a final mass of 1–10 mg activated carbon after drying the electrode/current collector system. The samples were then pressed at a pressure of 10 tons for 20 s to fold the electrode-coated area and have a final physical surface area of 1 cm^2. Galvanostatic cyclic charge–discharge was performed at current density of 0.1 A g^{-1}. The specific capacitances were calculated from the Cyclic Charge-Discahreg (CCD) curves and are given in Chapter 5.

3.8.2.2 CMOF-5

0.0805 g CMOF-5 was mixed and ground with 0.0102 g Ketjen black, 0.0116 g Polytetrafluoroethylene (PTFE) as a binder and 8 mL ETOH. After all the reactants were ground, they were applied to the carbon paper and dried overnight at 100 °C. After cooling to room temperature, the samples were immersed in 6 M KOH for 6 h prior to the analysis.

3.8.2.2.1 Cyclic voltammetry

Cyclic voltammetry was carried out at the scan rates of 1, 2, 5, 10, 20, 50, 100 and 200 mV s^{-1}, in the potential window of 0–0.8 V. The results are provided in Chapter 5

3.8.2.2.2 Cyclic charge–discharge

The galvanostatic charge–discharge was carried out at the 0.25 A g^{-1}. The results are given in Chapter 4.

3.8.2.3 CMIL-100(Fe)

0.0808 g C-MIL-100(Fe), 0.0108 g C-65, 0.0108 g PTFE and 8 mL ETOH were mixed and ground using a mortar and pestle until a homogenous paste was yielded. The paste was then drop-cased on the carbon paper and dried at 100 °C overnight. Then, the electrodes were immersed in 6 M KOH electrolyte before the test was run.

3.8.2.3.1 Cyclic voltammetry

The cyclic voltammograms was carried out at 1, 2, 5,10,20,50,100 and 200 mV s^{-1}. The results are given in Chapter 5.

3.8.2.3.2 Charge–discharge

The galvanostatic charge–discharge test was carried out at 0.01, 0.1, 0.2 and 0.25 A $g^{-1.}$ The specific capacitance was calculated from CCD and is provided in Chapter 5.

Chapter 4

4 Structural Characterisation Results

4.1 Powder X-Ray Diffraction Results

The crystallinity of the synthesised MOFs structures was characterised with PXRD and confirmed with the experimental data simulated by Material Studio version 8.0.0.843, licenced by University College London.

4.1.1 Powder X-ray diffraction results for Ni-MOF-74

Figure 15 illustrates the PXRD patterns for MOF-74. We see that the PXRD pattern for our synthesised MOF-74 matches the simulated PXRD, which shows the purity of materials, as expected.

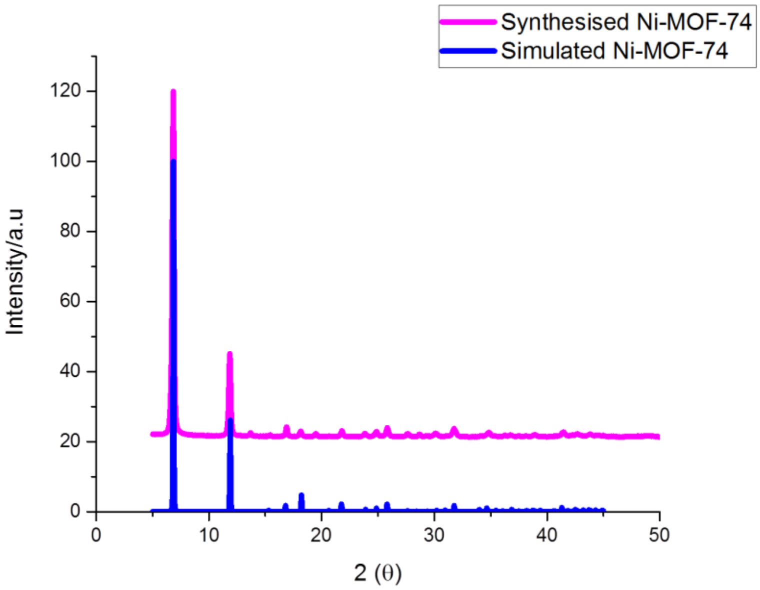

Figure 15: PXRD pattern for Ni-MOF-74

4.1.2 Powder X-ray diffraction results for ZIF-8

The PXRD pattern for ZIF-8 is shown in Figure 16. As is expected, the PXRD pattern for the synthesised ZIF-8 is perfectly matched with the simulated one, which shows the crystalline structure of the synthesised ZIF-8

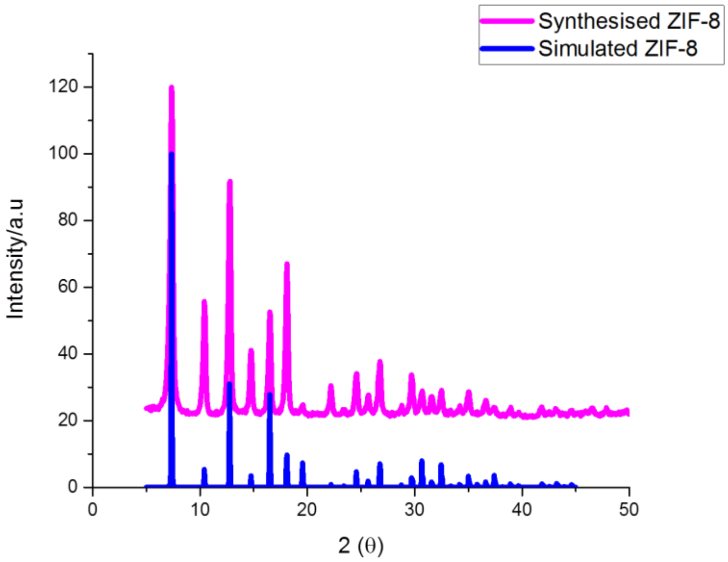

Figure 16: PXRD pattern for ZIF-8

4.1.1 Powder X-ray diffraction results for MIL-100(Al)

The PXRD pattern of MIL-100 is provided in Figure 17. As seen, it is similar to the simulated pattern; however, there are some noises in the synthesised PXRD which can be the result of some unreacted linkers in the pores of the MOF. Since the synthesis of MIL-100(Al) was not successful, we decided to synthesis MIL-100(Fe) instead. However, we believe that with further activation, it is possible to have MIL-100(Al) with a more crystalline structure.

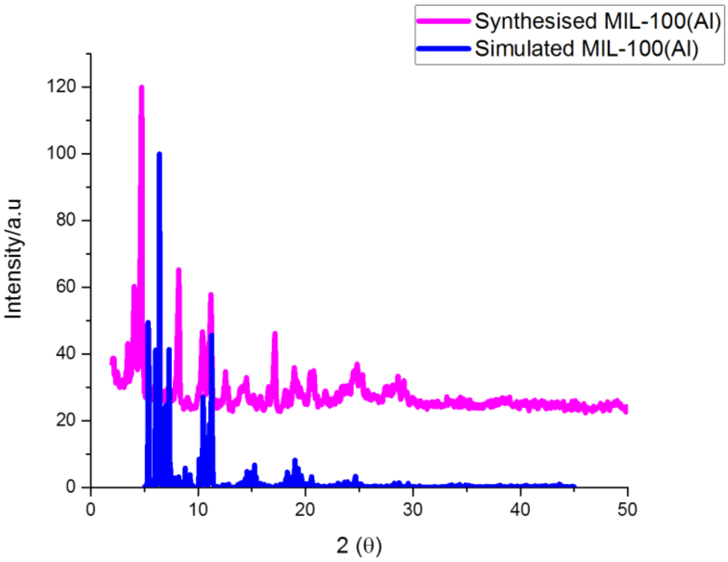

Figure 17: PXRD Pattern for MIL-100(Al)

4.1.2 Powder X-ray diffraction results for MIL-100(Fe)

The PXRD pattern for MIL-100(Fe) was compared with the simulated pattern and given in Figure 18. As is shown, the XRD pattern matches perfectly with the simulated pattern, demonstrating the crystallinity of the sample.

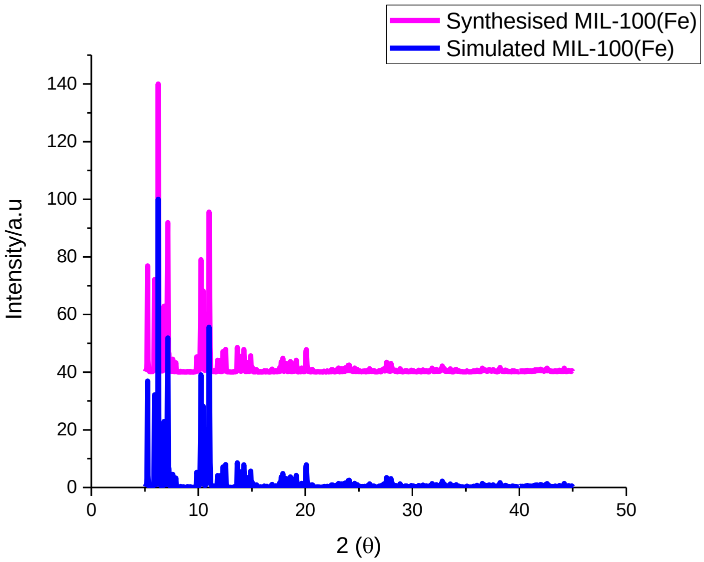

Figure 18: PXRD pattern for MIL-100(Fe)

4.1.3 Powder X-ray diffraction results for UiO-66

The structure crystallinity of the synthesised UiO-66 was characterised with PXRD and compared with the simulated pattern. As is shown in Figure 19, the XRD pattern for the synthesised sample perfectly matches with the simulated pattern, confirming the phase purity and crystalline structure of the synthesised sample.

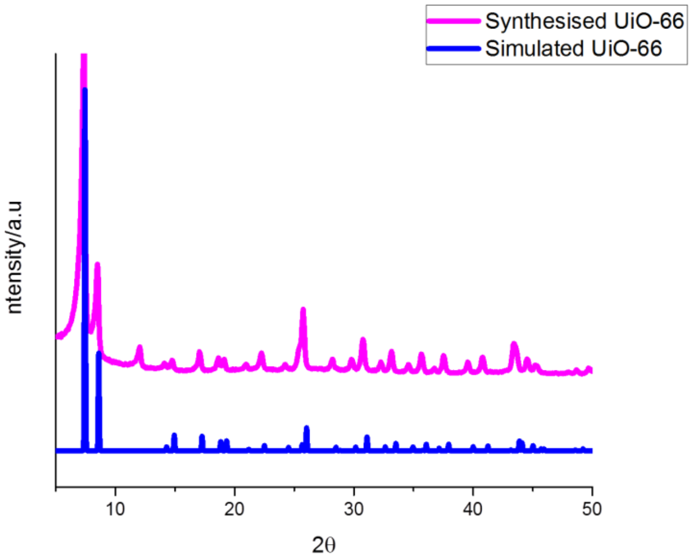

Figure 19: PXRD pattern for UiO-66

4.1.4 Powder X-ray diffraction results for UiO-67

The synthesised sample was characterised with PXRD to check the crystallinity of the sample. Figure 20 shows the comparison of the PXRD pattern for the synthesised sample and the simulated pattern, which matches perfectly. This result confirms the crystallinity of the MOF structure, and hence verifies the successful synthesis of the sample.

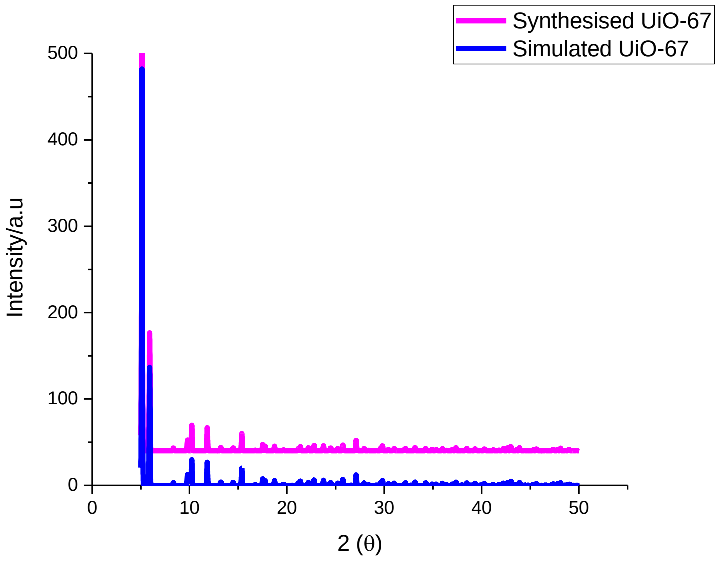

Figure 20: PXRD pattern for UiO-67

4.1.5 Powder X-ray diffraction results for MIL-53

The PXRD pattern of the synthesised MIL-53 was in agreement with the simulated pattern, showing the phase purity of the synthesised sample (see Figure 21).

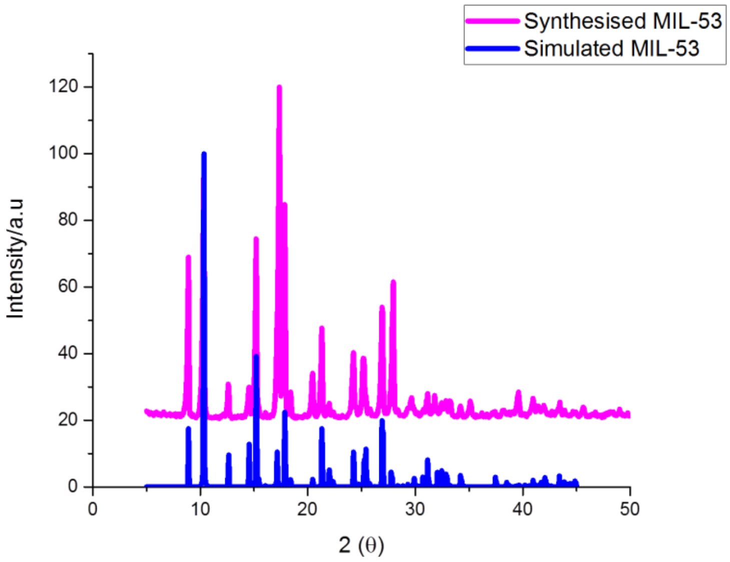

Figure 21: PXRD Pattern for MIL-53(Al)

4.1.6 Powder X-ray diffraction results for MOF-5

The successful synthesis of the MOF-5 was confirmed by comparing the PXRD patterns of the synthesised sample with the simulated pattern. Figure 22 shows the

PXRD pattern of the synthesised MOF-5 plotted over the simulated sample, matching perfectly, thus confirming the phase purity of the sample.

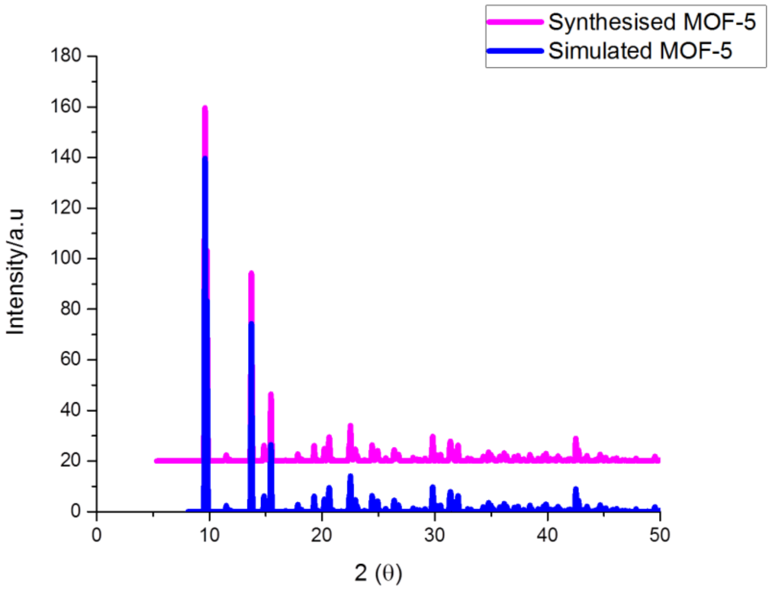

Figure 22: PXRD pattern for MOF-5

4.1.7 Conclusion

The crystallinity structures of the synthesised samples have been determined by plotting the PXRD patterns of the synthesised MOFs versus the simulated ones. The comparison of the results shows that all the MOFs synthesised have crystalline structure and pure phase, except for MIL-100(Al), which may be a result of not being activated properly. Better washing and solvent exchange process is recommended to overcome this problem .

4.2 Brunauer-Emmet-Teller Results for Synthesised Metal Organic Frameworks

The BET surface area of the synthesised MOFs was calculated using the BET equation described in Chapter 2. The pore size of the synthesised MOFs was measured using the density functional theory (DFT) theory method by using desorption isotherms.

4.2.1 Brunauer-Emmet-Teller results for Ni-MOF-74

Figure 23 illustrates type I nitrogen adsorption-desorption isotherm of the MOF-74, which indicates the microporosity of the material. The pore size distribution of Ni-MOF-74 was plotted using desorption isotherm with the DFT theory based on the slit-shaped carbon model (using the SAIEUAS software provided by Micromeritics). The result is given in Figure 24. The BET surface area and pore volume of the Ni-MOF-74 are given in Table 7.

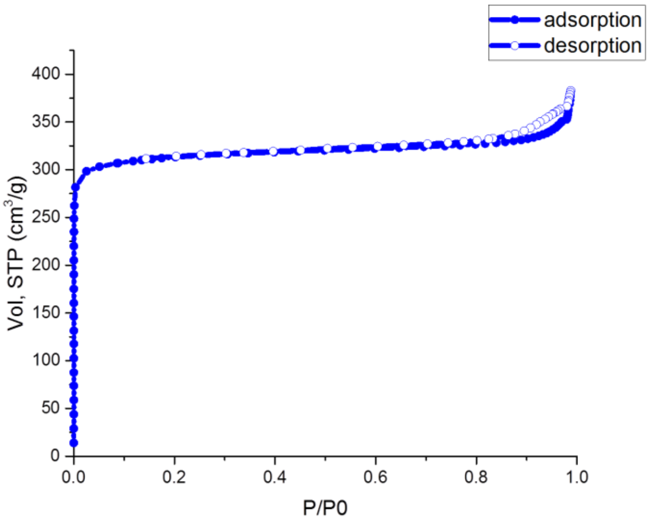

Figure 23: Nitrogen sorption isotherm for Ni-MOF-74

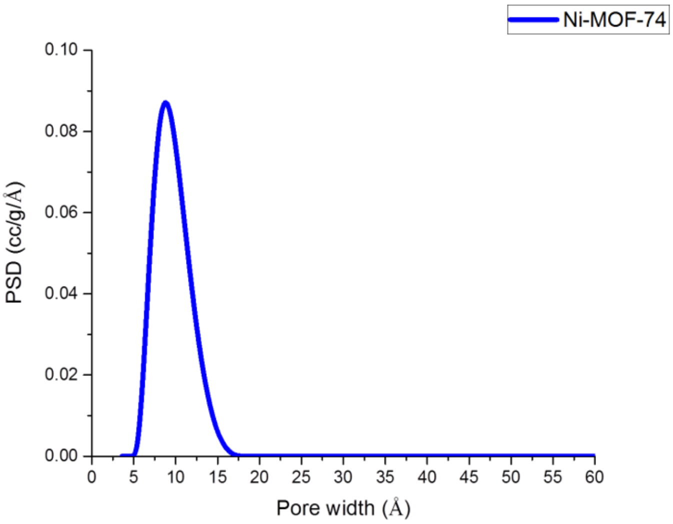

Figure 24: Pore size distribution of Ni-MOF-74

Table 7: BET surface area and pore volume

Sample	BET surface area (m^2/g)	Pore volume (cm^3/g)
Ni-MOF-74	1135	0.56

4.2.2 Brunauer-Emmet-Teller results for ZIF-8

Figure 25 illustrates type I isotherm for ZIF-8 as expected, indicating the microporosity of the synthesised sample. The calculated BET surface area and pore volume are given in **Error! Reference source not found.**. The pore size distribution of ZIF-8 was p lotted using DFT model based on the slit-shaped carbon model, using the adsorption isotherm as shown in Figure *26*.

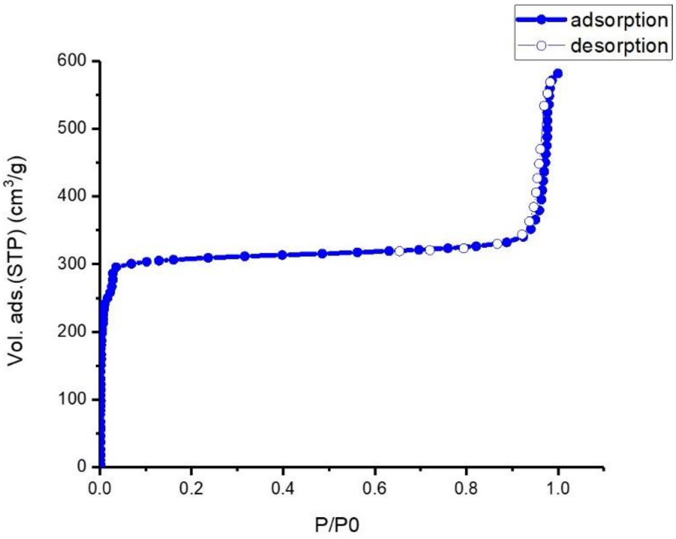

Figure 25: Nitrogen sorption isotherm for ZIF-8

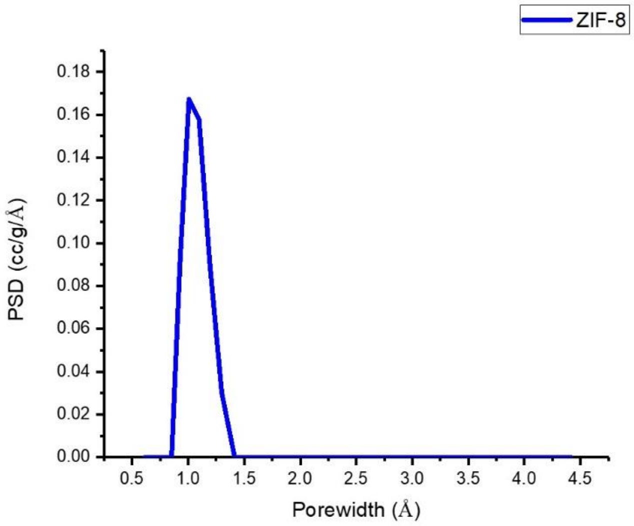

Figure 26: Pore size distribution of ZIF-8

Table 8: BET surface area and pore volume

Sample	BET surface area (m^2/g)	Pore volume(cm^3/g)
ZIF-8	1200	0.55

4.2.3 Brunauer-Emmet-Teller results for MIL-100 (Al)

Figure 27 shows the type I nitrogen adsorption–desorption isotherm for MIL-100(Al), starting with a concave shape towards P/P_0, where the adsorption of micropores occurs, then n reaches a plateau, and finally equilibrium is reached at the relative pressure of 1.The BET surface area and pore volume of the sample are given in Table *9*. The BET surface area was calculated using the BET equation.

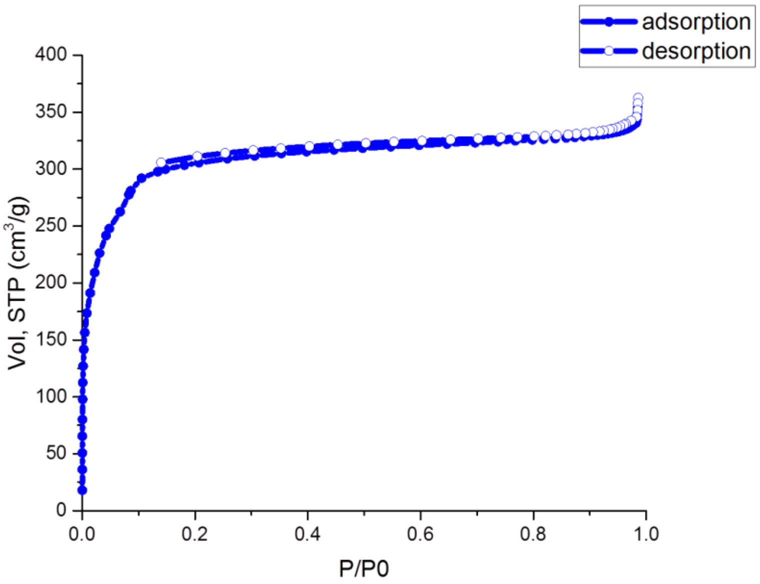

Figure 27: Nitrogen sorption isotherm for MIL-100(Al)

Table 9: BET surface area and pore volume of MIL-100(Al)

Sample	**BET surface area** **(m^2/g)**	**Pore volume** **(cm^3/g)**
MIL-100(Al)	1099	0.54

4.2.4 Brunauer-Emmet-Teller results for MIL-100(Fe)

Figure 28 shows the type I nitrogen adsorption–desorption isotherm for MIL-100(Fe). It begins with a concave shape towards P/P_0, where the adsorption of micropores occurs, then reaches a plateau, and attains equilibrium at the relative pressure of 1. Using desorption isotherm, the pore size distribution of the MIL-100(Fe) was calculated and is plotted in Figure 29.

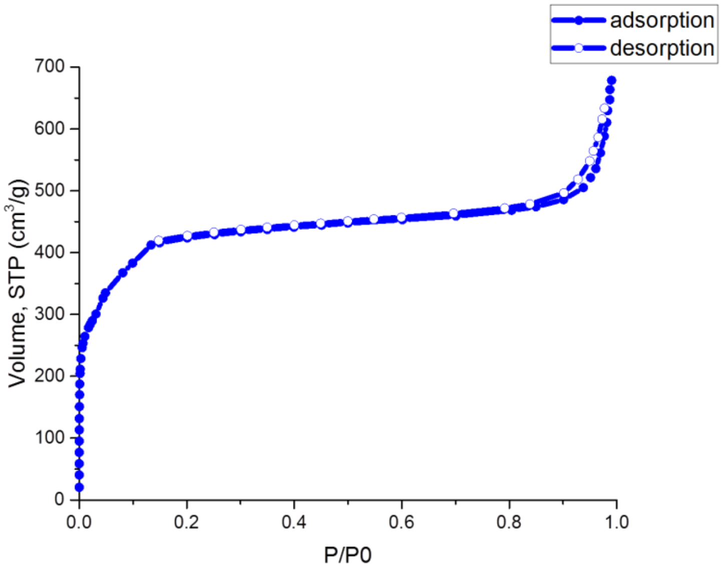

Figure 28: Nitrogen sorption isotherm for MIL-100(Fe)

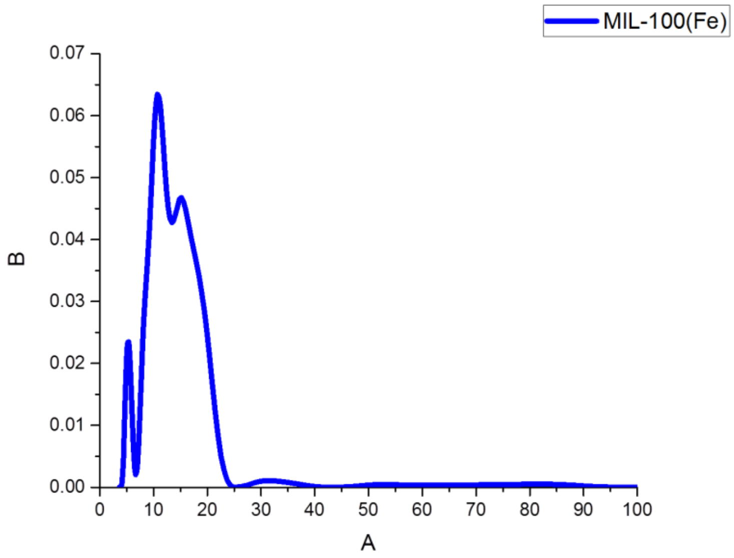

Figure 29: Pore size distribution o fMIL-100(Fe)

The BET surface area and pore volume of the MIL-100(Fe) are given in Table 10.

Table 10: BET surface area and pore volume of MIL-100(Fe)

Sample	**BET surface area** (m^2/g)	**Pore volume** (cm^3/g)
MIL-100(Fe)	1645	0.82

4.2.5 Brunauer-Emmet-Teller results for MOF-5

Figure 30 shows the type I nitrogen adsorption–desorption isotherm for MOF-5. It begins with a concave shape towards P/P_0, where the adsorption of micropores occurs, then reaches a plateau, and a hysteresis loop indicates the presence of the mesopores in the structure of this MOF. As it is shown on Figure 31, two pore sizes are observed at the range of 8 and 15 Å for this MOF. The BET surface area and pore volume of the MOF-5 are given in Table 11.

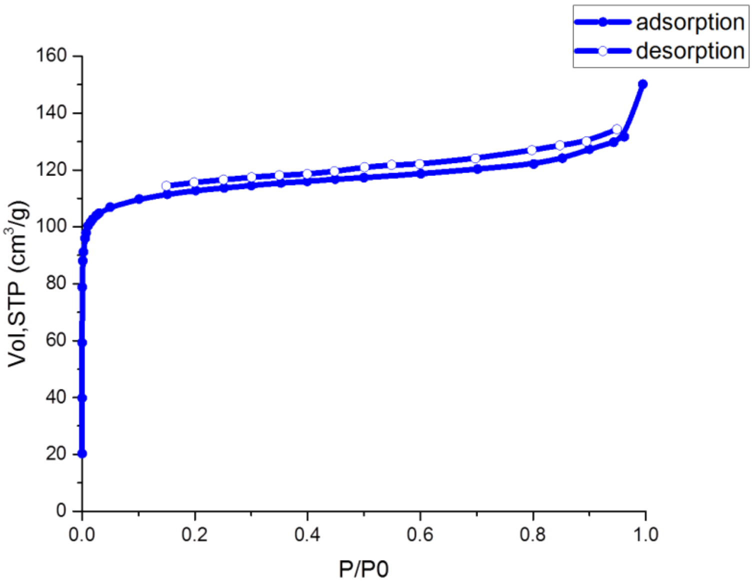

Figure 30: Nitrogen sorption isotherm for MOF-5

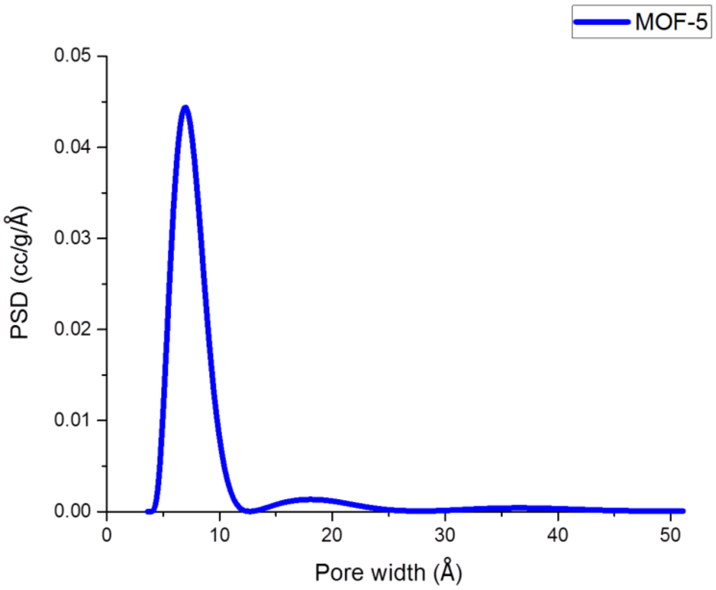

Figure 31: Pore size distribution for MOF-5

Table 11: BET surface area and pore volume of MOF-5

Sample	**BET surface area (m²/g)**	**Pore volume (cm³/g)**
MOF-5	600	0.96

4.2.6 Brunauer-Emmet-Teller results for HKUST-1

Commercial HKUST was purchased from Sigma-Aldrich and degassed overnight under vacuum at 100 °C before beginning the adsorption measurements. The nitrogen sorption isotherm and pore size distribution of the commercial HKUST are given in Figure 32 and Figure 33 respectively. The adsorption–desorption isotherm given in Figure 33 shows type IV isotherm with a hysteresis loop at a higher pressure. The hysteresis loop appears when there are mesopores available in the structure of the sample and is associated with the capillary condensation of the adsorbing and desorbing of the mesopores. The BET surface area and pore volume of the HKUST are given in Table 12.

As seen in Figure *33*, there are two pore sizes of 5 and 9 Å, similar to the theoretical pore sizes found in HKUST-1. The BET surface area and pore volume of the commercial HKUST are provided in Table 12.

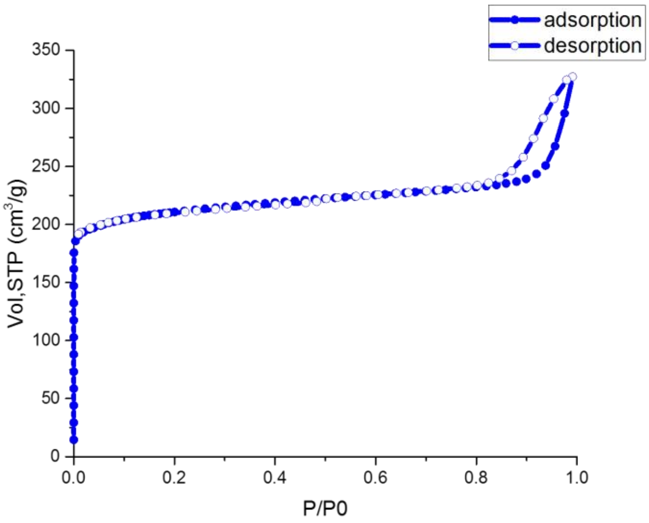

Figure 32: Nitrogen sorption isotherm for commercial HKUST

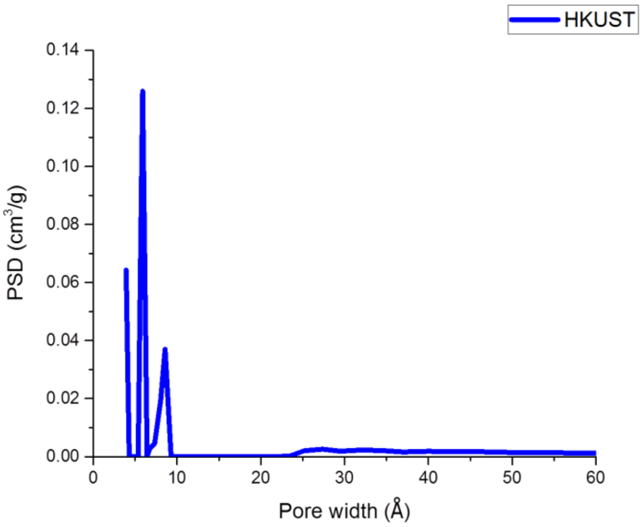

Figure 33: Pore size distribution for HKUST

Table 12:BET surface area and pore volume for HKUST

Sample	**BET surface area (m^2/g)**	**Pore volume (cm^3/g)**
HKUST	825	0.50

4.2.7 Brunauer-Emmet-Teller results for MIL-53(Al)

The nitrogen sorption isotherm for MIL-53(Al) is given in Figure 34. The isotherm is a type I isotherm as expected, but has a very low surface area and pore volume. As the PXRD result for MIL-53 was perfectly matched, the low surface area can a result of not being activated properly, requiring further activation. Then BET surface area and pore volume of the synthesised MIL-53 are given in Table 13.

Table 13: MIL-53(Al) BET surface area and pore volume

Sample	**BET surface area (m^2/g)**	**Pore volume (cm^3/g)**
MIL-53(Al)	274.0671	0.132130

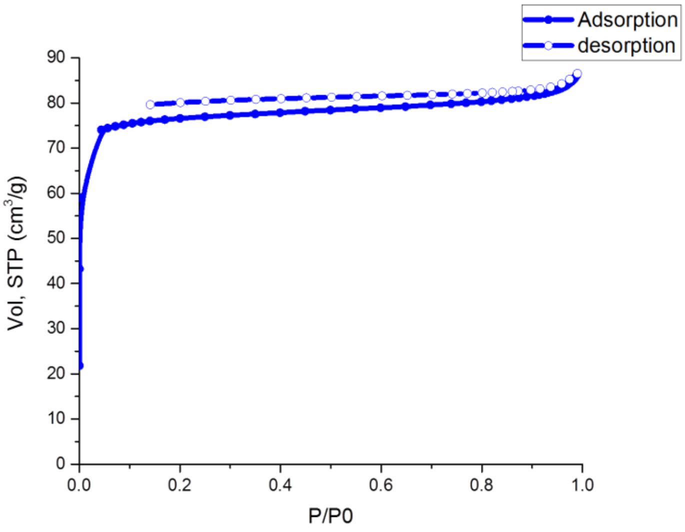

Figure 34: Nitrogen sorption isotherm for MIIL-53(Al)

4.2.8 Brunauer-Emmet-Teller results for UiO-66

The synthesised UiO-66 was degassed overnight at 110 °C under vacuum prior to the nitrogen adsorption–desorption measurements being taken. Figure 35 shows the adsorption–desorption isotherm of the UiO-66 under N_2 at 77 K. This isotherm is a type I isotherm, which has a sharp rise at low relative pressure. The isotherm has a flat plateau at the range of 0.1–1, and reaches equilibrium at the relative pressure of 1. The pore size distribution of the UiO-66 was plotted using the DFT model based on the slit-shaped carbon and the adsorption isotherm. See Figure *36*. The calculated BET surface area and pore volume of the UiO-66 is given in Table 14.

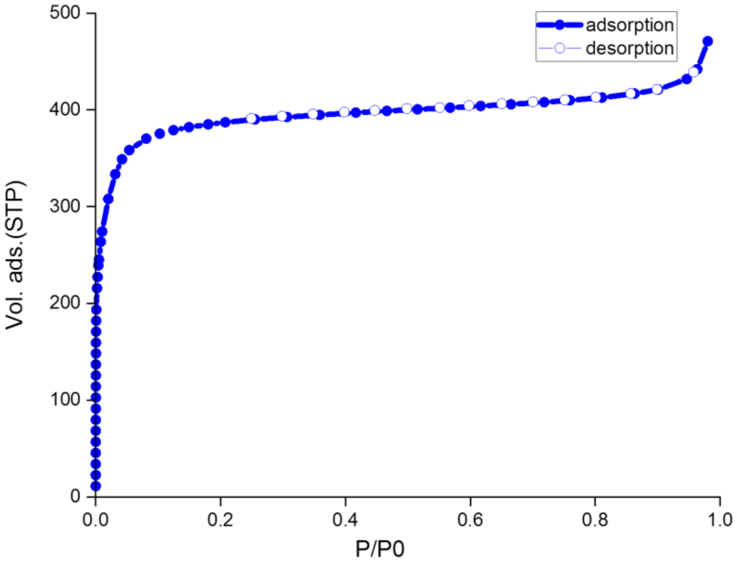

Figure 35: Nitrogen sorption isotherm for UiO-66

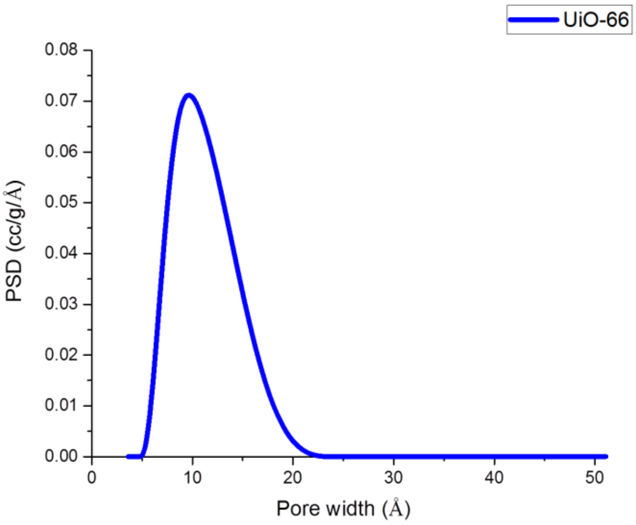

Figure 36: Pore size distribution of UiO-66

Table 14: UiO-66 BET surface area and pore volume

Sample	BET surface area (m^2/g)	Pore volume (cm^3/g)
UiO-66	1476	0.65

4.2.9 Brunauer-Emmet-Teller results for UiO-67

Prior to the measurements, the sample was degassed overnight at 110 °C under vacuum. The nitrogen sorption isotherm and pore size distribution for UiO-67 are given in Figure 37 and Figure 38 respectively. Figure 37 shows a type I isotherms with a step at the relative pressure at 0.1; it is believed that this step is due to the presence of two types of pores (octahedral (11.5 Å) and tetrahedral (21.5 Å))(Katz et al., 2013). The BET surface area and pore volume of UiO-67 are given in Table 15.

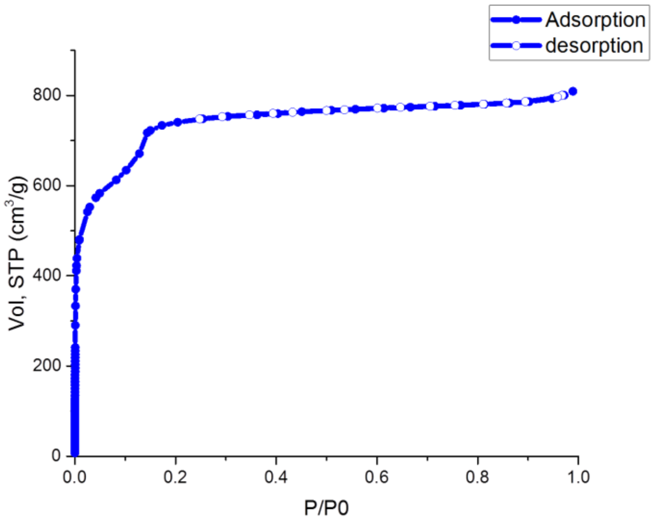

Figure 37: Nitrogen sorption isotherm for UiO-67

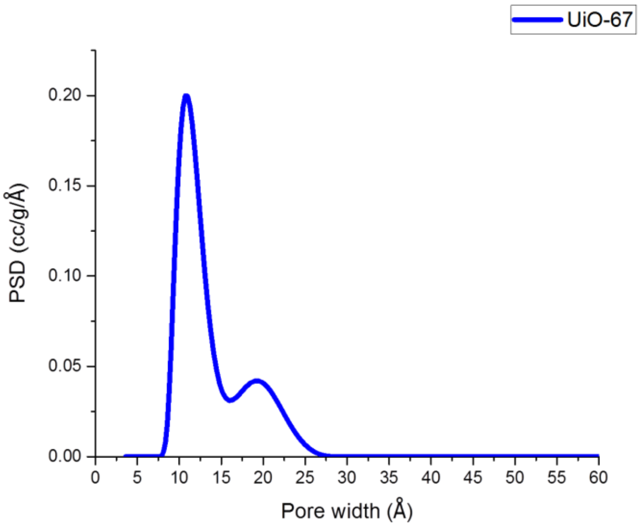

Figure 38: Pore size distribution for UiO-67

Table 15: UiO-67 BET surface area and pore volume

Sample	BET surface area (m^2/g)	Pore volume (cm^3/g)
UiO-67	2500	1.21

4.2.10 Brunauer-Emmet-Teller results for C-ZIF-8

As was expected, type I isotherm is without any hysteresis loop (see Figure *39*) and there was an increase in the surface area, from 1200 to 1645 m^2/g. The pore size distribution of the C-ZIF-8 was plotted using DFT model based on slit-shaped carbon, and is presented in Figure 40. As shown, C-ZIF-8 has both micro- and mesopores, I at 11 Å and 35 Å. The calculated BET surface area and pore volume are given in Table 16.

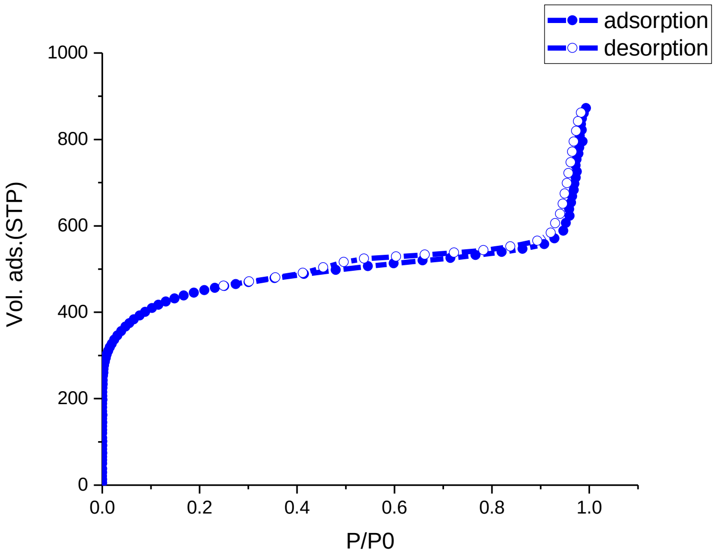

Figure 39: Nitrogen sorption isotherm for C-ZIF-8

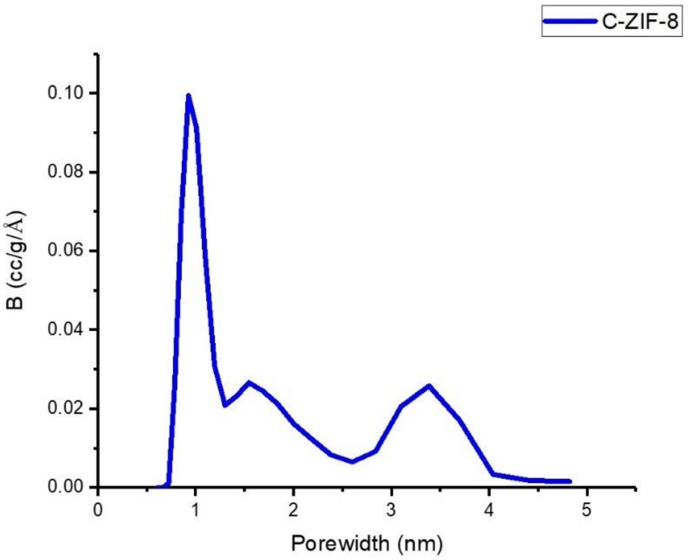

Figure 40: Pore size distribution for C-ZIF-8

Table 16: BET surface area and pore volume of C-ZIF-8

Sample	**BET surface area (m^2/g)**	**Pore volume(cm^3/g)**
C-ZIF-8	1645	0.33

4.2.11 Brunauer-Emmet-Teller results for C-MOF-5

Figure 41 shows a type IV isotherm with a concave shape towards P/P_0 at the beginning of the isotherm, at which the micropores filling occurs. It then has a linear isotherm where equilibrium is reached, and in the final region has a convex shape with a hysteresis loop, which corresponds to the pore filling and emptying of the mesopores. Figure 42 shows the pore size distribution of the C-MOF-5 having pores at 8 and 31 Å corresponding to micro and mesoporosity of the sample, respectively. The calculated BET surface area and pore volume of the C-MOF-5 are given in Table 17.

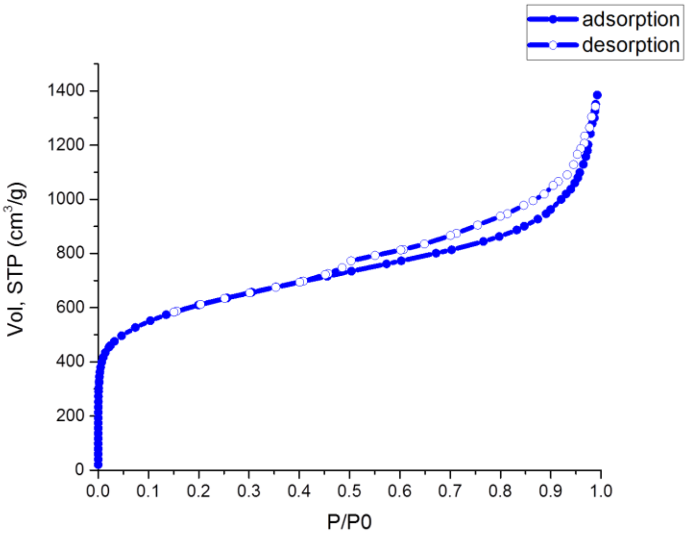

Figure 41: Nitorgen sorption isotherms for C-MOF-5

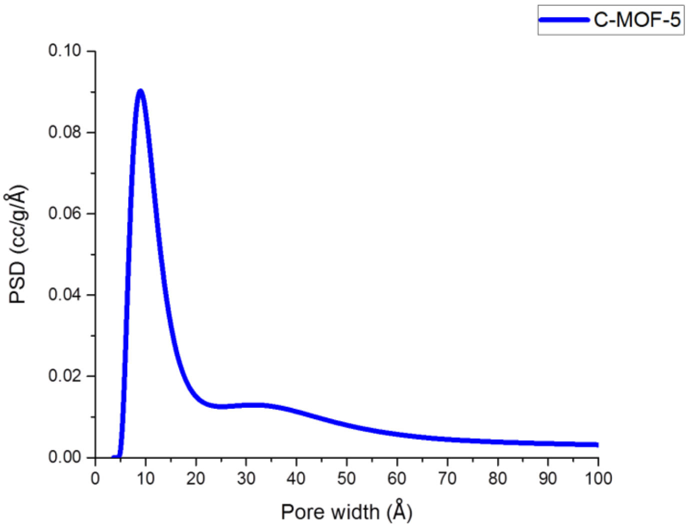

Figure 42: Pore size distribution for C-MOF-5

Table 17: BET surface area and pore volume of C-MOF-5

Sample	BET surface area (m^2/g)	Pore volume (cm^3/g)
C-MOF-5	2208	0.95

4.2.12 Brunauer-Emmet-Teller results for C-MIL-100(Fe)

The sample was degassed overnight at 110 °C under vacuum. Figure 43 shows a type IV isotherm. The isotherm starts with the micropore filling at the low relative pressure and a concave shape towards the P/P0. Then, there is a plateau region, and in the final region there is small hysteresis loop, which indicates the presence of the mesopores in the structure of the carbonised MIL-100(Fe). Figure 44 shows the pore size distribution of the C-MIL-100(Fe) calculated from adsorption isotherm applying the DFT model using SAIEUS software provided by the Micromeritics Corporation. The pore size distribution indicates the presence of both micro- and mesopores in the structure of the carbonised MOF. This carbon has pore sizes at 5, 11 and 21 Å. The BET surface area and pore volume of the C-MIL-100(Fe) are given in Table 18. The very low surface area of the carbonised MOF can be explained as the result of a change in the surface of the sample after washing with HCl. It is also possible that the structure of the MOF collapsed during the carbonisation process. The BET surface area and pore volume of the C-MIL-100(Fe) are given in Table 18.

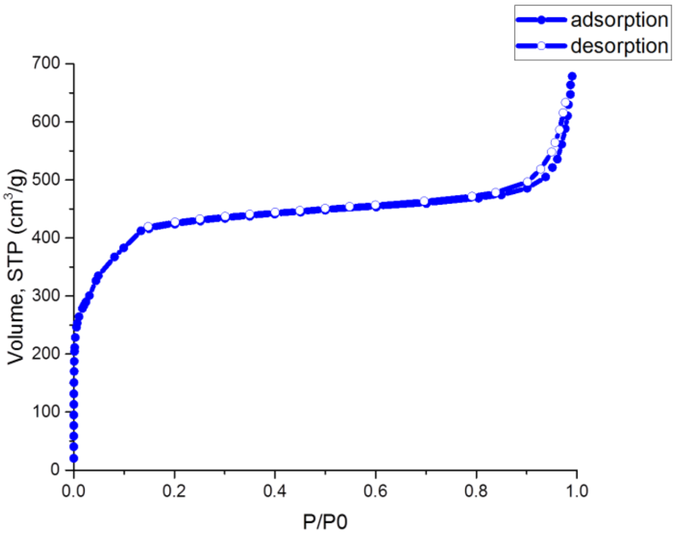

Figure 43: Nitrogen sorption isotherm for C-MIL-100(Fe)

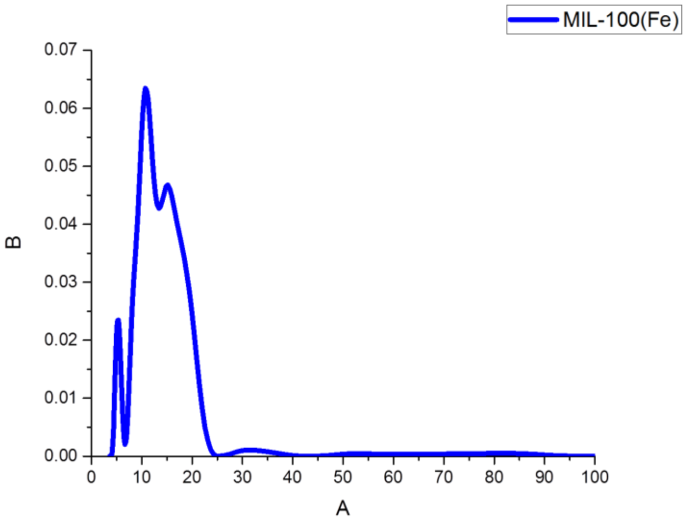

Figure 44: Pore size distribution for C-MIL-100(Fe)

Table 18: BET surface area and pore volume for C-MIL-100(Fe)

Sample	BET surface area (m^2/g)	Pore volume (cm^3/g)
C-MIL-100(Fe)	105.44	0.25

4.3 Conclusion

The surface area and porosity of all synthesised and carbonised MOFs have been characterised under nitrogen at 77 using the BET equation and DFT model, respectively. The results from the measurements illustrate that the carbonised samples have a similar pore structure to the MOF precursor, as expected. Also, an increase in the surface area of the carbonised samples has been observed, except in the case of MIL-100(Fe), which we believe is due to the washing process with HCl; the surface chemistry of the template has been changed and some of the pores have been blocked.

4.4 Elemental Analysis

The morphology structure of the carbonised samples and Pt loaded C-ZIF-8 was evaluated by SEM coupled with energy dispersive X-ray spectroscopy.

4.4.1 Scanning electron microscopy image of C-ZIF-8

Figure 45 shows the morphology structure of the carbonised ZIF-8. It is observable that this carbon has the similar structure to the ZIF-8.

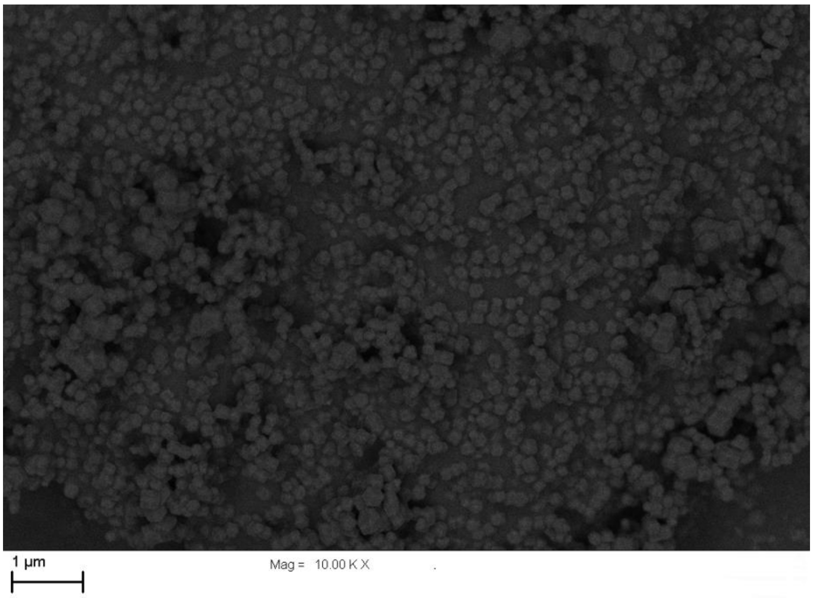

Figure 45: SEM image of the C-ZIF-8

4.4.2 Scanning electron microscopy image of C-MOF-5

The morphology structure of the carbonised MOF-5 was evaluated with SEM. Figure 46 shows the morphology structure of the C-MOF-5.

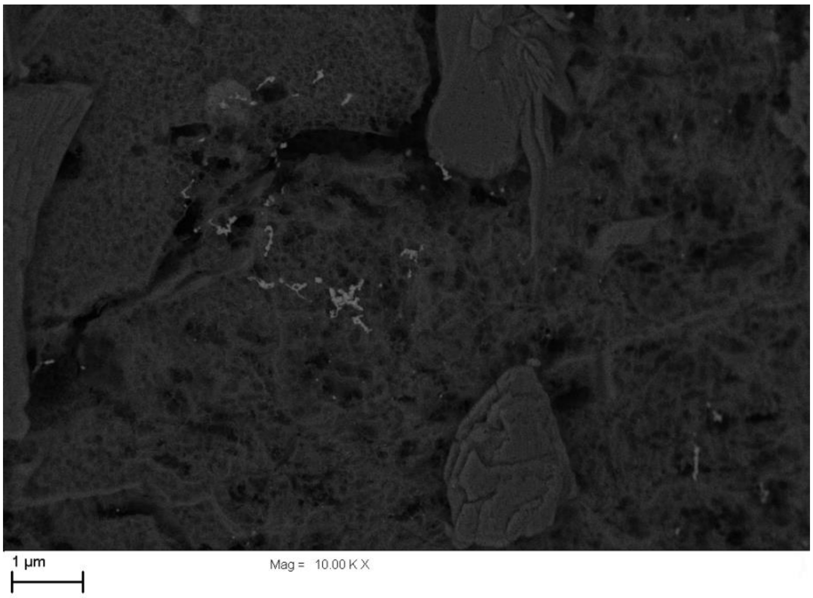

Figure 46: SEM image of the C-MOF-5

4.4.3 Scanning electron microscopy image of C-MIL-100(Fe)

Figure 47 shows SEM image of the carbonised MIL-100(Fe). As shown, there are some light points showing the presence of the traces of Fe in the structure of the carbon, left over from the MOF precursor. This image shows that the washing process was not thorough enough.

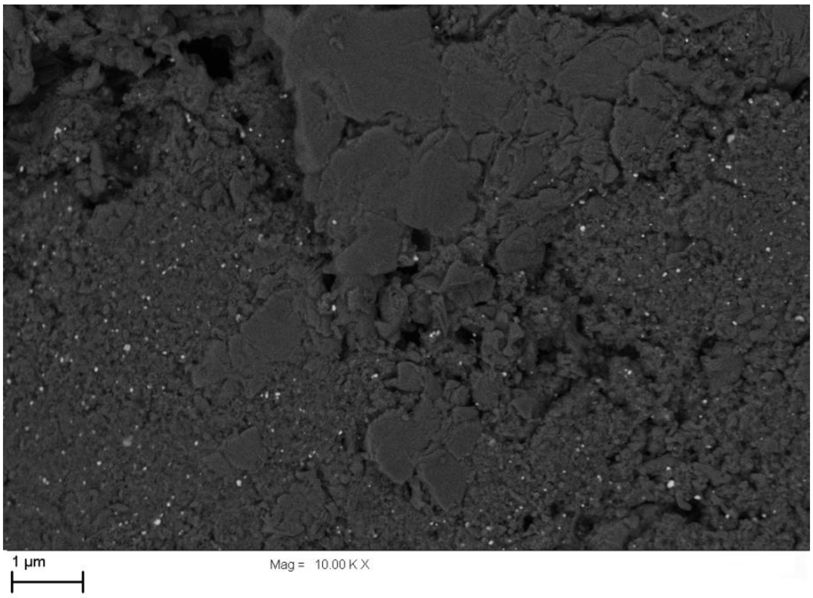

Figure 47: SEM image of C-MIL-100(Fe)

4.4.4 Scanning electron microscopy images of Pt/$\text{C}_{\text{ZIF-8}}$

The SEM image of Pt loaded carbons is presented in Figure 48.

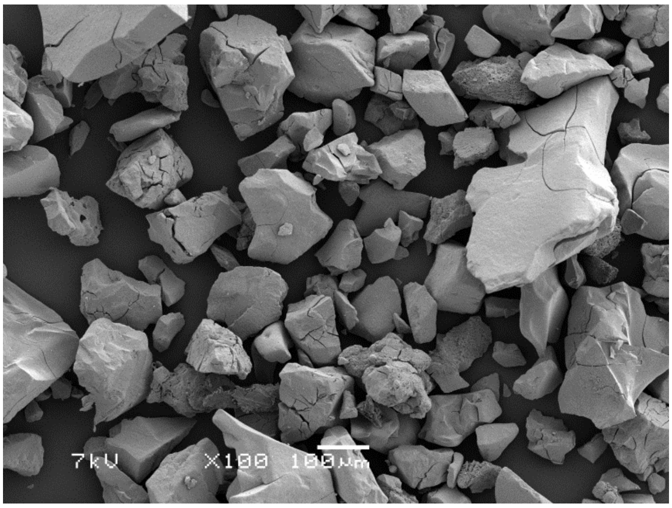

Figure 48: SEM images of Pt/CZIF-8

4.5 Energy Dispersive Spectroscopy Result for $\text{C}_{\text{ZIF-8}}$

The $\text{C}_{\text{ZIF-8}}$ was analysed by EDS and the results are given in Figure 49.

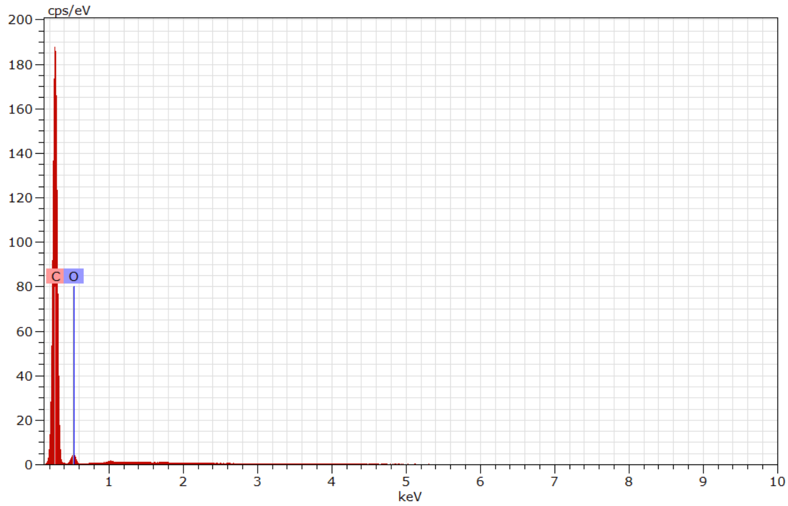

Figure 49: a) SEM image of $\text{C}_{\text{ZIF-8}}$, b) and c) EDS analysis of $\text{C}_{\text{ZIF-8}}$

4.5.1 EDS analysis of Pt/$\text{C}_{\text{ZIF-8}}$

The elemental analysis for the Pt loaded on carbonised ZIF-8 is given in Figure 50 and Table 19. The Pt loaded was not as high as expected, and there were some impurities in the sample. The source of the Zn in the sample can be as a result of unsuccessful carbonisation. The presence of oxygen can be as a result of leak in the furnace during the carbonisation. This problem can be fixed with purging nitrogen with higher flow rate.

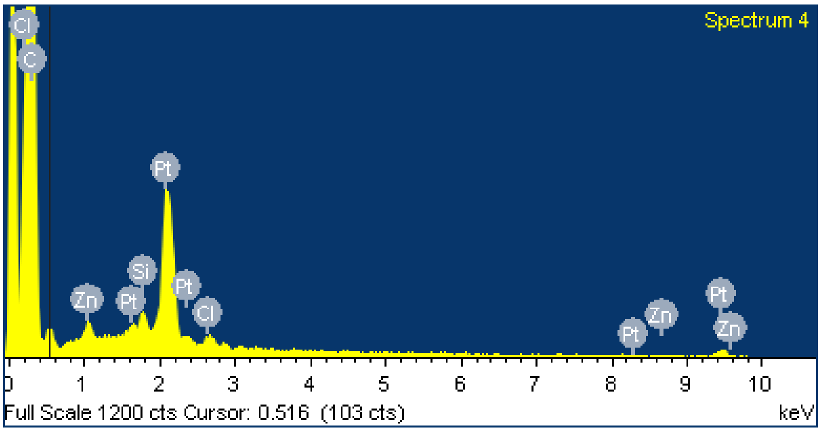

Figure 50: EDS analysis of Pt/C-ZIF-8

Table 19: Elemental analysis for Pt/C-ZIF-8

Element	Weight%	Atomic%
C K	80.04	97.81
Si K	0.77	0.40
Cl K	0.62	0.26
Zn K	0.89	0.20
Pt M	17.69	1.33
Total	100.00	100.00

4.5.2 Energy dispersive spectroscopy result for Pt/Vulcan

Figure *51* and Table 20 show elemental analysis data for the Pt loaded on Vulcan. As it is shown in Table 20, the amount of Pt loaded was 20%, as expected.

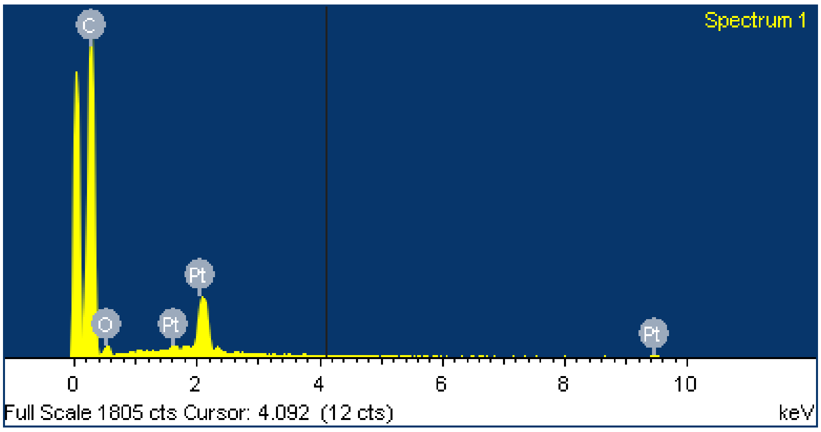

Figure 51: EDS analysis data for Pt/Vulcan

Table 20: Elemental analysis data for Pt/Vulcan

Element	Weight%	Atomic%
C K	73.18	92.13
O K	6.67	6.31
Pt M	20.15	1.56
Totals	100.00	100.00

4.5.3 Energy dispersive spectroscopy results for CMOF-5

Figure 52 shows the elemental analysis for carbonised MOF-5. As shown in Table 21, the carbonisation has processed perfectly and all the zinc in the structure of the MOF evaporated.

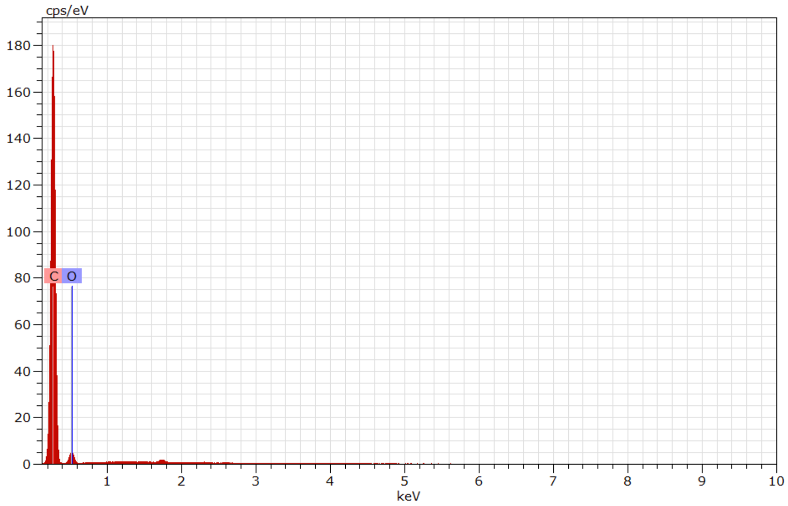

Figure 52: EDS analysis for C-MOF-5

Table 21: Elemental analysis data for C-MOF-5

Element	Weight%	Atomic%
C K	89.91	92.23
O K	10.09	7.77
Totals	100.00	10.00

4.5.4 Energy dispersive spectroscopy results for C-MIL-100(Fe)

Figure 53 and Table 22 show the elemental analysis data for carbonised MIL-100(Fe). As it is shown in Table 22, there are some traces of iron in the structure of the carbon, which is due to insufficient washing during the carbonisation.

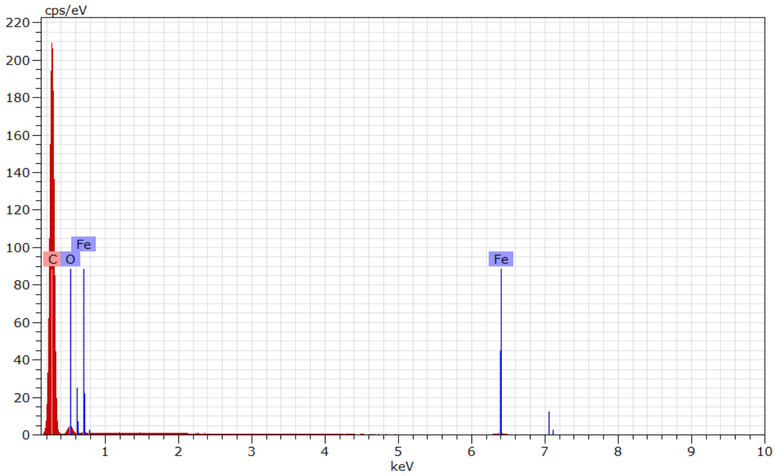

Figure 53: Elemental analysis for C-MIL-100(Fe)

Table 22: EDS analysis for C-MIL-100(Fe)

Element	**Weight%**	**Atomic%**
C	90.86	92.23
O	7.91	7.77
Fe	1.23	0.27
Totals	100.00	10.00

4.5.5 Transmission Electron Microscopy Results

Figure 54 shows morphology of the Pt/C_{ZIF-8}. The Pt loaded homogenously on the C_{ZIF-8} and was not agglomerated, and the particle size of the Pt seems to have be small enough to not to cover the support.

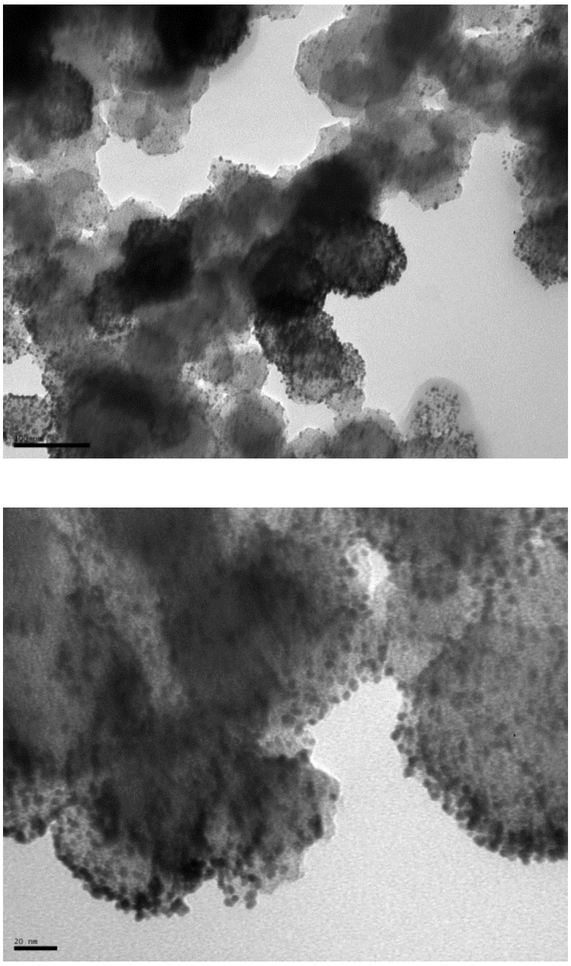

Figure 54: TEM images of Pt/$_{\mathrm{CZIF-8}}$

Chapter 5

5 Electrochemical Analysis

The electrochemical behaviour of the samples was measured using PEMFC and supercapacitors.

5.1 Electrochemical Surface Area

The Pt electrochemical surface area of Pt/C_{ZIF-8} and Pt/Vulcan was calculated from the hydrogen adsorption charge (Q_H) of the CV, shown in Figure 55.

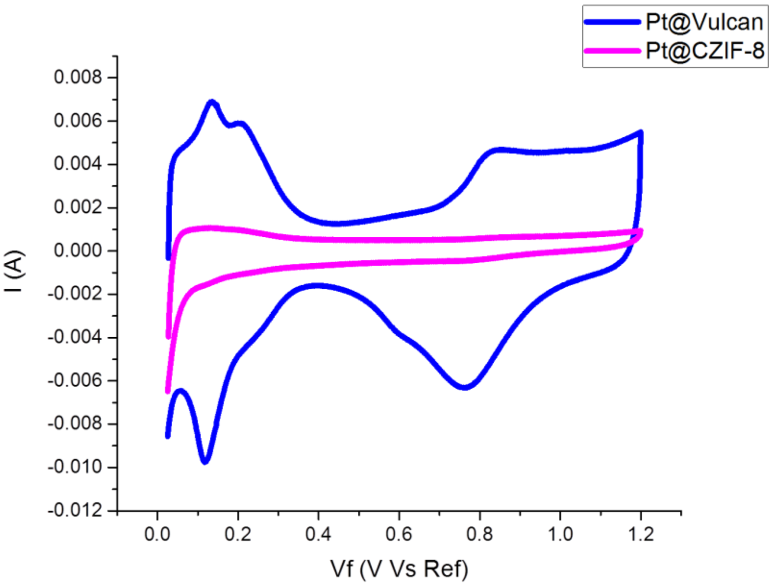

Figure 55: Comparison of CVs obtained from Pt/CZIF-8 and commercial Pt/Vulcan

Hydrogen adsorption charge Q_H for Pt/Vulcan was 1.641mC, so:

$$\text{ECSA Pt, cat} = \left[\frac{1.641\times10^{-3}}{210\ \mu C\ cm_{Pt}^{-2}\ 20*10^{-3}\ mg_{Pt}cm^{-2}\ 0.2475(cm^{2})}\right] \times 10^{5}$$

$$\boxed{\text{ECSA}_{\text{Pt, cat}}=105.26\ m^{2}/g}$$

hydrogen adsorption charge Q_H for synthesised Pt/C_{ZIF-8} calculated from the negative going potential scan was 109.8 µC, so:

$$\mathrm{ECSA\ Pt, cat} = \left[\frac{109.8 \times 10\text{-}6}{210\ \mu C\ cm_{Pt}^{-2}\ 20 \times 10\text{-}3\ \ mg_{Pt}cm^{-2}\ 0.2475(cm^2)}\right] \times 10^5$$

$$\boxed{\mathrm{ECSA}_{\mathrm{Pt,\ cat}} = 10.58\ m^2/g}$$

The low electrochemical surface area of the Pt/C_{ZIF-8} can be a result of not having well-dispersed Pt on the carbon support. It is also possible that not all the Pt was accessible due to the small pores in the support. The other possible reason could be Pt particle size, which was bigger than the commercial size.

5.2 Oxygen Reduction Reaction Results

The comparison results of an anodic sweep of the ORR polarisation curves at 1600 rpm are illustrated in Figure 56. The ORR polarisation curve obtained for commercial Pt/Vulcan has a single reduction wave, and the limiting current density plateau is well developed. The ORR polarisation curve or Pt/C_{ZIF-8} also has a single reduction curve; however, there are some avoidable noise disturbs on the curve, which could be due to bad contact of the working electrode to the rotator.

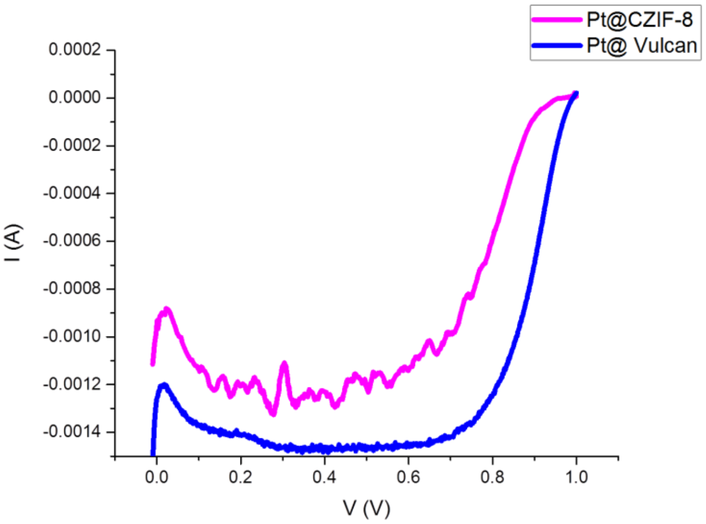

Figure 56: Comparison of the ORR polarisation curves of the commercial Pt/Vulcan and synthesised Pt/C_{ZIF-8} at the rotation rate of 1600 rpm

The Koutecky-Levich plot was derived from all the rotation rates 400, 800, 1200 and 1600 rpm and the intercept ($1/A^{-1}$) was derived from the Koutecky-Levich plot of the ORR polarisation curves with rotation rates at potential 0.9 V. The intercept for Pt/Vulcan was 339.1 A^{-1}.

The intercept ($1/I^{-1}$) derived from the polarisation curve at potential 0.9 V for Pt/C_{ZIF-8} was $9.894*10^{-3}$ A^{-1}. By applying the kinetic current in Equation 11, the specific capacitance for Pt/Vulcan and Pt/ C_{ZIF-8} was calculated, and is presented in Table 23.

$$\text{Pt/Vulcan: } I_s\,(\mu A\ cm_{Pt}^{-2}) = \frac{2.95*10^{-3}}{1.092*10^{-3}/210\ \mu C\ cm_{Pt}^{-2}}$$

Is = 567.307 ($\mu A\ cm_{Pt}^{-2}$), Pt/C_{ZIF-8}:

$$I_s\,(\mu A\ cm_{Pt}^{-2}) = \frac{1.01*10^{-4}}{109.8*10^{-6}/210\ \mu C\ cm_{Pt}^{-2}}$$

Is = 193.190(µA cm$_{Pt}^{-2}$).

Table 23: Comparison of kinetic current (I_K) and specific capacitance (I_S) of the commercial Pt/Vulcan and Pt/CZIF-8

Sample	**intercept (I) (1/A)**	**I_k=1/Intercept (A)**	**Q_H**	**(I_S)specific activity (μAcm_{Pt}^{-2})**
Pt/Vulcan (Sigma-Aldrich)	339.1	0.00295	0.001418	567.3076923
Pt/C_{ZIF-8}	9894	0.000101	0.0001098	193.1905126

The specific activity of the synthesised catalyst is lower than the commercial one, which is as a result of a lower electrochemical surface area in the former**.**

5.3 Durability Test

The durability of the prepared catalyst was evaluated by measuring the change in the double layer capacitance from the catalyst support as a function of cycling numbers. The change of double layer capacitance of catalyst support for synthesised and commercial supports is illustrated given in Table 24 and Table 25 respectively as a function of cycling numbers.

Figure 57 shows the change of double layer capacitance as a function of cycling numbers. Increase in capacitance means an increase in oxygenated functional groups on the surface of the sample. As shown in Figure 57, the synthesised carbon had a larger change in capacitance in comparison to the Ketjen carbon, which may have been a result of the high BET surface area of the C_{ZIF-8}, which showed lower stability compared to the commercial carbon supports.

Table 24: Double layer capacitance and normalised double layer capacitance of the Pt/CZIF-8

Amps (Coulombs /Volts)	Double layer capacitance	Double layer capacitance normalised	number of cycles
8×10^{-5}	2.96×10^{-4}	8.0.2	0
1.01×10^{-4}	3.69×10^{-4}	100	10
1.26×10^{-4}	4.60×10^{-4}	124.75	100
1.40×10^{-4}	5.11×10^{-4}	138.61	200
1.07×10^{-4}	3.90×10^{-4}	105.84	500
1.92×10^{-4}	7.01×10^{-4}	190.09	1000

Table 25: Double layer capacitance and normalised double layer capacitance of the commercial Ketjen black

Amps (Coulomb/Volts)	double layer capacitance	normalised double layer capacitance	number of cycles
3.90×10^{-5}	1.58×10^{-4}	72.49	0
5.38×10^{-5}	2.18×10^{-4}	100	10
2.10×10^{-5}	8.50×10^{-4}	39.03	100
6.38×10^{-5}	2.58×10^{-4}	118.58	200
7.06×10^{-5}	2.86×10^{-4}	131.22	500
8.44×10^{-5}	3.42×10^{-4}	156.87	1000

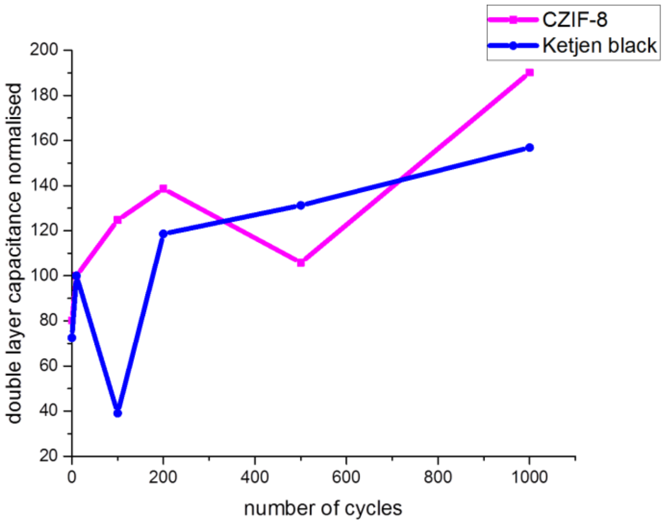

Figure 57: Change of double layer capacitance of catalyst support as a function of cycling numbers

5.4 Supercapacitor Results

5.4.1 CZIF-8 cyclic voltammetry

The specific capacitance of the CZIF-8 was measured using CV in the potential window of 0-0.8 V at different sweep rates; 5, 20, 40, 60, 80, 100, 200, 300,4 00 and

500 mV s^{-1}. Figure 58 shows the mirror symmetric and stable CV curves, confirming the stability of the carbon.

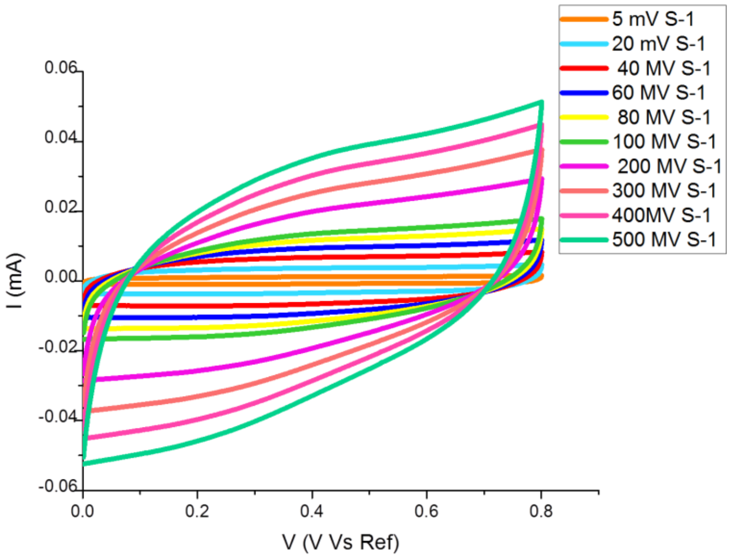

Figure 58: Cyclic voltamoogram for CZIF-8 at different sweep rates

5.4.1.1 Galvanostatic charge–discharge

The Galvanostatic charge–discharge curve of the carbonised ZIF-8 was measured at the potential window of 0–0.8 V at the current density of the 0.1 A g^{-1}, and the results are provided in Figure 59. The specific capacitance of C-ZIF-8 was calculated using the discharge time.

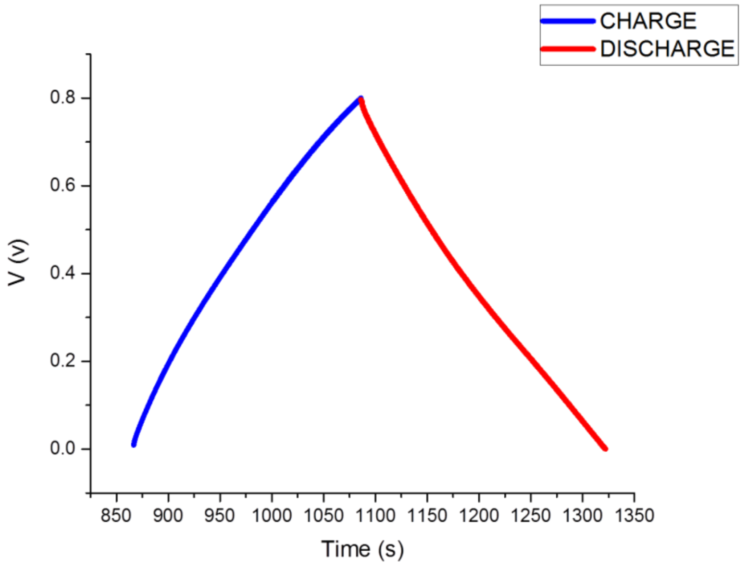

Figure 59: Cyclic charge–discharge curve of C-ZIF-8 at 0.1 A g^{-1}

The specific capacitance was calculated from Equation 13 as follows:

m = 0.003315g, ΔV = 0.8V, I = 3.315 x 10^{-4} (A)

$$C = \frac{I}{m} \text{ x } \frac{\Delta \text{t}}{V}$$

$$C = 3.315 \text{ x } 10^{-4} \times \frac{563}{0.8}$$

$$C = 70.375 \ \text{Fg}^{-1}$$

The calculated specific capacitance is much higher than the previous study by (Young et al., 2016) in which they obtained the result of 56.8 F g^{-1}, and the commercial graphite. This result shows that the carbonised ZIF-8 can be a potential substitute for commercial carbon.

5.4.2 CMOF-5

5.4.2.1 Cyclic voltammetry

The CV of the C-MOF-5 was performed at potential window of -1–0 V at different sweep rates; 5, 20 ,40, 60, 80, 100, 200, 300, 400 and 500 mV s^{-1}. Figure 60 shows the CV curve for this MOF, which is not as stable as C-ZIF-8.

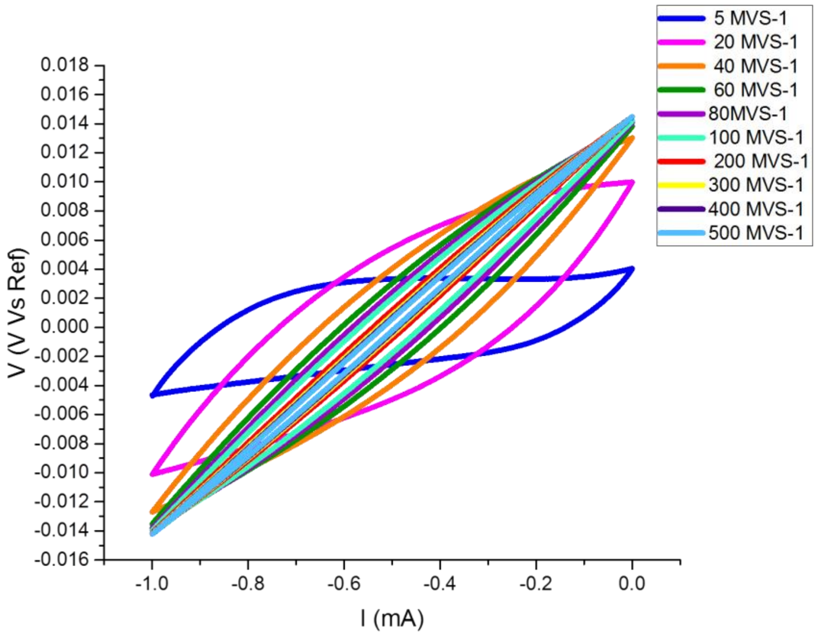

Figure 60: CV of C-MOF-5

5.4.2.2 Charge discharge

The galvanostatic charge–discharge curve for C-MOF-5 at current density of 0.25 A g^{-1} at the potential window of -1–0 is shown in Figure 61. The specific capacitance was calculated using Equation 13.

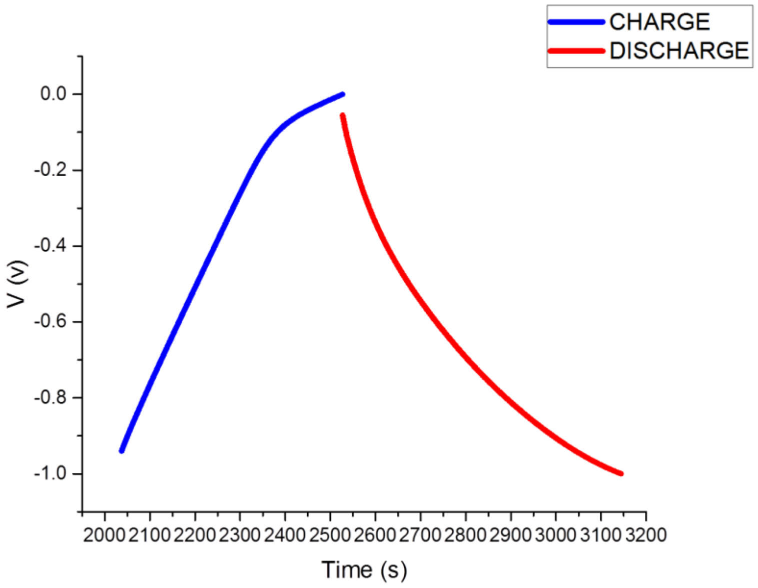

Figure 61: Galvanostatic charge-discharge at current density of 0.25 A g^{-1}

The specific capacitance was calculated from Equation 13 as follows:

m = 4.4 x 10^{-3}g, ΔV = 1V, I = 1.1 x 10^{-3} (A).

$$C = \frac{I}{m} \text{ x } \frac{\Delta t}{V}$$

$$C = 0.25 \text{ x } \frac{639}{1}$$

$$C = 159.75 \ \text{Fg}^{-1}$$

The calculated specific capacitance for C-MOF-5 is much higher than the commercial carbon. It is also comparable to the previous study by (Hu et al., 2010), in which they yielded 72 F g^{-1}. This result shows that CMOF-5 with both micro- and mesopores can be a good alternative to the commercial graphite carbons.

5.4.3 C-MIL-100(Fe)

5.4.3.1 Cyclic voltammetry

The specific capacitance of the C-MIL-100(Fe) was measure using CV in the potential window of -1–0 V at different sweep rates; 1, 2, 5, 10, 20, 50, 100, and 200 mV s^{-1}. As shown in Figure 62, the cyclic voltammograms are not stable as was expected. This result indicates that this carbon cannot be a substitute for the commercial carbons.

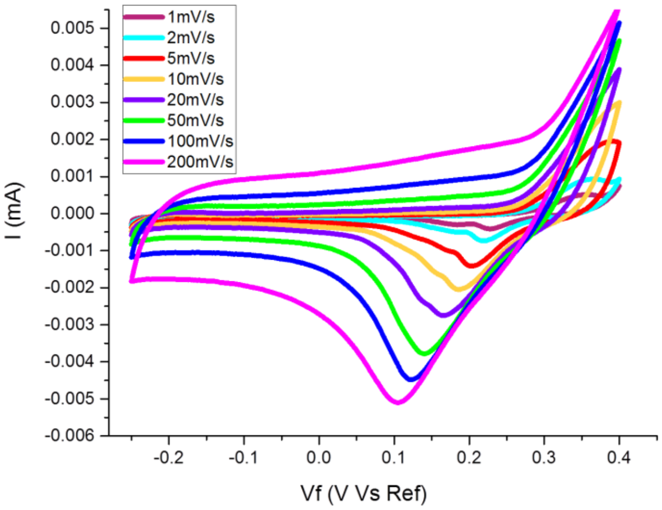

Figure 62: CV of C-MIL-100 at different sweep rates

5.4.3.2 Galvanostatic charge-discharge

Figure 63 shows the cyclic charge–discharge curve for C-MIL-100(Fe). The galvanostatic charge–discharge of the C-MIL-100(Fe) was performed at the potential window of -0.25–0.4 V, and the specific capacitance at the current density of 0.01 A g^{-1} was calculated using Equation 13.

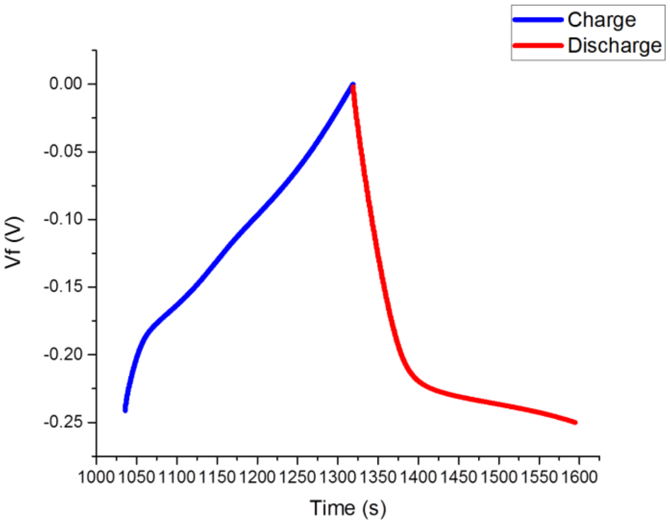

Figure 63: Galvanostatic charge–discharge for C-MIL-100 at 0.01A g^{-1}

$$C = \frac{I}{m} \text{ x } \frac{\Delta \text{t}}{V}$$

$$C = 0.01 \text{ x } \frac{276}{0.65}$$

$$C = 4.246 \text{ Fg}^{-1}$$

The specific capacitance for CMIL-100(Fe) exhibited very low value. This can be due to the very low surface area of the CMIL-100, showing that this carbon is not a good substitute for the commercial one.

5.5 Conclusion

The results obtained from the electrochemical measurements reveal that the MOF-derived carbon can potentially be good substitutes for the supercapacitors, and the best results are obtained from the carbon with both micro- and mesopores in their structures. However, these carbons do not have a good performance in PEMFC industries, as the Pt loading blocked some of the pores of the carbons, hence decreased electron transfer.

Chapter 6

6 Immersion Calorimetry Results

In order to evaluate the adsorption abilities of the selected MOFs, they were characterised by immersion calorimetry using Setaram Tian-Calvet C80D calorimeter. For more accuracy, each sample was measured twice and the average of the results was used in this research.

To calculate the heat of adsorption of the Xylene isomers on different MOFs and MOF-derived carbons, the area under the curve of heat exchange was integrated, and by applying the Antoine equation, the final result was calculated. The properties of xylene isomers are given in Table 26.

Table 26: Xylene isomer properties

Properties	O-xylene	M-xylene	P-xylene
Density (g/cm^3)	0.88	0.86	0.86
A (component-specific constants)	7.14914	7.1815	7.15471
B (component-specific constants)	1566.59	1573.0243	1553.95
C (component-specific constants)	222.671	226.671	225.23
ΔH vap. (kJ mol^{-1})	45	43	41
T experiment (°C)	30	30	30
Kinetic diameter (nm) (d_k)	0.74	0.71	0.67

6.1 HKUST – Calorimetry Measurements

Commercial HKUST purchased from Sigma-Aldrich was used to study the adsorption behaviour oh HKUST in xylene isomers.

6.1.1 HKUST in O-Xylene

Figure 64 shows the amount of heat released from the adsorption of the O-xylene on HKUST. The heat of adsorption was calculated and is given in Table 27 from the area under the curve.

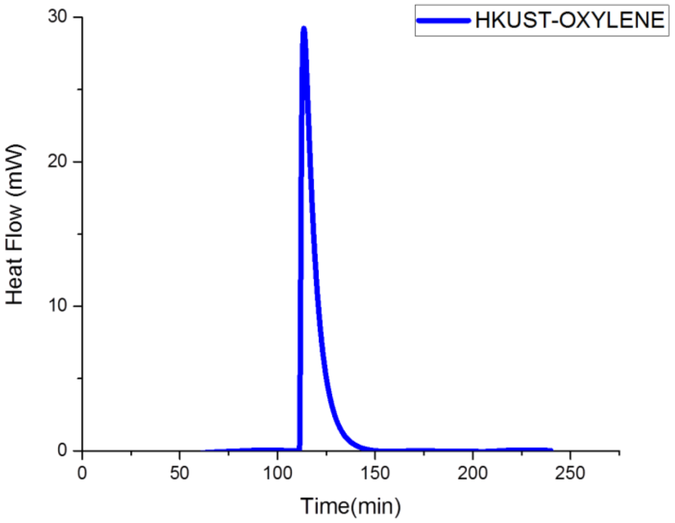

Figure 64: Heat of adsorption released from HKUST-1 in O-xylene

The measured amount of O-xylene adsorbed by HKUST was measured and plotted against the time, and from the integration of the area under the curve, the amount of the O-xylene adsorbed on the HKUST was calculated. The results are given in Table 27.

6.1.2 HKUST in M-Xylene

Figure 65 shows the heat of adsorption released from HKUST immersed in M-xylene.

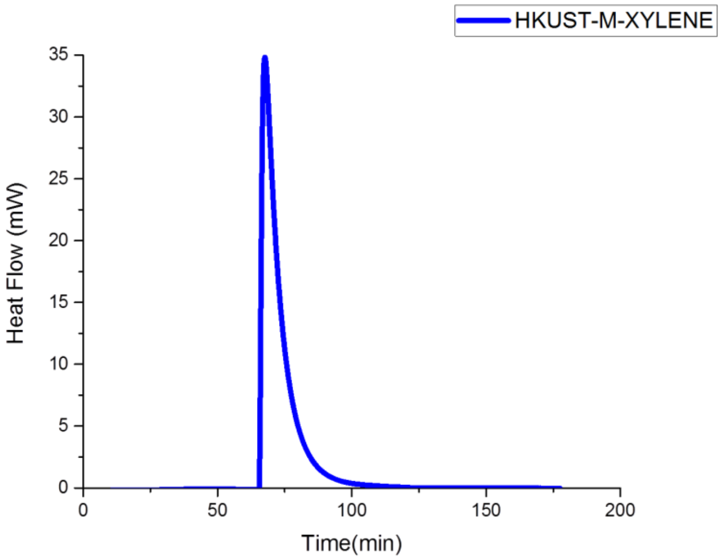

Figure 65: Heat of adsorption released from HKUST in M-xylene

6.1.3 HKUST in P-Xylene

Figure 66 shows the adsorbed amount of the P-xylene on the commercial HKUST-1. The heat of adsorption was calculated from the area under the curve.

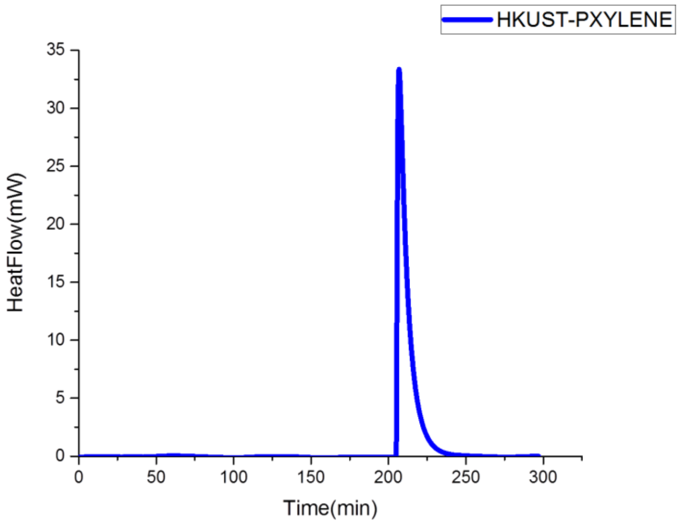

Figure 66: Heat of adsorption released from HKUST in P-xylene

6.1.4 Table of calorimetry data

Table 27 shows the details of the experiments and the calculated heat of adsorption of HKUST-1.

Table 27: Experimental details of the HKUST-1 calorimetry in xylene isomers

HKUST-1	O-Xylene	M-Xylene	P-Xylene
m_1	8.8008	8.6882	8.8133
m_2	8.9043	8.7883	8.9184
m_3	9.0108	8.8772	8.994
m_4	8.9932	8.8597	8.9754
m_5	1.6211	1.5794	1.7656
m_6	2.027	2.082	2.2477
Degassed weight (g)	0.0859	0.0826	0.0865
Liquid mass (g)	0.4059	0.5026	0.4821
Liquid volume. (mL)	0.46125	0.584419	0.560581
Liquid volume (L)	0.000461	0.000584	0.000561
P_o (mmHg)	8.892463	11.29633	11.64877
P_o (atm)	0.011701	0.014864	0.015327
Moles dissolved evap.	2.17E-07	3.49E-07	3.46E-07
Heat of evaporation (mJ)	9.769793	15.02603	14.17154
Released heat (J/g)	187.265	205.771	145.96
Released heat mJ)	16086.06	16996.68	12625.54
Heat of adsorption (mJ)	16095.83	17011.71	12639.71
Heat of adsorption (J/g)	187.3787	205.9529	146.1238

The calculated results for adsorption of the xylene isomers on the HKUST show that this molecule adsorbed a large amount of xylene isomers; however, this amount is slightly higher for the meta xylene isomer, which can be due to the interaction with the open metal sites of this MOF.

6.2 ZIF-8 Calorimetry Measurements

6.2.1 ZIF-8 in O-xylene

The heat of adsorption of O-xylene on ZIF-8 was calculated from the area under the curve of the released heat, as shown in Figure 67. The calculated heat of adsorption of all xylene isomers for ZIF-8 is given in Table 28.

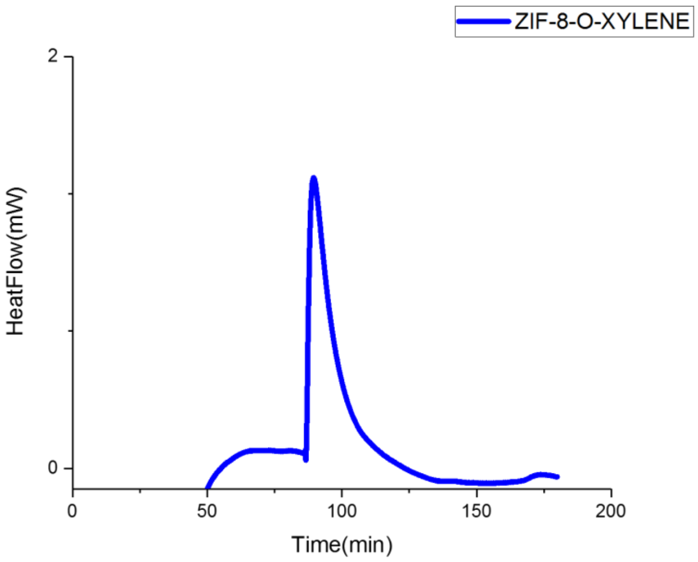

Figure 67: Heat of adsorption released from ZIF-8 in O-xylene

6.2.2 ZIF-8 in M-Xylene

Figure 68 reveals the amount of heat released during the adsorption of the M-xylene on ZIF-8.

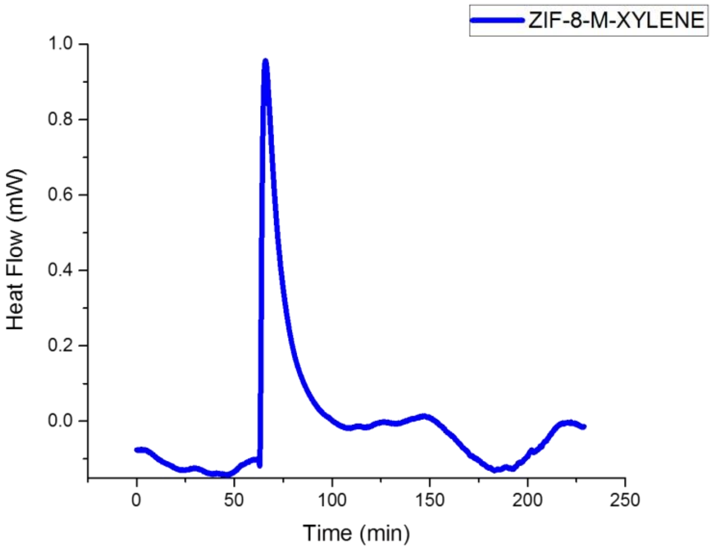

Figure 68: Heat of adsorption released from ZIF-8 in M-xylene

6.2.3 ZIF-8 in P-xylene

Figure 69 reveals the amount of heat released during the adsorption of the P-xylene on ZIF-8. The heat of adsorption has been calculated from the area under the curve.

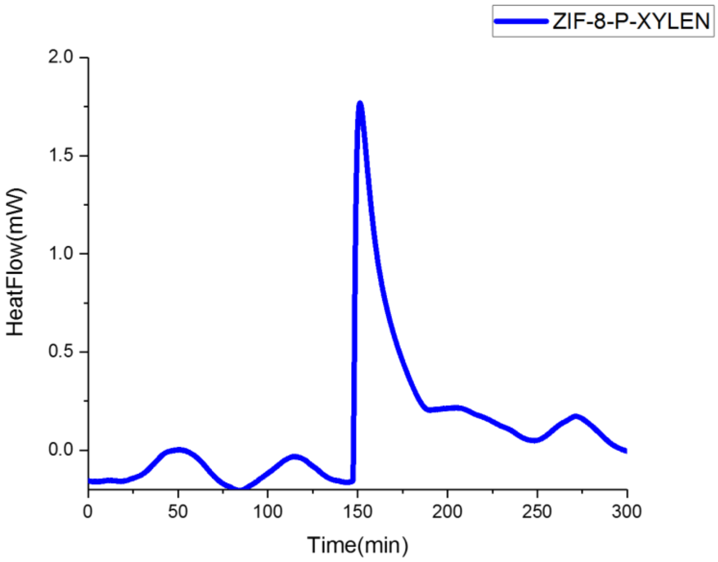

Figure 69: Heat of adsorption released from ZIF-8 in P-xylene

6.2.4 Table of calorimetry data

The details of the experimental results of the adsorption selectivity for ZIF-8 are given in Table 28. The comparison of the adsorbed heat of different isomers of the xylenes by ZIF-8 reveals that the pores of this MOF have adsorbed at a very low volume xylene molecules, which shows there is no accessibility for the molecules of xylene isomers to the pores of ZIF-8. This result can be explained due to the small pore aperture (0.34 nm) of the ZIF-8, which does not allow xylene isomers to pass through.

Table 28: Experimental detailsof the ZIF-8 adsorption of xylene isomers

ZIF-8	O-xylene	M-xylene	P-xylene
m_1	8.6309	8.7258	8.6427
m_2	8.7293	8.8241	8.7342
m_3	8.7857	8.9483	8.8498
m_4	8.7844	8.9478	8.8493
m_5	1.7645	1.5454	1.5961
m_6	2.1746	1.903	2.0091
Degassed weight (g)	0.0971	0.0978	0.091
Liquid mass (g)	0.4101	0.3576	0.413
Liquid volume (mL)	0.46602273	0.41581395	0.48023256
Liquid volume (L)	0.00046602	0.00041581	0.00048023
P_o (mmHg)	8.89246286	11.2963299	11.6487669
P_o (atm)	0.01170059	0.01486357	0.0153273
Moles dissolved evap.	2.1935E-07	2.4863E-07	2.9611E-07
Heat of evaporation (mJ)	9.87088477	10.6910237	12.1403114
Released heat (J/g)	8.187	8.032	22.95
Released heat mJ)	794.9577	785.5296	2088.45
Heat of adsorption (mJ)	804.828585	796.220624	2100.59031
Heat of adsorption (J/g)	8.2886569	8.14131517	23.08341

6.3 UiO-66 Immersion Calorimetry Measurements

6.3.1 UiO-66 in O-xylene

The heat of adsorption of O-xylene on UiO-66 was recorded and plotted against time (Figure 70), and the amount of heat of adsorption was calculated from the area under the curve.

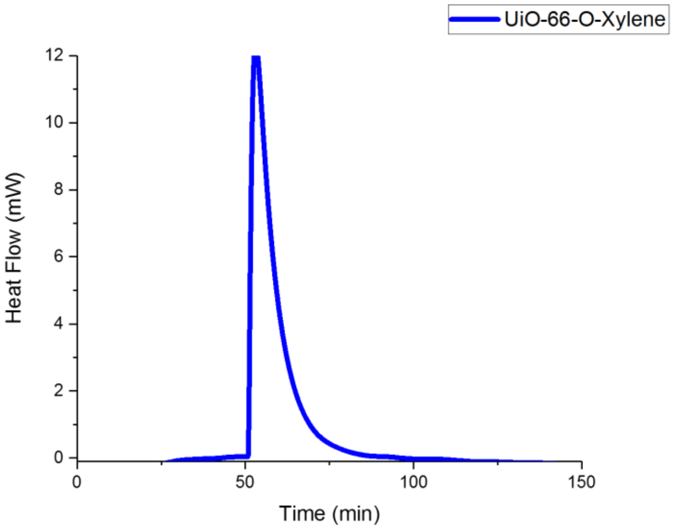

Figure 70: Released heat from the adsorption of O-xylene on UiO-66

6.3.2 UiO-66 in M-xylene

Figure 71 shows the amount of heat released from the adsorption of the M-xylene on UiO-66. The value of the heat of adsorption has been calculated from the area under the curve.

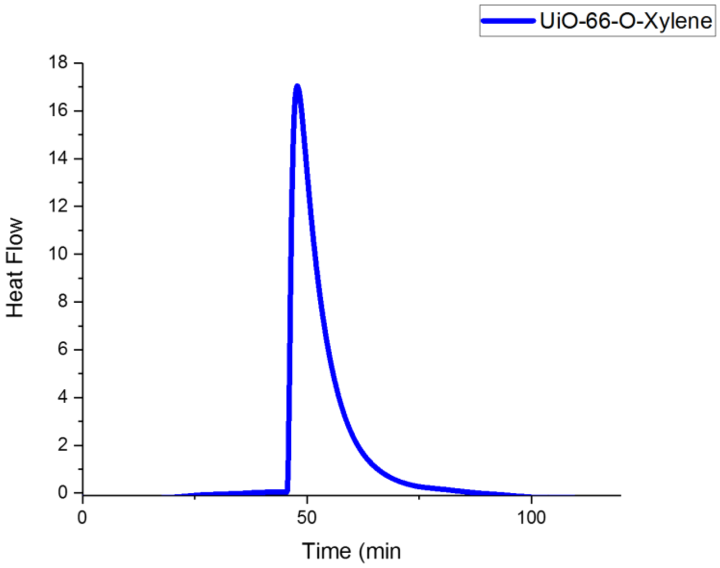

Figure 71: Released heat from the adsorption of M-xylene on UiO-66

6.3.3 UiO-66 in P-xylene

Figure 72 illustrates the amount of heat released from the adsorption of the P-xylene on UiO-66. The heat of adsorption for the all isomers of xylene was calculated and corrected with regards to the Antoine equation, and the results are provided in Table 29.

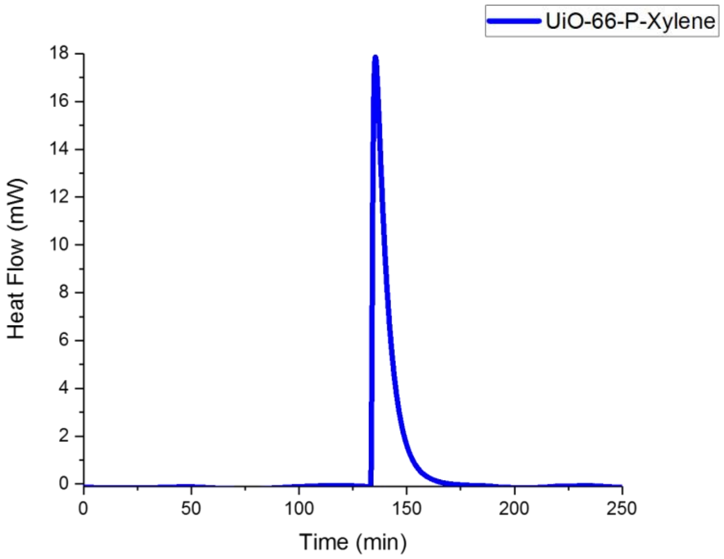

Figure 72: Heat of adsorption released from UiO-66 in P-xylene

6.3.4 Table of calorimetry data

The details of the experiments and the calculated results for the UiO-66 samples are given in Table 29. The amount of xylene adsorbed on the UiO-66 shows that the adsorption selectivity of this MOF for O-xylene and M-xylene is higher than the P-xylene. These results show the reverse shape selectivity of UiO-66 for xylene adsorption. As can be seen, UiO-66 has shown reverse shape selectivity, which can be due to the place of the methyl group in the structure of the molecule

Table 29: Experimental details of the UiO-66 adsorption of xylene isomers

UiO-66	O-Xylene	M-Xylene	P-Xylene
m_1	8.7044	8.655	8.7908
m_2	8.8083	8.7401	8.8883
m_3	8.9713	8.9306	9.024
m_4	8.9583	8.9203	9.0123
m_5	1.7815	1.524	1.6238
m_6	2.259	1.7702	2.0032
Degassed weight (g)	0.0909	0.0748	0.0858
Liquid mass (g)	0.4775	0.2462	0.3794
Liquid volume (mL)	0.542613636	0.28627907	0.441162791
Liquid volume (L)	0.000542614	0.000286279	0.000441163
P_o (mmHg)	8.892462861	11.29632985	11.64876695
P_o (atm)	0.011700594	0.014863572	0.015327305
Moles dissolved evap.	2.55404E-07	1.71175E-07	2.72015E-07
Heat of evaporation (mJ)	11.49316625	7.360542583	11.15262501
Released heat (J/g)	111.72	109.84	101.732
Released heat mJ)	10155.348	8216.032	8728.6056
Heat of adsorption (mJ)	10166.84117	8223.392543	8739.758225
Heat of adsoption (J/g)	111.8464375	109.938403	101.861984

6.4 UiO-67 Immersion Calorimetry Measurements

6.4.1 UiO-67 in O-xylene

Figure 73 shows the amount of heat of adsorbed of O-xylene on UiO-67.

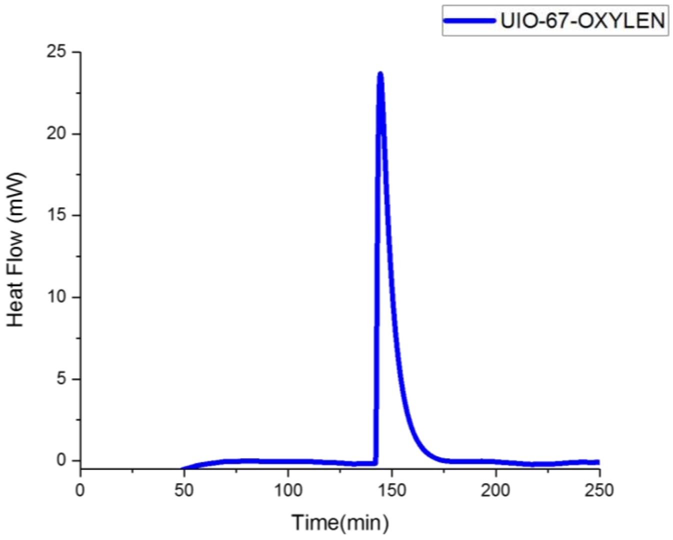

Figure 73: Heat of adsorption released from UiO-67in O-Xylene

6.4.2 UiO-67 in M-xylene

The heat of adsorption of the M-xylene on UiO-67 is illustrated in Figure 74.

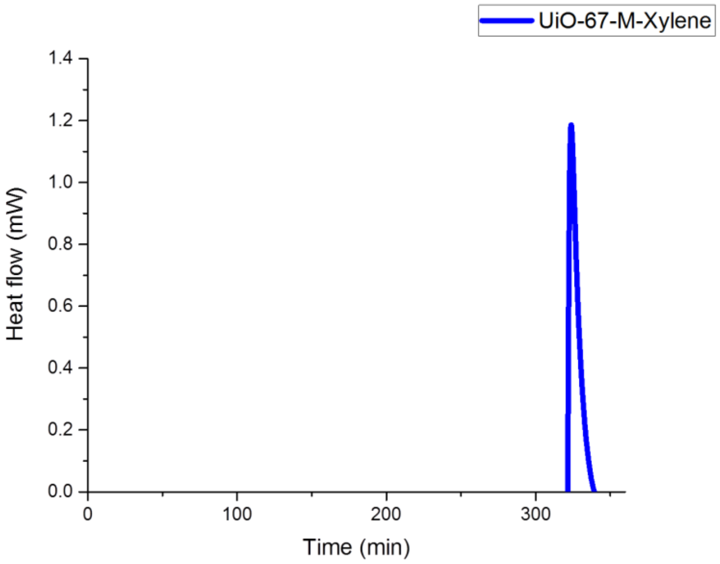

Figure 74: Heat of adsorption released from UiO-67 in M-xylene

6.4.3 UiO-67 in P-xylene

Figure 75 illustrates the amount of P-xylene adsorbed on the UiO-67. The heat of adsorption for all the isomers of xylene was calculated and corrected with regards to the Antoine equation. Results are provided in Table 30.

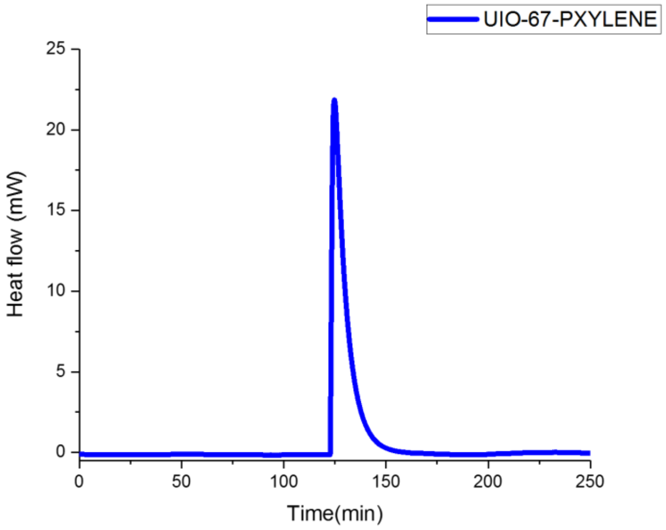

Figure 75: Heat of adsorption released from UiO-67 in P-xylene

6.4.4 Table of calorimetry data

The details of the experimental results of the adsorption selectivity for UiO-67 are given in Table 30.

Table 30: Experimental details of the UiO-67 adsorption of Xylene isomers

UiO-67	O-Xylene	M-Xylene	P-Xylene
m_1	8.6193	8.4686	8.7151
m_2	8.705	8.5392	8.7949
m_3	8.791	8.6685	8.8659
m_4	8.7858	8.6622	8.8603
m_5	1.7001	1.5186	1.3823
m_6	2.1512	1.9539	1.743
Degassed weight (g)	0.0805	0.0643	0.0742
Liquid mass (g)	0.4511	0.4353	0.3607
Liquid volume (mL)	0.51261364	0.506163	0.4194186
Liquid volume (L)	0.00051261	0.000506	0.00041942
P_o (mmHg)	8.89246286	11.29633	11.6487669
P_o (atm)	0.01170059	0.014864	0.0153273
Moles dissolved evap.	2.4128E-07	3.03E-07	2.5861E-07
Heat of evaporation (mJ)	10.8577326	13.01399	10.6029305
Released heat (J/g)	147.574	7.234	142.173
Released heat (mJ)	11879.707	465.1462	10549.2366
Heat of adsorption (mJ)	11890.5647	478.1602	10559.8395
Heat of adsorption (J/g)	147.708879	7.436395	142.315897

The results calculated for the adsorption selectivity of the UiO-67 reveal that this molecule is better in adsorbing O-xylene and P-xylene than M-xylene. These results show that this MOF can be used for the separation of o-xylene and p-xylene.

6.5 C-UiO-66

Since UiO-66 showed reverse shape selectivity, we decided to run the test for the carbonised sample and compare the results with the original MOF to see whether or not the MOF keeps its reverse shape selectivity after carbonisation as well.

6.5.1 C-UiO-66 in M-xylene

Figure 76 shows the amount of m-xylene adsorbed on C-UiO-66. The heat of adsorption of the C-UiO-66 was calculated from the area under the curve of the released heat and was corrected with regards to the Antoine equation. The details are given in Table 31.

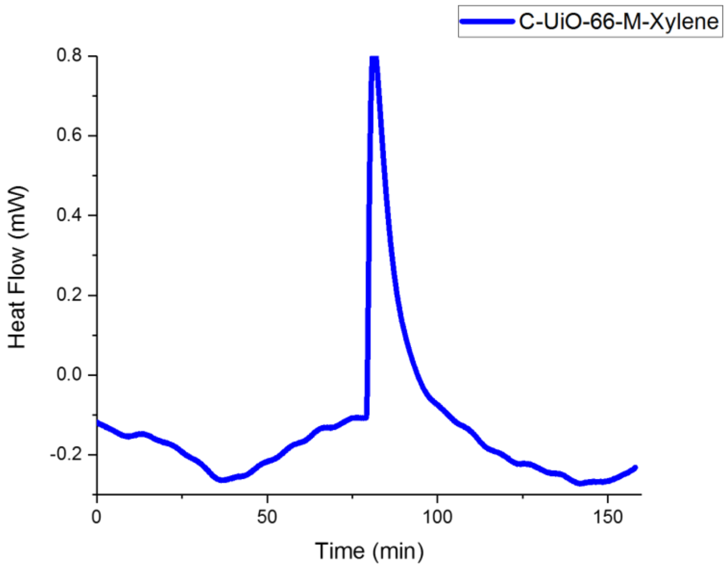

Figure 76: Heat of adsorption released from C-UiO-66 in M-xylene

6.5.2 Table of calorimetry data

The full details of the experimental results for the adsorption selectivity of the C-UiO-66 are given in Table 31. The very low value of the heat of adsorption for the carbonised UiO-66 reveals that this carbon does not have accessible pores to the m-xylene. Since there was no accessibility for the M-xylene to enter to the pores of C-UiO-66, the experiment was not repeated for other isomers.

Table 31: Experimental details of the C-UiO-66 adsorption of xylene isomers

C-UiO-66	M-Xylene
m_1	8.668
m_2	8.7676
m_3	8.8518
m_4	8.851
m_5	1.6935
m_6	2.0639
Degassed weight (g)	0.0988
Liquid mass (g)	0.3704
Liquid volume (Sopian and Wan Daud)	0.430697674
Liquid volume (L)	0.000430698
P_o (mmHg)	11.29632985
P_o (atm)	0.014863572
Moles dissolved evap.	2.57528E-07
Heat of evaporation (mJ)	11.07370013
Released heat (J/g)	4.245
Released heat mJ)	419.406
Heat of adsorption (mJ)	430.4797001
Heat of adsorption (J/g)	4.357081985

6.6 C-HKUST

6.6.1 C-HKUST in M-xylene

The amount of released heat from the adsorption of the M-xylene on HKUST is illustrated in Figure 77. The very low heat of adsorption of the m-xylene on HKUST shows there is no accessibility to the pores of the HKUST, hence the experiments were not repeated for the other isomers.

6.6.1 Table of calorimetry data

The full details of the experimental results for the adsorption selectivity of the C-HKUST are given in Figure 77. The very low value of the heat of adsorption for the carbonised HKUST reveals that this carbon does not have accessible sites to the m-xylene. Since there was no accessibility for the m-xylene to enter to the pores of C-HKUST, the experiment was not repeated for other isomers.

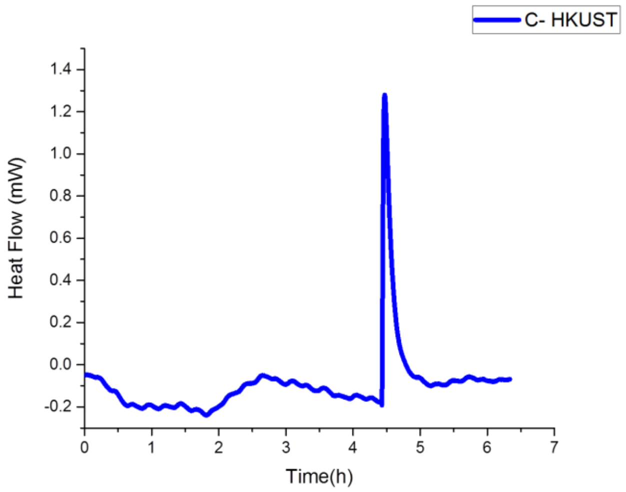

Figure 77: Heat of adsorption of C-HKUST

Table 32: Experimental deails of the dasorption of M-xylene on C-HKUST

C-HKUST	M-Xylene
m_1	8.5896
m_2	8.676
m_3	8.7931
m_4	8.793
m_5	1.7092
m_6	2.152
Degassed weight (g)	0.0863
Liquid mass (g)	0.4428
Liquid volume (mL)	0.514884
Liquid volume (L)	0.000515
P_o (mmHg)	11.29633
P_o (atm)	0.014864
Moles dissolved evap.	3.08E-07
Heat of evaporation (mJ)	13.23821
Released heat (J/g)	2.71
Released heat mJ)	233.873
Heat of adsorption (mJ)	247.1112
Heat of adsorption (J/g)	2.863398

6.7 Conclusion

The comparison of all calorimetry results show that the highest heat of adsorption belongs to the adsorption of M-xylene on to the HKUST-1. Considering the dimensions of the xylene isomers, where P-xylene is the smallest and O-xylene is the biggest isomer, we were expecting to gain the highest adsorption of P-xylene. For this reason, we decided to make a replica from HKUST and compare the result of the replica with the original MOF, where we observed no adsorption occurring on the replica sample. Since UiO-66 showed the reverse shape selectivity for the adsorption of xylene isomers, we decided to try the test for the replica of UiO-66 as well, which resulted in no adsorption on the replica of UiO-66. In addition, the results reveal that UiO-67 is more favourable for adsorbing O-xylene and P-xylene, hence can be applied for the separation of these isomers.

Chapter 7

7 Conclusion

Different MOFs with different pore structures were synthesised and characterised used PXRD and BET. The comparison of the PXRD results of the synthesised samples were in agreement with the simulated data, illustrating the crystalline structure and successful synthesis of MOFs.

The BET surface area of the synthesised MOFs and MOF-derived carbons was measured under nitrogen at 77 K using the BET method. The surface area of the ZIF-8 was as high as 1588 m^2/g, which is higher than the reported data in the literature (1173 m^2/g) (Pan et al., 2011). The surface area for Ni-MOF-74 was obtained as 1135 m^2/g, which is in agreement with the literature. MIL-100(Fe) surface area was calculated as 1645 m^2/g, which matched with the value reported in the literature (1343 m^2/g) (Jeremias et al., 2012). However, the surface area obtained for MIL-53(Al) was 274 m^2/gr, which is lower than the value reported in the literature (1163 m^2/gr) (Karikkethu Prabhakaran and Deschamps, 2015). MIL-110(Al) also revealed a very low surface area (452 m^2/g); it was expected to be 1400 m^2/g as reported in the literature (Volkringer et al., 2007) As the PXRD patterns for both MIL-53(Al) and MIL-110(Al) were in agreement with the simulated data, the low surface areas for these MOFs can be as a result of having some solvents trapped in the pores of the MOFs, which can be removed by further activation. This process will be conducted in future work.

The EDS results obtained from the microwave-assisted synthesise method did not show the homogenous loading of the Pt, which then improved by applying different method suggested by (Yang et al., 2003). The elemental analysis of the Pt loaded carbon following this method illustrated the homogenous loading of Pt on both carbonised MOF and Vulcan.

So far, we can conclude that the synthesis and activation method for MIL-53(Al) and MIL-110(Al) needs to be improved, and the characterisation of these MOFs needs to be recalculated to obtain an acceptable result.

In addition, the results from fuel cell test show that these materials are not the best support materials for fuel cell application and potentially can be good support materials for Li-ion batteries and supercapacitors applications. The results from the TEM show that there was no agglomeration of the Pt on the support, and they were dispersed well. However, the low ECSA of the Pt/C_{ZIF-8} could be due to the non-homogenous platinisation of the carbons. Also, we believe that since the CZIF-8 has micropores, the Pt coating could have blocked them, preventing the electrons from flowing easily. On the other hand, the MOF-derived carbons had better performance as electrodes in the supercapacitors tests. The specific capacitance calculated from cyclic charge–discharge for C_{ZIF-8} and C_{MOF-5} was higher than that of the commercial carbon; however, the C-MIL-100(Fe) did not show any good result, which we believe is due to the very low surface area of that carbon.

Finally, the adsorption ability of ZIF-8, HKUST, UiO-66 and UiO-67 was evaluated using the immersion calorimetry technique. ZIF-8 had the lowest interest of adsorption of xylene isomers due to the narrow pore aperture, which is smaller than the kinetic diameters of all xylene isomers. HKUST-1 gained the highest value for the heat of adsorption; however, the replica of this MOF did not adsorb any xylene isomer.

UiO-66 and UiO-67 also showed good performance in the adsorption of the xylene isomers. However, UiO-66 showed a reverse shape selectivity, which encouraged us to make the replica and assess its adsorption ability. The replica did not show any adsorption capability, which we believe is due to the change in the surface chemistry of the MOF after carbonisation.

Chapter 8

8 Recommendations for Future Study

The main goal of this study was to evaluate the effect of the microporosity of the carbon materials used in electrocatalysts and electrodes on the performance of fuel cells and supercapacitors. We also aimed to evaluate the adsorption ability of the MOFs and MOF-derived carbons. Different MOFs with different pore sizes were thus synthesised, characterised and carbonised. In case of the fuel cell measurements, the sample was loaded with Pt; however, there was some difficulties at the stage of catalyst preparation, which need to be rectified as a part of the future works. It is recommended that the platinisation of the carbonised MOFs be optimised. As these carbons have micropore structures, it is crucial to apply the platinisation in a way that the pores do not got blocked with the Pt particles. Also, it is recommended that MOF-derived carbons be synthesised with both micro- and mesopore structures to enhance the electrochemical behaviour of these MOFs. It is recommended that the conductivity of the MOF-derived carbons be evaluated with respect to the mechanism of the carbonisation, and the result optimised by choosing the best MOF precursor considering the pore structure of the MOF. Overall, this research can be expanded by the synthesis and characterisation of new MOFs and their polymerisation, and applying them in the other fields of the electrochemical devices such as l-ion batteries to optimise the performance of such devices. Moreover, it is recommended that the pore size structure of the MOF-derived carbons be controlled by controlling the carbonisation process to enhance the adsorption ability of these materials. It is possible to control the pore structure of the carbon by choosing the appropriate MOF, so this property of the MOFs can be used for the separation studies using adsorption phenomena.

References

- AFSAHI, F., VINH-THANG, H., MIKHAILENKO, S. & KALIAGUINE, S. 2013. Electrocatalyst synthesized from metal organic frameworks. *Journal of Power Sources,* 239**,** 415-423.

- AMALI, A. J., SUN, J.-K. & XU, Q. 2014a. From assembled metal-organic framework nanoparticles to hierarchically porous carbon for electrochemical energy storage. *Chemical Communications,* 50**,** 1519-1522.

- AMALI, A. J., SUN, J. K. & XU, Q. 2014b. From assembled metal-organic framework nanoparticles to hierarchically porous carbon for electrochemical energy storage. *Chem Commun (Camb),* 50**,** 1519-22.

- BO LIU, H. S., TOMOKI AKITA, AND QIANG XU 2008. <Metal-Organic Framework as a Template for Porous Carbon Synthesis.pdf>. *J AM Chem Soc*.

- CANDELARIA, S. L., SHAO, Y., ZHOU, W., LI, X., XIAO, J., ZHANG, J.-G., WANG, Y., LIU, J., LI, J. & CAO, G. 2012. Nanostructured carbon for energy storage and conversion. *Nano Energy,* 1**,** 195-220.

- CAR, A., STROPNIK, C. & PEINEMANN, K.-V. 2006. Hybrid membrane materials with different metal–organic frameworks (MOFs) for gas separation. *Desalination,* 200**,** 424-426.

- CHAIKITTISILP, W., HU, M., WANG, H., HUANG, H. S., FUJITA, T., WU, K. C., CHEN, L. C., YAMAUCHI, Y. & ARIGA, K. 2012. Nanoporous carbons through direct carbonization of a zeolitic imidazolate framework for supercapacitor electrodes. *Chem Commun (Camb),* 48**,** 7259-61.

- CHEN, X. Y., XIE, D. H., CHEN, C. & LIU, J. W. 2013. High-performance supercapacitor based on nitrogen-doped porous carbon derived from zinc(II)-bis(8-hydroxyquinoline) coordination polymer. *Journal of Colloid and Interface Science,* 393**,** 241-248.

- CHOI, K. M., JEONG, H. M., PARK, J. H., ZHANG, Y.-B., KANG, J. K. & YAGHI, O. M. 2014. Supercapacitors of nanocrystalline metal–organic frameworks. *ACS nano,* 8**,** 7451-7457.

- DÍAZ, R., ORCAJO, M. G., BOTAS, J. A., CALLEJA, G. & PALMA, J. 2012. Co8-MOF-5 as electrode for supercapacitors. *Materials Letters,* 68**,** 126-128.

- FEIDENHANS'L, R. 1989. Surface structure determination by X-ray diffraction. *Surface Science Reports,* 10**,** 105-188.

- FEREY, G., MILLANGE, F., MORCRETTE, M., SERRE, C., DOUBLET, M. L., GRENECHE, J. M. & TARASCON, J. M. 2007. Mixed-valence li/fe-based metal-organic frameworks with both reversible redox and sorption properties. *Angew Chem Int Ed Engl,* 46**,** 3259-63.

- FREIRE, E., MAYORGA, O. L. & STRAUME, M. 1990. Isothermal titration calorimetry. *Analytical Chemistry,* 62**,** 950A-959A.

- GARSANY, Y., BATURINA, O. A., SWIDER-LYONS, K. E. & KOCHA, S. S. 2010. Experimental Methods for Quantifying the Activity of Platinum Electrocatalysts for the Oxygen Reduction Reaction. *Analytical Chemistry,* 82**,** 6321-6328.

- GE, L., YANG, Y., WANG, L., ZHOU, W., DE MARCO, R., CHEN, Z., ZOU, J. & ZHU, Z. 2015. High activity electrocatalysts from metal–organic framework-carbon nanotube templates for the oxygen reduction reaction. *Carbon,* 82**,** 417-424.

- GORIPARTI, S., MIELE, E., DE ANGELIS, F., DI FABRIZIO, E., PROIETTI ZACCARIA, R. & CAPIGLIA, C. 2014. Review on recent progress of nanostructured anode materials for Li-ion batteries. *Journal of Power Sources,* 257**,** 421-443.

- GRANT GLOVER, T., PETERSON, G. W., SCHINDLER, B. J., BRITT, D. & YAGHI, O. 2011. MOF-74 building unit has a direct impact on toxic gas adsorption. *Chemical Engineering Science,* 66**,** 163-170.

- HAN, Y., QI, P., FENG, X., LI, S., FU, X., LI, H., CHEN, Y., ZHOU, J., LI, X. & WANG, B. 2015. In Situ Growth of MOFs on the Surface of Si Nanoparticles for Highly Efficient Lithium Storage: Si@MOF Nanocomposites as Anode Materials for Lithium-Ion Batteries. *ACS Applied Materials & Interfaces,* 7**,** 2178-2182.

- HAO, F., LI, L., ZHANG, X. & CHEN, J. 2015. Synthesis and electrochemical capacitive properties of nitrogen-doped porous carbon micropolyhedra by direct carbonization of zeolitic imidazolate framework-11. *Materials Research Bulletin,* 66**,** 88-95.

- HAO, P., ZHAO, Z., TIAN, J., LI, H., SANG, Y., YU, G., CAI, H., LIU, H., WONG, C. P. & UMAR, A. 2014. Hierarchical porous carbon aerogel derived from bagasse for high performance supercapacitor electrode. *Nanoscale,* 6**,** 12120-9.

- HORIUCHI, Y., TOYAO, T. & MATSUOKA, M. 2016. Metal–Organic Framework (MOF) and Porous Coordination Polymer (PCP)-Based Photocatalysts. *In:* YAMASHITA, H. & LI, H. (eds.) *Nanostructured Photocatalysts: Advanced Functional Materials.* Cham: Springer International Publishing.

- HOWARTH, A. J., PETERS, A. W., VERMEULEN, N. A., WANG, T. C., HUPP, J. T. & FARHA, O. K. 2017. Best Practices for the Synthesis, Activation, and Characterization of Metal–Organic Frameworks. *Chemistry of Materials,* 29**,** 26-39.

- HU, J., WANG, H., GAO, Q. & GUO, H. 2010. Porous carbons prepared by using metal–organic framework as the precursor for supercapacitors. *Carbon,* 48**,** 3599-3606.

- HU, M., REBOUL, J., FURUKAWA, S., TORAD, N. L., JI, Q., SRINIVASU, P., ARIGA, K., KITAGAWA, S. & YAMAUCHI, Y. 2012. Direct Carbonization of Al-Based Porous Coordination Polymer for Synthesis of Nanoporous Carbon. *Journal of the American Chemical Society,* 134**,** 2864-2867.

- JEREMIAS, F., KHUTIA, A., HENNINGER, S. K. & JANIAK, C. 2012. MIL-100(Al, Fe) as water adsorbents for heat transformation purposes-a promising application. *Journal of Materials Chemistry,* 22**,** 10148-10151.

- JIANG, H. L., LIU, B., LAN, Y. Q., KURATANI, K., AKITA, T., SHIOYAMA, H., ZONG, F. & XU, Q. 2011. From metal-organic framework to nanoporous carbon: toward a very high surface area and hydrogen uptake. *J Am Chem Soc,* 133**,** 11854-7.

- JUNG, D. W., YANG, D. A., KIM, J., KIM, J. & AHN, W. S. 2010. Facile synthesis of MOF-177 by a sonochemical method using 1-methyl-2-pyrrolidinone as a solvent. *Dalton Trans,* 39**,** 2883-7.

- KARIKKETHU PRABHAKARAN, P. & DESCHAMPS, J. 2015. Hydrogen adsorption in lithium doped MIL-101 and MIL-53(Al) at 77 and 298 K up to 100 bar: effect of lithium concentration. *Journal of Porous Materials,* 22**,** 1073-1081.

- KATZ, M. J., BROWN, Z. J., COLON, Y. J., SIU, P. W., SCHEIDT, K. A., SNURR, R. Q., HUPP, J. T. & FARHA, O. K. 2013. A facile synthesis of UiO-66, UiO-67 and their derivatives. *Chemical Communications,* 49**,** 9449-9451.

- LEE, D.-H., HAN, J.-H., KIM, M.-K., LEE, O.-J. & KANG, K. Y. 2012. A Case of Polyarteritis Nodosa Manifesting as a Neuropathy Following Influenza Infection. *J Rheum Dis,* 19**,** 163-167.

- LEE, D. Y., SHINDE, D. V., KIM, E.-K., LEE, W., OH, I.-W., SHRESTHA, N. K., LEE, J. K. & HAN, S.-H. 2013. Supercapacitive property of metal–organic-frameworks with different pore dimensions and morphology. *Microporous and Mesoporous Materials,* 171**,** 53-57.

- LI, B., WEN, H.-M., ZHOU, W. & CHEN, B. 2014a. Porous Metal–Organic Frameworks for Gas Storage and Separation: What, How, and Why? *The Journal of Physical Chemistry Letters,* 5**,** 3468-3479.

- LI, H., EDDAOUDI, M., O'KEEFFE, M. & YAGHI, O. M. 1999. Design and synthesis of an exceptionally stable and highly porous metal- organic framework. *Nature,* 402**,** 276-279.

- LI, J.-S., LI, S.-L., TANG, Y.-J., HAN, M., DAI, Z.-H., BAO, J.-C. & LAN, Y.-Q. 2015. Nitrogen-doped Fe/Fe3C@graphitic layer/carbon nanotube hybrids derived from MOFs: efficient bifunctional electrocatalysts for ORR and OER. *Chemical Communications,* 51**,** 2710-2713.

- LI, J., CHEN, Y., TANG, Y., LI, S., DONG, H., LI, K., HAN, M., LAN, Y.-Q., BAO, J. & DAI, Z. 2014b. Metal–organic framework templated nitrogen and sulfur co-doped porous carbons as highly efficient metal-free electrocatalysts for oxygen reduction reactions. *Journal of Materials Chemistry A,* 2**,** 6316.

- LI, S.-L. & XU, Q. 2013. Metal–organic frameworks as platforms for clean energy. *Energy & Environmental Science,* 6**,** 1656.

- LI, X., CHENG, F., ZHANG, S. & CHEN, J. 2006. Shape-controlled synthesis and lithium-storage study of metal-organic frameworks Zn4O(1,3,5-benzenetribenzoate)2. *Journal of Power Sources,* 160**,** 542-547.

- LIU, B., SHIOYAMA, H., JIANG, H., ZHANG, X. & XU, Q. 2010a. Metal–organic framework (MOF) as a template for syntheses of nanoporous carbons as electrode materials for supercapacitor. *Carbon,* 48**,** 456-463.

- LIU, B., ZHANG, X., SHIOYAMA, H., MUKAI, T., SAKAI, T. & XU, Q. 2010b. Converting cobalt oxide subunits in cobalt metal-organic framework into agglomerated Co3O4 nanoparticles as an electrode material for lithium ion battery. *Journal of Power Sources,* 195**,** 857-861.

- LLABRÉS I XAMENA, F. X., ABAD, A., CORMA, A. & GARCIA, H. 2007. MOFs as catalysts: Activity, reusability and shape-selectivity of a Pd-containing MOF. *Journal of Catalysis,* 250**,** 294-298.

- MA, S., GOENAGA, G. A., CALL, A. V. & LIU, D. J. 2011. Cobalt imidazolate framework as precursor for oxygen reduction reaction electrocatalysts. *Chemistry,* 17**,** 2063-7.

- MAO, C., KONG, A., WANG, Y., BU, X. & FENG, P. 2015. MIL-100 derived nitrogen-embodied carbon shells embedded with iron nanoparticles. *Nanoscale,* 7**,** 10817-10822.

- MARTIN WINTER, R. J. B. 2004. What Are Batteries, Fuel Cells, and Supercapacitors.pdf. *Chemical Review,* 104**,** 4245-4269.

- MCMULLAN, D. 1995. Scanning electron microscopy 1928–1965. *Scanning,* 17**,** 175-185.

- MITSUDA, K., BAUTZ, M., INOUE, H., KELLEY, R. L., KOYAMA, K., KUNIEDA, H., MAKISHIMA, K., OGAWARA, Y., PETRE, R., TAKAHASHI, T., TSUNEMI, H., WHITE, N. E., ANABUKI, N., ANGELINI, L., ARNAUD, K., AWAKI, H., BAMBA, A., BOYCE, K., BROWN, G. V., CHAN, K.-W., COTTAM, J., DOTANI, T., DOTY, J., EBISAWA, K., EZOE, Y., FABIAN, A. C., FIGUEROA, E., FUJIMOTO, R., FUKAZAWA, Y., FURUSHO, T., FURUZAWA, A., GENDREAU, K., GRIFFITHS, R. E., HABA, Y., HAMAGUCHI, K., HARRUS, I., HASINGER, G., HATSUKADE, I., HAYASHIDA, K., HENRY, P. J., HIRAGA,

J. S., HOLT, S. S., HORNSCHEMEIER, A., HUGHES, J. P., HWANG, U., ISHIDA, M., ISHISAKI, Y., ISOBE, N., ITOH, M., IYOMOTO, N., KAHN, S. M., KAMAE, T., KATAGIRI, H., KATAOKA, J., KATAYAMA, H., KAWAI, N., KILBOURNE, C., KINUGASA, K., KISSEL, S., KITAMOTO, S., KOHAMA, M., KOHMURA, T., KOKUBUN, M., KOTANI, T., KOTOKU, J. I., KUBOTA, A., MADEJSKI, G. M., MAEDA, Y., MAKINO, F., MARKOWITZ, A., MATSUMOTO, C., MATSUMOTO, H., MATSUOKA, M., MATSUSHITA, K., MCCAMMON, D., MIHARA, T., MISAKI, K., MIYATA, E., MIZUNO, T., MORI, K., MORI, H., MORII, M., MOSELEY, H., MUKAI, K., MURAKAMI, H., MURAKAMI, T., MUSHOTZKY, R., NAGASE, F., NAMIKI, M., NEGORO, H., NAKAZAWA, K., NOUSEK, J. A., OKAJIMA, T., OGASAKA, Y., OHASHI, T., OSHIMA, T., OTA, N., OZAKI, M., OZAWA, H., PARMAR, A. N., et al. 2007. The X-Ray Observatory Suzaku. *Publications of the Astronomical Society of Japan,* 59**,** S1-S7.

- MORENO-PIRAJÁN, J. C., GIRALDO, L. & VARGAS, D. P. 2012. Determination of Energy Characteristic and Microporous Volume by Immersion Calorimetry in Carbon Monoliths. *E-Journal of Chemistry,* 9.

- MOROZAN, A. & JAOUEN, F. 2012. Metal organic frameworks for electrochemical applications. *Energy & Environmental Science,* 5**,** 9269.

- MUELLER, U., SCHUBERT, M., TEICH, F., PUETTER, H., SCHIERLE-ARNDT, K. & PASTRÉ, J. 2006. Metal–organic frameworks—prospective industrial applications. *J. Mater. Chem.,* 16**,** 626-636.

- PAN, Y., LIU, Y., ZENG, G., ZHAO, L. & LAI, Z. 2011. Rapid synthesis of zeolitic imidazolate framework-8 (ZIF-8) nanocrystals in an aqueous system. *Chemical Communications,* 47**,** 2071-2073.

- PARK, K. S., NI, Z., COTE, A. P., CHOI, J. Y., HUANG, R., URIBE-ROMO, F. J., CHAE, H. K., O'KEEFFE, M. & YAGHI, O. M. 2006. Exceptional chemical and thermal stability of zeolitic imidazolate frameworks. *Proc Natl Acad Sci U S A,* 103**,** 10186-91.

- PEARCE, R. B. 2004. GOLDSTEIN, J., NEWBURY, D., JOY, D., LYMAN, C., ECHLIN, P., LIFSHIN, E., SAWYER, L. & MICHAEL, J. 2003. Scanning Electron Microscopy and X-Ray Microanalysis, 3rd ed. xix + 689 pp. New York, Boston, Dordrecht, London, Moscow: Kluwer Academic/Plenum Publishers. Price Euros 76.00, US $75.00, £48.00 (hard covers). ISBN 0 306 47292 9. *Geological Magazine,* 140**,** 728-729.

- PIERRE TRAN-VANA, K. B., MATHIEU MORCRETTEB, MICHEL HERLEMA, JEAN-MARIE TARASCONB, A. K. CHEETHAMC AND GÉRARD FÉREYA 2002. <Reactivity of Lithium with a Microporous Phosphate.pdf>. *Journal of New Materials for Electrochemical Systems,* 6**,** 29-31.

- PROIETTI, E., JAOUEN, F., LEFÈVRE, M., LAROUCHE, N., TIAN, J., HERRANZ, J. & DODELET, J.-P. 2011. Iron-based cathode catalyst with enhanced power density in polymer electrolyte membrane fuel cells. 2**,** 416.

- QU, Q., YUN, J., WAN, Z., ZHENG, H., GAO, T., SHEN, M., SHAO, J. & ZHENG, H. 2014. MOF-derived microporous carbon as a better choice for Na-ion batteries than mesoporous CMK-3. *RSC Advances,* 4**,** 64692-64697.

- RADHAKRISHNAN, L., REBOUL, J., FURUKAWA, S., SRINIVASU, P., KITAGAWA, S. & YAMAUCHI, Y. 2011. Preparation of Microporous Carbon Fibers through Carbonization of Al-Based Porous Coordination Polymer (Al-PCP) with Furfuryl Alcohol. *Chemistry of Materials,* 23**,** 1225-1231.

- RAJARATHNAM, K. & RÖSGEN, J. 2014. Isothermal titration calorimetry of membrane proteins — Progress and challenges. *Biochimica et Biophysica Acta (BBA) - Biomembranes,* 1838**,** 69-77.

- REDDY, M. V., SUBBA RAO, G. V. & CHOWDARI, B. V. 2013. Metal oxides and oxysalts as anode materials for Li ion batteries. *Chem Rev,* 113**,** 5364-457.

- RESCH, G., HELD, A., FABER, T., PANZER, C., TORO, F. & HAAS, R. 2008. Potentials and prospects for renewable energies at global scale. *Energy Policy,* 36**,** 4048-4056.

- ROUQUEROL, F., ROUQUEROL, J. & SING, K. 1999. CHAPTER 1 - Introduction. *Adsorption by Powders and Porous Solids.* London: Academic Press.

- SALUNKHE, R. R., KAMACHI, Y., TORAD, N. L., HWANG, S. M., SUN, Z., DOU, S. X., KIM, J. H. & YAMAUCHI, Y. 2014. Fabrication of symmetric supercapacitors based on MOF-derived nanoporous carbons. *Journal of Materials Chemistry A,* 2**,** 19848-19854.

- SEGAKWENG, T., MUSYOKA, N. M., REN, J., CROUSE, P. & LANGMI, H. W. 2016. Comparison of MOF-5- and Cr-MOF-derived carbons for hydrogen storage application. *Research on Chemical Intermediates,* 42**,** 4951-4961.

- SHI, J., HEI, S., LIU, H., FU, Y., ZHANG, F., ZHONG, Y. & ZHU, W. 2013. Synthesis of MIL-100(Fe) at Low Temperature and Atmospheric Pressure. *Journal of Chemistry,* 2013**,** 4.

- SHI, Y., ZHANG, X., WANG, L. & LIU, G. 2014. MOF-derived porous carbon for adsorptive desulfurization. *AIChE Journal,* 60**,** 2747-2751.

- SHIN, J., KIM, M., CIRERA, J., CHEN, S., HALDER, G. J., YERSAK, T. A., PAESANI, F., COHEN, S. M. & MENG, Y. S. 2015. MIL-101(Fe) as a lithium-ion battery electrode material: a relaxation and intercalation mechanism during lithium insertion. *J. Mater. Chem. A,* 3**,** 4738-4744.

- SILVESTRE-ALBERO, J., GÓMEZ DE SALAZAR, C., SEPÚLVEDA-ESCRIBANO, A. & RODRíGUEZ-REINOSO, F. 2001. Characterization of microporous solids by immersion calorimetry. *Colloids and Surfaces A: Physicochemical and Engineering Aspects,* 187-188**,** 151-165.

- SOPIAN, K. & WAN DAUD, W. R. 2006. Challenges and future developments in proton exchange membrane fuel cells. *Renewable Energy,* 31**,** 719-727.

- SPANOPOULOS, I., BRATSOS, I., TAMPAXIS, C., KOURTELLARIS, A., TASIOPOULOS, A., CHARALAMBOPOULOU, G., STERIOTIS, T. A. & TRIKALITIS, P. N. 2015. Enhanced gas-sorption properties of a high surface area, ultramicroporous magnesium formate. *CrystEngComm,* 17**,** 532-539.

- SRINIVAS, G., KRUNGLEVICIUTE, V., GUO, Z.-X. & YILDIRIM, T. 2014. Exceptional CO2capture in a hierarchically porous carbon with simultaneous high surface area and pore volume. *Energy Environ. Sci.,* 7**,** 335-342.

- STEELE, B. C. H. & HEINZEL, A. 2001. Materials for fuel-cell technologies. *Nature,* 414**,** 345-352.

- STOCK, N. & BISWAS, S. 2012. Synthesis of metal-organic frameworks (MOFs): routes to various MOF topologies, morphologies, and composites. *Chem Rev,* 112**,** 933-69.

- TAN, Y., ZHANG, W., GAO, Y., WU, J. & TANG, B. 2015. Facile synthesis and supercapacitive properties of Zr-metal organic frameworks (UiO-66). *RSC Advances,* 5**,** 17601-17605.

- TANG, J., SALUNKHE, R. R., LIU, J., TORAD, N. L., IMURA, M., FURUKAWA, S. & YAMAUCHI, Y. 2015. Thermal Conversion of Core–Shell Metal–Organic Frameworks: A New Method for Selectively Functionalized Nanoporous Hybrid Carbon. *Journal of the American Chemical Society,* 137**,** 1572-1580.

- THOMSON, G. W. 1946. The Antoine Equation for Vapor-pressure Data. *Chemical Reviews,* 38**,** 1-39.

- TORAD, N. L., HU, M., ISHIHARA, S., SUKEGAWA, H., BELIK, A. A., IMURA, M., ARIGA, K., SAKKA, Y. & YAMAUCHI, Y. 2014. Direct synthesis of MOF-derived nanoporous carbon with magnetic Co nanoparticles toward efficient water treatment. *Small,* 10**,** 2096-107.

- VOLKRINGER, C., POPOV, D., LOISEAU, T., FÉREY, G. R., BURGHAMMER, M., RIEKEL, C., HAOUAS, M. & TAULELLE, F. 2009. Synthesis, Single-Crystal X-ray Microdiffraction, and NMR Characterizations of the Giant Pore Metal-Organic Framework Aluminum Trimesate MIL-100. *Chemistry of Materials,* 21**,** 5695-5697.

- VOLKRINGER, C., POPOV, D., LOISEAU, T., GUILLOU, N., FEREY, G., HAOUAS, M., TAULELLE, F., MELLOT-DRAZNIEKS, C., BURGHAMMER, M. & RIEKEL, C. 2007. A microdiffraction set-up for nanoporous metal-organic-framework-type solids. *Nat Mater,* 6**,** 760-4.

- WANG, G., ZHANG, L. & ZHANG, J. 2012. A review of electrode materials for electrochemical supercapacitors. *Chemical Society Reviews,* 41**,** 797-828.

- WANG, L., FENG, X., REN, L., PIAO, Q., ZHONG, J., WANG, Y., LI, H., CHEN, Y. & WANG, B. 2015. Flexible Solid-State Supercapacitor Based on a Metal–Organic Framework Interwoven by Electrochemically-Deposited PANI. *Journal of the American Chemical Society,* 137**,** 4920-4923.

- WANG, X., ZHOU, J., FU, H., LI, W., FAN, X., XIN, G., ZHENG, J. & LI, X. 2014. MOF derived catalysts for electrochemical oxygen reduction. *Journal of Materials Chemistry A,* 2**,** 14064-14070.

- WEI, J., HU, Y., LIANG, Y., KONG, B., ZHANG, J., SONG, J., BAO, Q., SIMON, G. P., JIANG, S. P. & WANG, H. 2015. Nitrogen-Doped Nanoporous Carbon/Graphene Nano-Sandwiches: Synthesis and Application for Efficient Oxygen Reduction. *Advanced Functional Materials,* 25**,** 5768-5777.

- WILLIAMS, D. B. & CARTER, C. B. 1996. The Transmission Electron Microscope. *Transmission Electron Microscopy: A Textbook for Materials Science.* Boston, MA: Springer US.

- XI, K., CAO, S., PENG, X., DUCATI, C., KUMAR, R. V. & CHEETHAM, A. K. 2013. Carbon with hierarchical pores from carbonized metal-organic frameworks for lithium sulphur batteries. *Chem Commun (Camb),* 49**,** 2192-4.

- XIA, W., ZHU, J., GUO, W., AN, L., XIA, D. & ZOU, R. 2014. Well-defined carbon polyhedrons prepared from nano metal-organic frameworks for oxygen reduction. *Journal of Materials Chemistry A,* 2**,** 11606-11613.

- XIA, W., ZOU, R., AN, L., XIA, D. & GUO, S. 2015. A metal-organic framework route to in situ encapsulation of Co@Co3O4@C core@bishell nanoparticles into a highly ordered porous carbon matrix for oxygen reduction. *Energy & Environmental Science,* 8**,** 568-576.

- XU, H., ZHOU, S., XIAO, L., WANG, H., LI, S. & YUAN, Q. 2015. Fabrication of a nitrogen-doped graphene quantum dot from MOF-derived porous carbon and its application for highly selective fluorescence detection of Fe3+. *Journal of Materials Chemistry C,* 3**,** 291-297.

- YANG, B., LU, Q., WANG, Y., ZHUANG, L., LU, J., LIU, P., WANG, J. & WANG, R. 2003. Simple and Low-Cost Preparation Method for Highly Dispersed PtRu/C Catalysts. *Chemistry of Materials,* 15**,** 3552-3557.

- YANG, J., XIONG, P., ZHENG, C., QIU, H. & WEI, M. 2014. Metal-organic frameworks: a new promising class of materials for a high performance supercapacitor electrode. *Journal of Materials Chemistry A,* 2**,** 16640-16644.

- YOO, J., LEE, S., LEE, C. K., KIM, C., FUJIGAYA, T., PARK, H. J., NAKASHIMA, N. & SHIM, J. K. 2014. Homogeneous decoration of zeolitic imidazolate framework-8 (ZIF-8) with core-shell structures on carbon nanotubes. *RSC Advances,* 4**,** 49614-49619.

- YOON, M. & MOON, D. 2015. New Zr (IV) based metal-organic framework comprising a sulfur-containing ligand: Enhancement of CO2 and H2 storage capacity. *Microporous and Mesoporous Materials,* 215**,** 116-122.

- YOUNG, C., SALUNKHE, R. R., TANG, J., HU, C.-C., SHAHABUDDIN, M., YANMAZ, E., HOSSAIN, M. S. A., KIM, J. H. & YAMAUCHI, Y. 2016. Zeolitic imidazolate framework (ZIF-8) derived nanoporous carbon: the effect of carbonization temperature on the supercapacitor performance in an aqueous electrolyte. *Physical Chemistry Chemical Physics,* 18**,** 29308-29315.

- YU, G., ZOU, X., WANG, A., SUN, J. & ZHU, G. 2014. Generation of bimodal porosity via self-extra porogenes in nanoporous carbons for supercapacitor application. *Journal of Materials Chemistry A,* 2**,** 15420-15427.

- YUAN, D., CHEN, J., TAN, S., XIA, N. & LIU, Y. 2009. Worm-like mesoporous carbon synthesized from metal–organic coordination polymers for supercapacitors. *Electrochemistry Communications,* 11**,** 1191-1194.

- YUAN, W., GARAY, A. L., PICHON, A., CLOWES, R., WOOD, C. D., COOPER, A. I. & JAMES, S. L. 2010. Study of the mechanochemical formation and resulting properties of an archetypal MOF: Cu3(BTC)2 (BTC = 1,3,5-benzenetricarboxylate). *CrystEngComm,* 12**,** 4063.

- ZHANG, L., SU, Z., JIANG, F., YANG, L., QIAN, J., ZHOU, Y., LI, W. & HONG, M. 2014a. Highly graphitized nitrogen-doped porous carbon nanopolyhedra derived from ZIF-8 nanocrystals as efficient electrocatalysts for oxygen reduction reactions. *Nanoscale,* 6**,** 6590-6602.

- ZHANG, L. L. & ZHAO, X. S. 2009. Carbon-based materials as supercapacitor electrodes. *Chemical Society Reviews,* 38**,** 2520-2531.

- ZHANG, P., SUN, F., XIANG, Z., SHEN, Z., YUN, J. & CAO, D. 2014b. ZIF-derived in situ nitrogen-doped porous carbons as efficient metal-free electrocatalysts for oxygen reduction reaction. *Energy & Environmental Science,* 7**,** 442-450.

- ZHAO, D., SHUI, J.-L., CHEN, C., CHEN, X., REPROGLE, B. M., WANG, D. & LIU, D.-J. 2012. Iron imidazolate framework as precursor for electrocatalysts in polymer electrolyte membrane fuel cells. *Chemical Science,* 3**,** 3200.

- ZHAO, S., YIN, H., DU, L., HE, L., ZHAO, K., CHANG, L., YIN, G., ZHAO, H., LIU, S. & TANG, Z. 2014a. Carbonized Nanoscale Metal–Organic Frameworks as High Performance Electrocatalyst for Oxygen Reduction Reaction. *ACS Nano,* 8**,** 12660-12668.

- ZHAO, X., ZHAO, H., ZHANG, T., YAN, X., YUAN, Y., ZHANG, H., ZHAO, H., ZHANG, D., ZHU, G. & YAO, X. 2014b. One-step synthesis of nitrogen-doped microporous carbon materials as metal-free electrocatalysts for oxygen reduction reaction. *Journal of Materials Chemistry A,* 2**,** 11666-11671.

- ZHAO, Y., LI, X., YAN, B., LI, D., LAWES, S. & SUN, X. 2015. Significant impact of 2D graphene nanosheets on large volume change tin-based anodes in lithium-ion batteries: A review. *Journal of Power Sources,* 274**,** 869-884.

- ZHAO, Y., SONG, Z., LI, X., SUN, Q., CHENG, N., LAWES, S. & SUN, X. 2016. Metal organic frameworks for energy storage and conversion. *Energy Storage Materials,* 2**,** 35-62.

- ZHENG, F., YANG, Y. & CHEN, Q. 2014. High lithium anodic performance of highly nitrogen-doped porous carbon prepared from a metal-organic framework. 5**,** 5261.

- ZHONG, S., ZHAN, C. & CAO, D. 2015. Zeolitic imidazolate framework-derived nitrogen-doped porous carbons as high performance supercapacitor electrode materials. *Carbon,* 85**,** 51-59.